EMISSION PROPERTIES OF SMALL MOLECULE PHOSPHOR EMITTERS IN ORGANIC LIGHT EMITTING DIODES

seit 1558

DISSERTATION

for the acquisition of the academic title

Doktor-Ingenieur (Dr.-Ing.)

submitted to the Council of the Faculty of Physics and Astronomy

of the Friedrich-Schiller-University Jena

by Rossá Mac Ciarnáin

born in Sligo, Ireland on the 16th June 1987

Supervisors:

Major Supervisor:……..……..

Associate Supervisor:…….……

Associate Supervisor:…….……

Day of the Disputation:……...……...

CONTENTS

1. Introduction……1

2. OLED fundamentals……5
   2.1 Charge carrier dynamics……5
   2.2 Exciton formation and relaxation……7
      2.2.1 Exciton dynamics……7
      2.2.2 Molecular energy levels and orbitals……9
   2.3 Emission from a dipole ensemble……11
   2.4 Intrinsic quantum efficiency & emitter decay lifetime……16
   2.5 OLED emission pattern……17

3. Methods and devices……19
   3.1 Device fabrication, structure & layer characterization……20
      3.1.1 Device fabrication, structure & material energy levels……20
      3.1.2 Single red emitter OLED structure……21
      3.1.3 Dual red & green emitter OLED structure……24
   3.2 Experimental procedures……25
      3.2.1 Layer characterization……25
      3.2.2 General measurement setup……26
      3.2.3 Electroluminescence measurements……27
      3.2.4 Photoluminescence measurements……27
      3.2.5 Transient luminescence measurements……27
   3.3 Single emitter active optical property extraction……28
   3.4 Fitting & error analysis……30
      3.4.1 Passive optical properties……30
      3.4.2 Angular intensity spectrum……31
      3.4.3 Fitting procedures……33

4. Results & discussion: Single red emitter devices……35
4.1 Emission zone profile……35
4.1.1 EZP confined to EML ……35
4.1.2 EZP Extended into blocking layers……38
4.2 Emitter ensemble intrinsic emission spectrum……43
4.3 Emitter ensemble orientation ratio……44
4.4 Intrinsic quantum efficiency of interlayer devices…… 46
4.4.1 Thin Ag:Ge interlayer optical properties……47
4.4.2 EL and PL intrinsic quantum efficiency……49
4.5 Emitter ensemble orientation distribution……53
4.5.1 Emission lifetime analysis of interlayer devices……53
4.5.2 Excitation reorientation in non-interlayer devices……59
4.5.3 Excitation reorientation in interlayer devices……64
4.5.4 Angular intensity spectral shape in interlayer devices……65

5. Results & discussion: Dual colour devices……67
5.1 Adaption of AOP extraction methods for dual emitter case……67
5.2 Green emission zone profile……72
5.3 Green orientation ratio……78
5.4 Red emission zone profile……80
5.5 Red orientation ratio……89

6. Conclusions and outlook……93

Bibliography……98

List of figures……113

List of abbreviations……115

List of publications……116

1. INTRODUCTION

This dissertation concerns the origination of radiation in bottom-emitting OLED devices, with regard to the spatial and orientational distributions of red-emitting $Ir(MDQ)_2(acac)$ and green-emitting $Ir(ppy)_3$ small molecules, which are key parameters affecting internal and external OLED efficiency respectively.

Organic light emitting diodes are now a mature, developed technology, as displays in hundreds of millions of products or as an increasingly used high class lighting solution in automobiles or other highly specialized applications. Currently OLEDs are an expensive lighting/display technology but current research on roll-to-roll solution processing [1] promises OLEDs to become much cheaper. OLEDs have many advantages as a field-changing light emission technology. They can be slim (OLED televisions can be 2.5 mm thick [2]), lightweight, transparent, flexible and large-area. Prototype applications shown include wallpaper lighting solutions [3], display/window [4], foldable [5] and rollable [6] displays. OLED televisions made by LG Display are regarded by technology journalists to be the highest quality televisions ever released [7, 8, 9, 10]. Samsung's mobile device OLED displays have recently been reviewed as the highest performance mobile device display ever tested [11]. For lighting applications, OLED technology offers sun-like spectra [12] and laboratory prototype devices promise the release of competitive, efficient products. In 2014, laboratory demonstrations of OLED devices for lighting had already well overtaken the fluorescent benchmark efficiency of 100 lm/W and the efficiency of consumer inorganic LEDs [13, 14]. A large area (15 cm^2) white single OLED device from Konica Minolta reached an efficiency of 131 lm/W [15]. The technological advances to enable such efficiency breakthroughs were due to advanced optical simulation techniques [16].

Apart from decreasing the cost, there is still much scope to improve OLED device efficiency with the aim of enabling the OLED market to overtake competing technologies. OLED efficiency considerations can be divided into internal quantum efficiency which deals with charge recombination and non-radiative quenching of the molecular excitations (excitons) and external quantum efficiency which deals with how well the created light can be outcoupled from the device layers into air.

With regard to internal quantum efficiency, the device property which gives information on charge recombination and exciton quenching is the emission zone profile (EZP), which is the spatial distribution of the light emission sources in the device. The EZP of an OLED has been shown to give information on charge transport and excited state diffusion [17, 18, 19, 20, 21], internal quantum efficiency [22, 23], energy transfer between different emitter molecules [24], material degradation and device lifetime [25] and the increasing quenching of excitons at high current densities (which lighting solutions require), the so-called "efficiency roll-off" [26, 27]. Too high a concentration of excitons has been strongly linked as a main cause [28, 26, 29]. Knowledge of the EZP gives insight to optimise devices to have a strictly positioned and constant EZP with position. Therefore accurate measures of the profile of the emission zone are needed to further understand efficiency roll-off and related quenching processes and to design devices with an optimally spread out exciton profile [30, 31]. Previously, the EZP has been simulated using an electronic model [21, 22, 32, 33, 34, 35], measured using sensing layers [18, 36, 37, 38, 39] which requires fabrication of many devices, and more recently, extracted by microcavity inverse light outcoupling approaches [40, 41], where only one single adapted microcavity device is needed to extract the EZP. The spatial resolution of EZPs resulting from this method has been found to be limited to quadratic functions [42]. All EZP results published thus far have assumed an EZP confined to exactly the planned layer dimensions where emitter molecules were deposited (emission layer). In most cases this means that small molecules of the order of 1 nm in size are deposited and remain within a 10 nm wide layer. However, diffusion of small molecule emitters in OLEDs over a distance of 10 nm after heating at ~ 90 °C has previously been observed [41, 43].

(1) The first goal of this work was to adapt the established microcavity inverse light outcoupling approach of extracting the device EZP to investigate if there is light emission from other layers as well as the emission layer.

With regard to external quantum efficiency, optical outcoupling efficiency is still a bottleneck for OLED devices and is limited to a maximum of ~20% [44, 45]. Refractive, diffractive or scattering outcoupling enhancing solutions can improve overall device efficiency by up to 20% [46]). However these solutions should not allow for OLEDs to be cheaply mass-produced. The spontaneous alignment of phosphorescent emitter molecules in OLEDs has attracted continuous attention

because of its strong effect on light outcoupling efficiency [47, 48, 49]. A fully parallel (with respect to the device layer interfaces) orientation of the emitter molecules can give a 50 % increase [50, 51] in the amount of light emitted from the device compared to randomly oriented emitters. Spontaneous alignment has been observed for several emitters [52] and has been correlated with the permanent molecular dipole moments [52], a strong formation of supra molecules due to an alignment of the triplet excited states within the host [53], or an interaction of anisotropic molecules at the thin film surface during thermal deposition [54]. Resulting efficiency enhancements have been reported for both standard guest-host systems [49, 50] as well as emitters exhibiting delayed fluorescence [55]. Different experimental approaches have been conducted to analyze the emitter ensemble orientation distribution in an OLED. Electroluminescence (EL) [49, 56] or photoluminescence (PL) [49, 55, 56, 57] emission patterns selectively compared with simulated emission patterns allow one to extract the second moments of the distribution, provided that the experimental configuration allows one to observe sufficient emission from perpendicular emitters [42]. Alternatively, the analysis of the position dependent emission lifetime [58, 59, 60, 61] can yield information about the orientation distribution. Tailoring of molecular orientation is currently highly desired to increase light outcoupling but current measurement methods do not give information on the detailed orientation distribution. Only an extraction of the ratio between parallel and perpendicular emission components (the orientation ratio) has been thus-far demonstrated. The position dependent emission lifetime approach exploits the fact that the Purcell effect [62] introduces strong orientation dependent emission rates, when the emitters are close to the metal cathode. Such devices give a high lifetime orientation splitting but also very low perpendicular emitter emission. If an additional thin metal interlayer was placed near the emitters to replace the strong cathode lifetime splitting effect while having a device with the cathode further away from the emitters, which enables high perpendicular emitter emission, this would allow for the separate observation of both parallel and perpendicular emitter lifetimes.

(2) The second goal of this work was to use specialised devices to measure both parallel and perpendicular emitter lifetimes which could give information on the detailed emitter orientation distribution, rather than just the orientation ratio.

As mentioned, methods for single emitter device EZP and orientation ratio extraction are well established [63]. However, it is very important to extend this emitter property analysis to multi-emitter OLEDs. Best performing commercial displays such as the afore-mentioned LG television use OLEDs featuring blue, green and red emitter layers stacked on top of each other in a single device [64]. Currently it is not well known how emitter properties may change when placed in such structures compared to single emitter devices. Such an extraction technique to obtain knowledge of the individual emitter optical properties would give a deeper physical understanding to allow for further improvements in device efficiency and lifetime in these best-in-class displays and very promising lighting solutions.

(3) The third goal of this work was to extend the established single emitter device emitter property extraction methods to dual emitter devices.

In the next chapter, Chapter 2, this dissertation will first introduce the necessary OLED optics background information to enable the reader to understand and follow the attempts to successfully reach these 3 goals. Chapter 3 will explain the experimental methods and analysis techniques used to obtain all results and conclusions. The results of the single emitter device research with regard to goal 1 and goal 2 is presented with discussion in Chapter 4. The second results and discussion chapter, Chapter 5, will detail the extraction of the orientation ratio and emission zone in dual colour devices towards reaching goal 3. Finally Chapter 6 will conclude upon how this work increased the knowledge of OLED emission processes and will give an outlook with a view to further advance OLED analysis and optimisation procedures.

2. OLED FUNDAMENTALS

A summary of all the OLED background necessary for the understanding of the methods, results and discussion of this dissertation are shown in this chapter. Section 2.1 introduces the dynamics of charge carriers during electroluminescence of an OLED device until an exciton is created by recombination. Section 2.2 gives the important exciton dynamic and quenching processes which may occur instead of direct emission and a brief overview of the molecular energy levels responsible for OLED luminescence. The far-field angular intensity pattern $I_{exp}(\theta, \lambda)$ is the experimentally accessible parameter from which information on the internal device emission processes can be extracted. Simulating this emission pattern, varying the individual optical properties of the emission system and comparing the result with the experimental pattern can give information about these properties. As a background to these simulation procedures, Section 2.4 introduces the classical Hertz dipole model used to simulate radiation from OLED emitters. Section 2.5 adds important considerations arising from the Purcell effect and finally Section 2.6 describes how the final OLED angular emission intensity spectrum is simulated.

2.1 Charge carrier dynamics

A typical OLED charge transport structure is shown in Fig.2.1. Due to the work function of the anode and cathode, an applied forward voltage bias (positive anode) V_{ext} is necessary to inject electrons from the cathode and holes from the anode into the transport layers. The anode should have a high work function Φ_A and the cathode, a low work function Φ_C (see Fig.2.1), so that a lower device operation voltage is required for sufficient charge injection. When this voltage is applied over the anode and cathode, electrons from the cathode and holes from the anode can be injected into electron transport layer (ETL) and the hole transport layer (HTL) respectively. The HTL is doped with electron acceptor molecules and the ETL is doped with electron donor molecules to compensate for the generally poor intrinsic conductivity of organic semiconductors. These electrons and holes can then “hop” through the allowed molecular energy levels; the highest occupied molecular orbital (HOMO) and the lowest unoccupied molecular orbital (LUMO) to reach the recombination/emission layer (EML). The HOMO and LUMO of organic

semiconductors are analogous to the valence and conduction bands of inorganic semiconductors. Electrons can hop to lower energy LUMO levels and can only move to higher energy LUMO levels when thermally excited. Reciprocally, holes hop to increasing HOMO energy levels (the electron drops energy level). The charges next pass through an intrinsic semiconductor hole blocking layer (HBL) and electron blocking layer (EBL) to reach the (EML). The HBL and EBL are chosen to have the correct HOMO and LUMO energy levels to block the further transport of charge carriers out of the EML and thus ensure recombination inside the EML. The EML is typically composed of a guest-host system of two molecular species to prevent concentration quenching [65]. Electron (or hole) transport depends on two parameters; adjacent layer HOMO/LUMO energy levels and intrinsic material charge carrier mobilities.

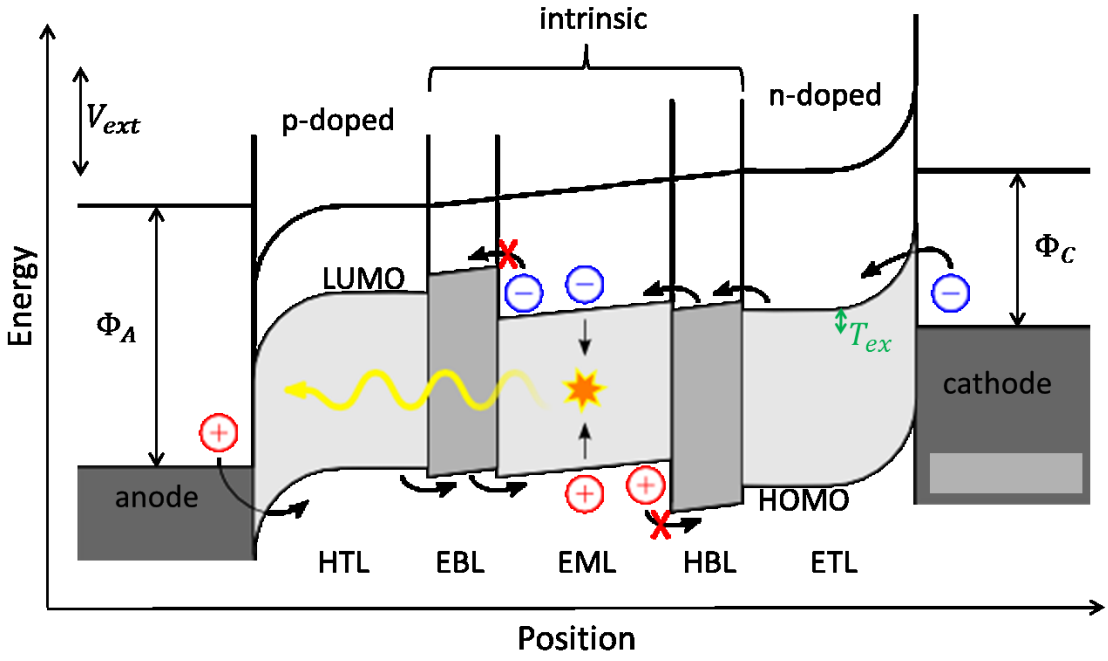

Fig.2.1 Charge carrier energy levels in an OLED under forward voltage bias. *The work functions of the anode* $\boldsymbol{\Phi_A}$ *and cathode* $\boldsymbol{\Phi_C}$ *are shown along with the HOMO and LUMO energy levels of the organic layers under a forward voltage bias* $\boldsymbol{V_{ext}}$ *. Red circles with plus signs inside represent holes and blue circles with minus signs inside represent electrons. Single-sided black arrows show the charge carrier transport directions. Band bending of the HOMO and LUMO levels by the applied voltage can be observed. Red "X" symbols denote hops forbidden by the blocking layer energy levels. The red and yellow star represents a recombination event and the yellow wave signifies light emission. (adapted from [66]).*

The devices in this work are bottom emitting, in that the light is emitted through the substrate, via a transparent anode, usually made from indium tin oxide (ITO). This type of electrically stimulated photon emission is called electroluminescence (EL).

2.2 Exciton formation and relaxation

In this subsection it will first be described how excitons (a bound excitation state of an electron and hole) can be formed by a recombination of charge carriers (Section 2.1) or via photoexcitation. The decay of this excited state can result in the emission of radiation. The frequency of this radiation depends on the energy difference between the HOMO and LUMO.

In the recombination of charge carriers, electrostatic forces bring the electrons and holes towards each other in the EML and they can recombine forming an exciton. Hole trapping on the emitter can occur if there is not too large an energy gap between the HTL HOMO and the emitter HOMO [67]. Trapping charges on the emitter should result in a more efficient device than energy transfer from the host as other relaxation processes are more unlikely to occur [68]. As such, the devices in this work have well-chosen materials (see section 3.1.) to prevent the presence of electrons and holes together on host molecules, allowing recombination only on the emitter molecules. Alternatively, in photoexcitation, following the absorption of a photon by the semiconducting molecule, an electron is promoted from the HOMO to the LUMO. A hole is created in the HOMO and this hole is bound to the electron by the Coulomb force, forming an exciton. Within ~100 fs of the excitation the molecule will resort to the excited state geometry [69, 70].

2.2.1 Exciton Dynamics

An exciton can be transferred from a donor molecule to an acceptor molecule via an energy transfer process [69, 71, 72]. Energy transfer plays a role both in exciton diffusion between molecules of the same material, and in exciton transfer between molecules of different materials, e.g. transfer from host to guest molecules or from a green to a red dye. Radiative energy transfer entails the absorption of an emitted photon by an acceptor molecule, depending on the overlap of the absorption and

emission spectra of the two molecules. With photon propagation, this process can occur over tens of nanometers [73, 74].

Two types of non-radiative energy transfer can occur in OLED devices. In Förster resonant energy transfer [75] a virtual photon is exchanged via a non-radiative dipole coupling. In contrast, in Dexter transfer [76] an exchange of electrons is required. The rate of Förster transfer Γ_F is given by

$$\Gamma_F = \tau^{-1}\left(\frac{R_F}{R}\right)^6 \tag{2.2.1}$$

where τ is the intrinsic lifetime of the exciton (i.e. in absence of the acceptor), R_F the Förster radius, and R the distance between donor and acceptor. The Förster radius is defined such that at the Förster radius, the Förster transfer rate is equal to the sum of the radiative and non-radiative decay rates.

The rate of Dexter transfer Γ_D is given by

$$\Gamma_D = \frac{2\pi}{\hbar}K^2\exp\left(\frac{-2R}{\lambda_{ex}}\right)J \tag{2.2.2}$$

where $\hbar = \frac{h}{2\pi}$ is the reduced Planck constant, K *is* an energy constant, λ_{ex} is the wavefunction decay length for excitons, and J the spectral overlap between donor and acceptor. Since the exchange of electrons in Dexter transfer requires the overlap of the two molecular wavefunctions, it occurs at much shorter distances than Förster transfer.

Excitons can be lost due to interactions with other excitons or polarons (charge carrier with polarization effect). The magnitude of each effect depends on the exciton and charge carrier density, which both increase with device current density, leading to efficiency roll-off [77]. In phosphorescent OLEDs with a high exciton density, triplet-triplet annihilation (TTA) is an important loss mechanism. Where singlets are produced from such a Dexter-mediated reaction, delayed fluorescence can occur [78]. Förster-mediated TTA can occur where the triplet emission and absorption spectra overlap. Here, the acceptor will become excited then quickly thermally de-excite, with the loss of one triplet. Triplet polaron quenching (TPQ) can also occur for excitons interacting with electrons or holes. A Dexter-mediated exchange of the excited exciton electron for the unexcited electron for example can occur, resulting in non-radiative relaxation. High device fields can also cause quenching by disassociation of excitons [79, 80].

2.2.2 Molecular energy levels and orbitals

Luminescence properties are, in general, determined by molecular orbitals responsible for the electronic ground state (HOMO) and the lowest excited state (LUMO). Conjugated double bonds between carbon atoms in organic molecules consist of a σ-bond in the central molecular plane and two π-bonds in parallel planes away from the carbon atoms. These can be seen sketched for a simple ethane molecule in Fig.2.2.1(a). In π-bonds electrons are relatively weakly bound, are delocalized and can contribute to charge transport in an OLED device. Electrons in σ-bonds are more tightly bound. The electronic states of a molecule can be described by wavefunctions, which can be solved using the Schrödinger equation and the Hückel method [81]. The result is that the orbitals split into bonding ground states and anti-bonding excited states of energy order shown in Fig.2.2.1(b). The π-bonds have a weaker overlap of their orbitals and so split in energy less than the σ-bonds The π-orbital is then the filled HOMO, and the π^*-orbital the unfilled LUMO. The $'*'$ superscript denotes an excited state.

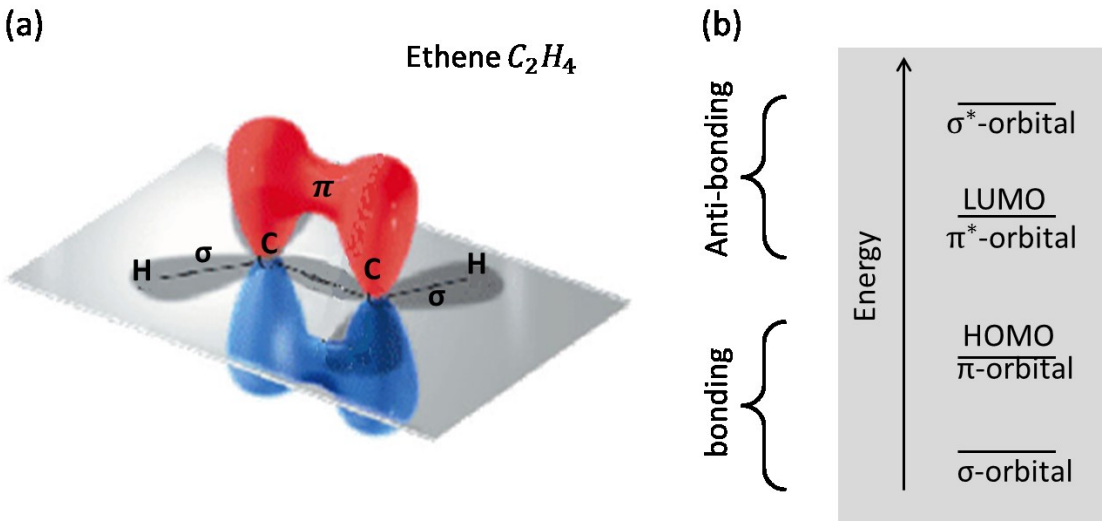

Fig.2.2.1. Ethene molecular orbitals and energy levels. *Part (a) shows the molecular orbitals of Ethene where hydrogen atoms are marked by H and carbon atoms by C. π-bonds/orbitals and σ-bonds/orbitals are marked. (b) shows the relative energy levels of the ground state bonding and excited state anti-bonding orbitals. Orbital figure adapted from [82].*

For organo-transition metal emitters as used in this work, excitations can be described as ligand centered (LC) or metal-to-ligand charge transfer (MLCT). A ligand describes the bond between substituted atoms and the central metal atom

in such molecules. LC excitations are generally of π - π^*character and MLCT excitations are generally of d- π^* character, where the d orbital is a metal centred orbital can occur. A very simplified energy level scheme for such an emitter is illustrated in Fig.2.2.2. In the example of part (a), a single ligand π orbital and one d- orbital are the occupied orbitals, both containing two electrons. The lowest unoccupied orbital is a single π^*. The d^* orbital is assumed energetically too high to be involved.

Electrons and holes are fermions with half integer spin. When these spins are coupled in an exciton, four new combined exciton states are possible; one singlet state denoted for example as ^1MLCT and one triplet state denoted for example as ^3MLCT consisting of three different spin orientations.

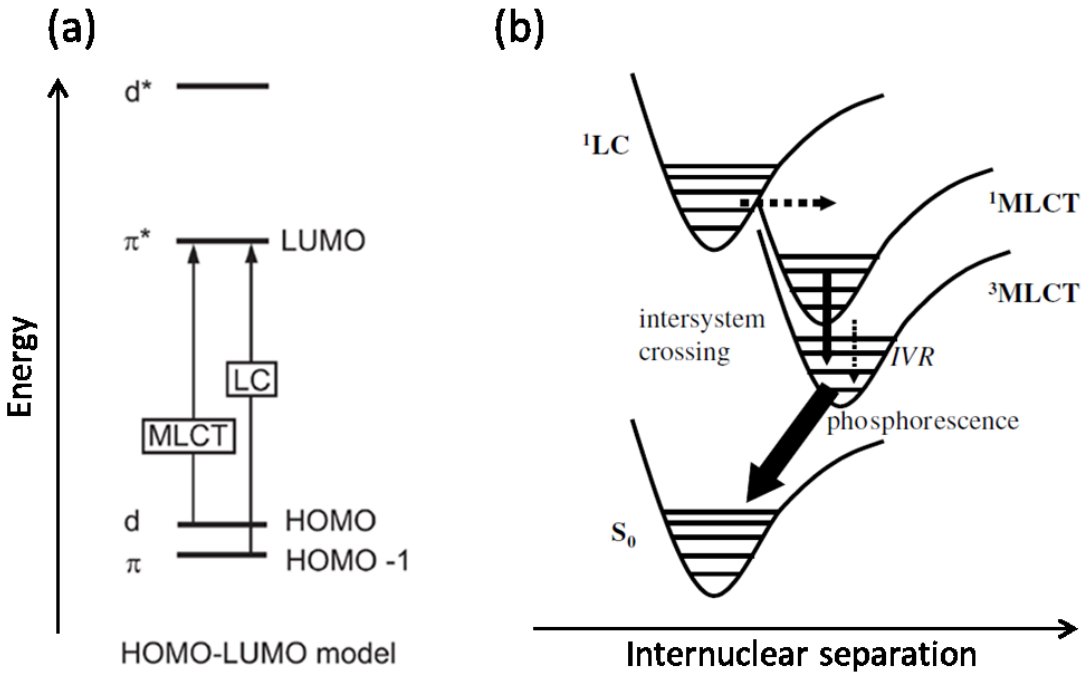

Fig.2.2.2 Excitation and emission in an organo-metallic diatomic molecule. *Part (a) shows the energy levels of molecular orbitals. MLCT and LC excitations are shown. Adapted from [1.4 B]. (b) shows a Jablonski representation of the possible exciton relaxation processes.* $\boldsymbol{S_0}$ *denotes the ground singlet state. IVR is intramolecular vibrational relaxation. The 1 or 3 superscript denotes 1 or 3 degenerate states, 1 for singlet and 3 for triplet. Adapted from [83].*

There is an equal probability that each of the four will be formed in any single charge recombination and so for large numbers of excitons, a singlet to triplet ratio of 1:3 occurs. In the case of optical excitation only singlets will be

formed, since the excitation from the singlet ground state S_0 to the T_1 excited state is spin-forbidden. In the case of phosphorescent emitters, the inter-system crossing (ISC) of the singlet exciton to the lower lying triplet state is usually faster than the emission from the singlet state. [84, 85]. ISC occurs much faster than the μs order phosphorescence in this work, thus this process can be assumed to be instantaneous, and so only triplet excitons will be considered.

Molecular excited states are sketched in Fig.2.2.2(b). A molecule's excited state can have electronic, vibrational, rotational and translational degrees of freedom. Electronic states are separated by a few eV. Each electronic level (denoted by the u-shaped curves representing potential energy versus internuclear separation in Fig.2.2.2(b)) is split into vibrational states (denoted by the horizontal lines in Fig.2.2.2(b)) separated by ~0.1 eV. Each vibrational state can have many rotational and translational states separated by ~0.01eV [86]. The excited state can be seen (denoted by the arrows in Fig.2.2.2(b)) to first decay to the singlet ^1MLCT state and then to the triplet ^3MLCT state via inter-system crossing. The presence of the transition metal in the emitter molecule introduces significant spin-orbit coupling so that this transition becomes allowed [87]. Radiative emission from triplet states is called phosphorescence and takes place on the microsecond scale.

2.3 Emission from a dipole ensemble

Simulation of the classical emission properties of a dipole ensemble will be shown first in Section 2.3. The important quantum microcavity influence on the emission (the Purcell effect) is described in Section 2.4 and the final emitted radiation pattern along with the transient decaying emission under different ensemble averaging assumptions is described in Section 2.5.

In this section the emission properties of a dipole ensemble in an arbitrary layered system will be presented. Emission is modelled using classical harmonically oscillating (Hertz) electrical dipoles in an arbitrary optical layered system. The dipole orientation is described by the dipole moment vector $\boldsymbol{p} = \begin{pmatrix} p_x \\ p_y \\ p_z \end{pmatrix}$. The electromagnetic fields arising from a such a dipole source source are calculated using Green's function approach [88, 89, 90]. The radiation characteristics

(emitted power) of each orthogonal dipole component [40, 91] in an infinite homogenous medium is illustrated in Fig.2.3.1.

The combined emission from many dipoles of different orientation and position is described by introducing an orientational and a spatial distribution function. The dipole moments are assumed to be isotropically oriented in the plane parallel to the layer interfaces. This means that the orientation distribution does not depend on an azimuth angle but only the polar angle φ, illustrated in Fig.2.3.1. The orientation distribution $g(\varphi)$ where φ is the angle that the dipole moment makes with the layer interface normal (Fig.2.3.1) is described. φ is related to the direction of the dipole moment by $sin^2\,\varphi = \frac{p_x^2 + p_y^2}{|p|^2}$ and $cos^2\,\varphi = \frac{p_z^2}{|p|^2}$.

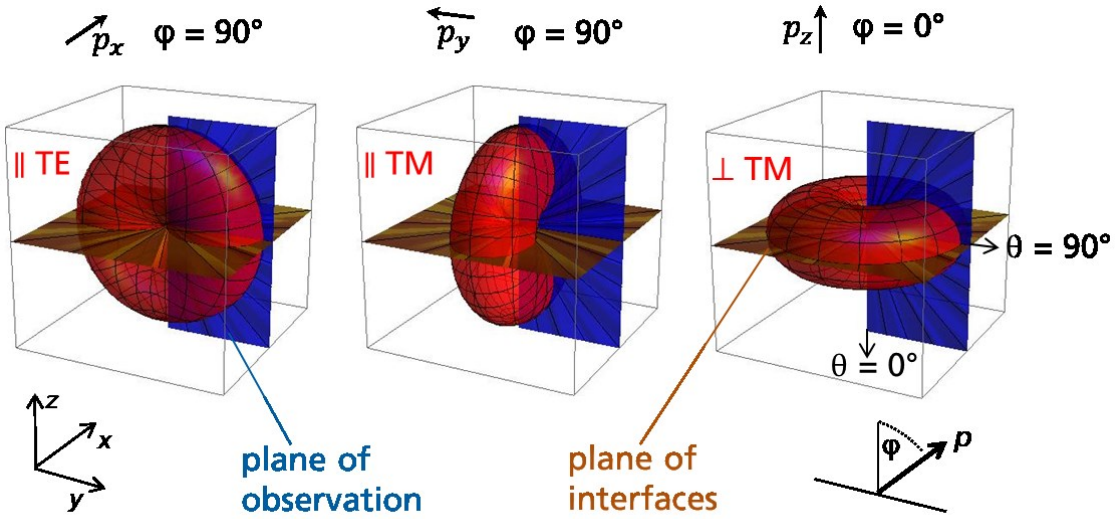

Fig.2.3.1 Radiation characteristics of the orthogonal dipole components. *Emission from the three fundamental orthogonal dipoles* $\boldsymbol{p_x, p_y}$ ***and*** $\boldsymbol{p_z}$ *is shown in an infinite homogenous medium. The three emission contributions which are relevant for OLED modelling are designated ∥ TE, ∥ TM and ⊥ TM where ∥ or ⊥ refers to the dipole orientation with respect to the layer interfaces. TE or TM corresponds to the radiation polarization in the observation plane. The dipole orientation angle* $\boldsymbol{\varphi}$ *is defined as the angle between the layer plane normal and the dipole. The observation angle* θ *is defined as the angle between the z axis (layer system normal) and the observation angle in the observation plane.*

Thus the fraction of all dipole moments that are parallel $p_{\parallel}$ and perpendicular $p_{\perp}$ to the layer interfaces is given by

$$\boldsymbol{p_{\parallel}} = \frac{\mathbf{1}}{|\boldsymbol{p}|^2}\int_{\mathbf{0}}^{\frac{\boldsymbol{\pi}}{\mathbf{2}}}\left(\boldsymbol{p_x^2} + \boldsymbol{p_y^2}\right) . \boldsymbol{g(\varphi)} . \boldsymbol{sin\varphi\, d\varphi} = \int_{\mathbf{0}}^{\frac{\boldsymbol{\pi}}{\mathbf{2}}} \boldsymbol{g(\varphi)} . \boldsymbol{sin^2\varphi} . \boldsymbol{sin\varphi\, d\varphi}$$

$$p_{\perp} = \frac{1}{|p|^2}\int_0^{\frac{\pi}{2}} p_z^2\, g(\varphi) . sin\varphi\, d\varphi = \int_0^{\frac{\pi}{2}} g(\varphi) . cos^2\varphi . sin\varphi\, d\varphi . \qquad (2.3.1)$$

The normalization $\int_0^{\frac{\pi}{2}} g(\varphi).sin\varphi.d\varphi = 1$ ensures that $p_{\parallel} + p_{\perp} = 1$.

The classical, stationary orthogonally decomposed emission pattern of an emitting dipole observed in the far field for an ideal optical layer stack [63] is then given by

$$\boldsymbol{I_{class}^{dipole}(\theta, r_0, \varphi)} =$$

$$\boldsymbol{sin^2\varphi}\left[\boldsymbol{I_{\parallel TE}^{dipole}(\theta, r_0)} + \boldsymbol{I_{\parallel TM}^{dipole}(\theta, r_0)}\right] + \boldsymbol{cos^2\varphi}\left[\boldsymbol{I_{\perp TM}^{dipole}(\theta, r_0)}\right]. \qquad \mathbf{(2.3.2)}$$

Where $\boldsymbol{r_0}$ is the position of the dipole and θ is the angle of detection.

Similarly, the total emitted power density of an arbitrarily oriented dipole can be decomposed into the three orthogonal contributions [63] as

$$\boldsymbol{a_{class}^{dipole}(r_0, \varphi)} =$$

$$\boldsymbol{sin^2\varphi}\left[\boldsymbol{a_{\parallel TE,tot}^{dipole}(r_0)} + \boldsymbol{a_{\parallel TM,tot}^{dipole}(r_0)}\right] + \boldsymbol{cos^2\varphi}\left[\boldsymbol{a_{\perp TM,tot}^{dipole}(r_0)}\right]. \qquad \mathbf{(2.3.3)}$$

Eq. 2.3.2 and Eq.2.3.3 are normalised to the totally irradiated power of a dipole in a homogenous medium. Eq. 2.3.2 shows that for such an isotropic *x-y* plane system, the emission pattern can be equivalently simulated with only the knowledge of the relative contributions of parallel and perpendicular dipole moments as with the detailed orientation distribution $g(\varphi)$. The orientation ratio $p_{\parallel}: p_{\perp} = 2 : x$ is adequate ensemble orientation information to completely simulate the emission pattern. An isotropic ensemble orientation would be fully described by an orientation ratio of $p_{\parallel}: p_{\perp} = 2 : 1$.

A typical optimized OLED device structure is sketched in Fig.2.3.2(a). Optimized in this case means that the device emitter-cathode separation is set to allow for constructive interference of the forward propagating wave with the cathode-back-reflected wave in the emission direction, resulting in maximum light outcoupling. If the OLED device active area has a homogenous charge recombination in the *x-y* plane, a spatial distribution of emitters along the *z*-axis can fully describe the emitter positions. This distribution function is called the emission zone profile *N(z)* (sketched in Fig.2.3.2(a)) which is normalized as $\int N(z)dz = 1$. In this way, the

dipole position $\boldsymbol{r_0}$ in Eq. 2.3.2 reduces to a dependency on position *z*. A single point profile of the emission zone N(z) in the centre of the EML is used in the simulations of Fig.2.3.2. The electric field components as observed in the observation plane from each orthogonal dipole component are designated || TE, || TM and ⊥ TM, where TE is the transverse electric field polarization and TM is the transverse magnetic field polarization. || or ⊥ refers to the dipole orientation with respect to the layer interfaces. Observation of the combined dipole emission at different observation angles results in detection of different parallel and perpendicular emission contributions.

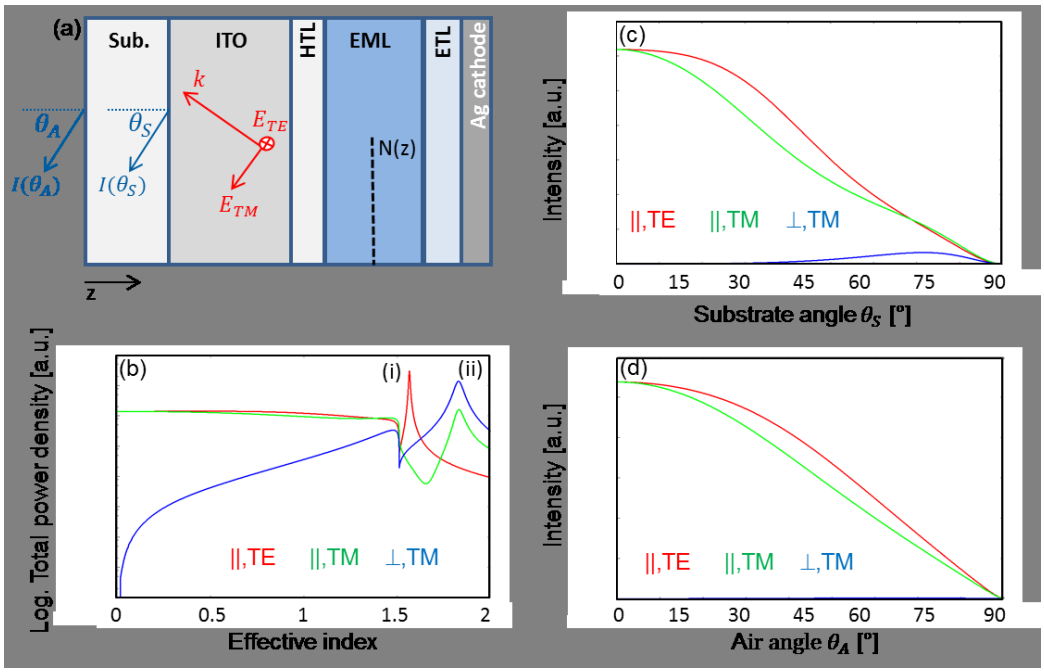

Fig. 2.3.2 Dipole emission from an OLED. *(a) shows a scheme of an OLED thin layer system featuring the emission zone profile N(z) (dashed line) and the dipole orientation at angle* $\boldsymbol{\varphi}$ *to the interface normal in the EML. The electric field polarizations* $\boldsymbol{E_{TE}}$ *and* $\boldsymbol{E_{TM}}$ *are sketched along with the wavevector k which indicates the direction of propagation of the relevant plane wave. The intensity, detected in the plane of observation at an angle to the interface normal is shown in the substrate* $\boldsymbol{I(\theta_S)}$ *and in air* $\boldsymbol{I(\theta_A)}$*. (b) shows the total power density emitted versus effective index, (c) shows the intensity emitted into the substrate and (d) shows the intensity emitted into air. || TE and || TM and ⊥ TM dipole emissions are colour-coded according to the legends of parts (b,c,d).*

A classical simulation of the total power density in air of Eq. 2.3.3 for an isotropic ensemble of emitters for varying effective index is shown in Fig.2.3.2(b). The

effective index is the normalized transverse wavevector component of the relevant plane wave. For example, in each layer it can be expressed by $n_i \sin \beta_i$; where n_i is the refractive index and β_i is the propagation angle in the medium. An effective index of emission in air is in the range 0…1, in the substrate 1…1.5 and high-index organic layers >1.5.

The emitted intensity from such an OLED stack is shown in the substrate in Fig.2.3.2(c) and in air in Fig.2.3.2(d). These emitted intensities result from the emission characteristics of the three dipole contributions of Fig.2.3.1 combined with multilayer interference effects. In Fig.2.3.2(b) at effective indices >1.5, so observation at large angles θ in Fig.2.3.1, two discrete layer stack interference modes are observed; the fundamental TE mode (i) and the plasmon modes (ii) excited by || TM and ⊥ TM. Plasmon modes are interface modes which, in this coordinate system can only couple to TM radiation. For an effective index approaching 0, || TE and || TM have similar total power density due to their similar dipole emission characteristics at low angles (see Fig.2.3.1). ⊥ TM emission power density however vanishes at an effective index of 0, again due to the dipole emission characteristics seen in Fig.2.3.1.

The emitted intensity versus observation angle graphs Fig.2.3.2(c) and (d) again show the same || TE and || TM constructive interference emission for observation at low angles. Conversely, ⊥ TM emission at low angles is almost completely suppressed due to the dipole emission characteristics and also due to the opposite interference conditions with respect to || TE and || TM [40]. Larger angle emission shows Lambertian-like behaviour mainly due to outcoupling of the light from the high-index organic stack to the substrate or air. For most angles || TE > || TM due to the dipole emission characteristics of Fig.2.3.1. For substrate emission $\theta \geq 60°$ cavity interference effects are visible. At large angles, there is more destructive interference for TE radiation than TM, shown by the larger || TM emission at $\theta \geq 60°$. At these angles, the TM phase is much less detuned than for TE upon reflection at the cathode, affecting interference. Additionally, at large angles, TE radiation exhibits a larger reflectivity at the anode and the cathode than TM radiation, and so experiences a larger phase detuning inside a rather resonant cavity.

Important effects of the structured environment in a real OLED on the quantum mechanical emission process is dealt with in terms of emitter lifetimes in Section 2.4.

2.4 Intrinsic quantum efficiency and emitter decay lifetime

In Section 2.3 the emission characteristic of an ideal continuously oscillating dipole was shown (Fig.2.3.1). A real emitter however, will spontaneously relax with a rate Γ. Separating the relaxation rates into a radiative rate Γ_r and a non-radiative rate Γ_{nr} one can define a probability that a single emitter will emit a photon in relaxation as the intrinsic quantum efficiency q.

$$\boldsymbol{q} = \frac{\boldsymbol{\Gamma_r}}{\boldsymbol{\Gamma_r + \Gamma_{nr}}}, 0 \leq q \leq 1 \tag{2.4.1}$$

q is a material property which can be lowered by increasing Γ_{nr} via e.g. the exciton dynamic processes described in Section 2.2.1.

In a real OLED stack, it is well known that an optical layer stack environment can alter the emission probability of a dipole via the Purcell effect [65, 92, 93, 94]. The non-radiative lifetime is assumed to not be affected by the Purcell effect. The intrinsic quantum efficiency is then

$$\boldsymbol{q}^* = \frac{\boldsymbol{\Gamma_r^*}}{\boldsymbol{\Gamma_r^* + \Gamma_{nr}}}, 0 \leq q^* \leq 1 \tag{2.4.2}$$

where Γ_r^* represents the radiative decay rate altered by the Purcell effect.

The variation of the radiative rate due to the Purcell effect can be quantified by a Purcell factor F [95]. To quantify the factor F, the equivalence of the spontaneous emission probability via a dipole transition and the radiated power of a classical dipole source in a microcavity is used [93]. The factor that the probability for the excited state to emit a photon is changed by is the same as the factor that the microcavity changes the total power emitted by the dipole according to

$$\boldsymbol{\Gamma_r^* = \mathrm{F}\Gamma_r = \frac{p_{tot}^{cav}}{p_{tot}^{hom}}\Gamma_r} \tag{2.4.3}$$

where p_{tot}^{cav} is the total radiated power in the microcavity and p_{tot}^{hom} is the total radiated power in the homogenous emitter medium, both calculated as in Eq.2.3.3.

The relative transition rate between the two systems is then

$$\boldsymbol{\Gamma_{rel}} = \frac{\boldsymbol{\Gamma^*}}{\boldsymbol{\Gamma}} = \frac{\boldsymbol{\Gamma_r^* + \Gamma_{nr}}}{\boldsymbol{\Gamma_r + \Gamma_{nr}}} = \mathbf{1} + \mathbf{q}\left(\frac{\boldsymbol{p_{tot}^{cav}}}{\boldsymbol{p_{tot}^{hom}}} - \mathbf{1}\right). \quad (2.4.4)$$

Using Eq.2.3.3 and Eq.2.4.4, the relative emission rate can be decomposed into the relative emission rate of the strictly parallel (||) and perpendicular (⊥) emitters according to

$$\boldsymbol{\Gamma_{rel}(\varphi, q)} = \boldsymbol{\Gamma_{rel}^{\parallel}(q)} \,.\, \boldsymbol{sin^2\varphi} + \boldsymbol{\Gamma_{rel}^{\perp}(q)} \,.\, \boldsymbol{cos^2\varphi} \quad (2.4.5)$$

This relative rate is then related to the inverse lifetime as $\tau_{rel} = \frac{1}{\Gamma_{rel}}$.

In this work the emitted intensity versus time when steady state device operation is turned off will be investigated. For such an excited emitter ensemble, the rate of change with time of the excited population M is given by

$$\frac{\boldsymbol{dM}}{\boldsymbol{dt}} = -(\frac{\mathbf{1}}{\boldsymbol{\tau_r^*}} + \frac{\mathbf{1}}{\boldsymbol{\tau_{nr}}})\boldsymbol{M} \quad (2.4.6)$$

Integrating with respect to time gives the solution for t >0:

$$\boldsymbol{M(t)} = \boldsymbol{M_0 e^{-(\frac{1}{\tau_r^*} + \frac{1}{\tau_{nr}})t}}. \quad (2.4.7)$$

Where M_0 is the intial population at t =0

So the luminescence decay measured is not only influenced by the radiative decay time but the non-radiative decay time also. The decay is actually decribed by a total decay lifetime τ_{tot} where $\frac{1}{\tau_{tot}} = \frac{1}{\tau_r^*} + \frac{1}{\tau_{nr}}$.

The two processes cannot be distinguished when measuring the emitted light, as they are inseparably connected. τ_{tot} is the experimentally accessible lifetime and will be referred to as the emission lifetime.

2.5 OLED emission pattern

The final emission from the OLED should take into account emission from (i) dipoles at all positions of the emitter ensemble as given by the weighting function N(z), (ii) dipoles of all orientations given by the orientation distribution g(φ), (iii) the emitter intrinsic spectrum S(λ), where λ is the wavelength of the radiation. Normalization of all distributions to 1 ensures that the integrated distribution

weight gives a single emissive event in total. The emission pattern is calculated as the incoherent superposition of all contributions according to

$$\boldsymbol{I^{cav}(\theta,\lambda)}$$

$$\boldsymbol{= S(\lambda)\int_z \int_\varphi N(z)g(\varphi)\,\frac{I^{dipole}_{class}(\theta,\lambda,z,\varphi)}{\Gamma_{rel}(q,z,\varphi)}\,\sin(\varphi)\,d\varphi\,dz}$$

$$\boldsymbol{= S(\lambda)\left\langle \frac{I^{dipole}_{class}(\theta,\lambda,z,\varphi)}{\Gamma_{rel}(q,z,\varphi)} \right\rangle_{\varphi,z}} \qquad (2.5.1)$$

Where $\langle\ \ \rangle_{\varphi,z}$ means averaged over φ and z

The relative emission rate Γ_{rel} takes the Purcell effect into account by normalising the emitted power from the dipole. For the low q case, the influence of the Purcell effect on the emission rate is minimal and the emission is well described by $I^{dipole}_{class}(\theta,\lambda,z,\varphi)$, see Eq.2.4.4. For a high q case, which is the probable case in useful OLED devices, the Purcell effect strongly influences $\Gamma_{rel}(q,z,\varphi)$. $\Gamma_{rel}(q,z,\varphi)$ depends on the whole intrinsic emission spectrum, but is well approximated at the mean wavelength of the relatively narrow intrinsic emission spectrum, as was performed in the simulations of this work.

Two different limiting types of ensemble orientation averaging, $\langle Y\rangle_\varphi = \int Y(\varphi).g(\varphi).sin\varphi.d\varphi$ of an arbitrary quantity Y can be proposed. Combining Eq.2.4.7 and Eq.2.5.1 yields the temporally resolved static intensity I_S of the emitting molecular ensemble according to

$$\boldsymbol{I_s(\theta,t,q) = \langle I_{class}(\theta,\varphi)\,.\,\tau_{rel}(\varphi,q)\,.\,e^{-t/\tau(\varphi,q)}\rangle_\varphi} \qquad (2.5.2)$$

This description assumes each molecule to exhibit a unique decay rate that depends on its individual fixed angle of orientation φ and will be referred to "static" ensemble average. Such temporal behavior has been observed in photo luminescing polymer films doped with Rhodamine 6G, which is assumed to have a single emission transition dipole moments and has an emission lifetime of approximately 3 ns [91, 96, 97]. It yields, in general, non-exponential time traces of emitting ensembles [98].

Contrarily, Europium complexes of 1 ms emission lifetime are well known not to exhibit orientation dependent emission lifetimes in the vicinity of metal mirrors

[92]. The average decay rate observed experimentally can be described by the "fluctuating" ensemble average

$$\boldsymbol{I_s(\theta, \mathrm{t}, q) \sim \langle I_{class}(\theta, \varphi)\rangle_{\varphi} \langle\, \tau_{rel}(\varphi, q)\rangle_{\varphi} \,.\, e^{-t.\ \langle \frac{1}{\tau(\varphi,q)}\rangle_{\varphi}}} \qquad \textbf{(2.5.3)}$$

This observation can be associated with thermal motion of the emitting ion during the emission lifetime. With regard to electroluminescent phosphors, such a fluctuating average has been reported for single homoleptic Iridium complexes [99] due to the fact that degenerate transition dipole moments can be assigned to each one of the three ligands. So depending on the nature of the emitting species and the orientation ensemble average, temporal experiments will lead to different interpretations. In Eq. 2.5.3 all emitters would have the same emission lifetime. In Eq. 2.5.2, in general, a multi-exponential emission decay time would be observed depending on the magnitude of the orientational lifetime differences. Such a multi-exponential decay is most apparent with large lifetime differences between parallel and perpendicular emitters for example.

If the Purcell effect is different in parallel and perpendicular directions ($\Gamma_{rel}^{\parallel} \neq \Gamma_{rel}^{\perp}$) and static averaging applies to the emitter ensemble, then the Purcell effect on the emission patterns of the emitters will vary with the angle of orientation φ. In this case, the orientation ratio does not give enough information to simulate the ensemble emission pattern, the angular distribution of the emitters or the detailed $g(\varphi)$ must be known. For devices featuring a strong Purcell effect which affects parallel and perpendicular emitter dipoles quite differently, emission lifetimes for ensembles having thin or wide orientation distributions could become distinguishable.

3. DEVICES AND METHODS

In this chapter the devices that were used in this work are introduced and the methods used in the investigation of these devices are explained. Firstly, in Section 3.1 the manufacture and structure of the devices is outlined followed by an overview of used material energy levels. Then, in Section 3.2 experimental procedures are outlined. Next, in Section 3.3 the established microcavity inverse

light outcoupling approach is oultined and finally fitting and error analysis is described in Section 3.4

3.1 Device fabrication, structure & layer characterization

3.1.1 Device fabrication, structure & material energy levels

OLED devices were prepared by thermally evaporating organic and metal layers sequentially onto commercial Indium Tin oxide (ITO) coated substrates under high vacuum conditions by OSRAM Opto Semiconductors GmbH, Regensburg, Germany. The layered structures were fabricated at a base pressure of $\sim 10^{-6}$ mbar. Organic layers were deposited at a rate of ~0.07 nm/s. Ag cathodes were deposited at a rate of 0.2 nm/s for the dual-emitter devices and 0.05 nm/s for the single emitter devices. For the thin metal interlayer, the Ge part was deposited at 0.02 nm/s and the Ag part at 0.05 nm/s. ETL and HTL layers were doped via co-evaporation in order to improve electron and hole transport. This technique was also used for incorporating emitters into EML hosts. After deposition of the cathode all devices were encapsulated along with a moisture absorbing getter under a glass cover. Each series was produced on a single substrate. One shadow mask was used for all organic layers and a different shadow mask was used to deposit the cathodes. For the deposition of the ETLs, different shadow masks were used in order to realize different ETL thicknesses. Hence, it was ensured that the thickness of all layers in the stack, apart from the ETL, are identical for all devices of one series. Measured device material energy levels are given in Table 3.1.1.

HOMO energy levels given are an average of cyclic voltammetry and Riken AC2 photoelectron spectroscopy measurements by the material manufacturer, whereby the energy of electrons ejected from the material under UV irradiation are measured. LUMO levels were estimated by adding band gap values extracted from the absorption edge of the material emission spectrum to these HOMO levels. This is an indirect measurement which assumes that the optical energy level difference is also the charge transport energy level difference, so some caution should be assumed in the use of these values. Triplet energy values were extracted from photoluminescence spectra measured also by the material manufacturer.

Material	HOMO [eV]	LUMO [eV]	Triplet energy [eV]	Transport property
α-NPD	-5.5	-2.4	2.2	Hole
HBL	-6.05	-2.75	2.5	Electron
$Ir(MDQ)_2acac$ (red)	-5.2	-2.7	1.9	Electron
$Ir(ppy)_3$ (green)	-5.3	-2.8	2.3	Hole

Table 3.1.1 Material properties of relevant device materials. *Accuracy of HOMO/LUMO values is estimated using the error of cyclic voltammetry and Riken AC2 photoelectron spectroscopy measurements, ±0.15 eV. Triplet energy accuracy is estimated to be ±0.1 eV, the T1-onset and 0-0 transition measurement error. The average room temperature electron thermal energy is ~ 0.026 eV.*

3.1.2 Single red emitter OLED structure

The structure of the single red emitter OLEDs is shown in Fig.3.1.2.1(a). Layers are chosen to perform charge transport and blocking functions as outlined in Section 2.1. The semi-transparent Ag:Ge interlayer introduces plasmon losses mostly for perpendicular emitter components as will be discussed in more detail in Section 4.6. The HBL and host material of the EML are composed of N,N'-bis(naphthalen-1-yl)-N,N'-bis(phenyl)-2,2'-dimethylbenzidine (α-NPD, shown in Fig.3.1.2.2(a)). The red heteroleptic triplet emitter iridium(III)bis(2-methyldibenzo-[f,h]quinoxaline)-(acetylacetonate) ($Ir(MDQ)_2acac$, shown in Fig.3.1.2.2(b)) is doped at 3% (w/w) into this host to form the EML. Other materials used are proprietary. $Ir(MDQ)_2(acac)$ is a typical emitter in today's high efficiency OLEDs and the mean wavelength of the emission spectrum is λ=630 nm [100, 101].

Devices with three different HTL spacer thicknesses (d_{sp}=10 nm, 30 nm, or 75 nm) were made. Half of these devices were control devices without the Ag:Ge layer so that devices with (Devices B) and without (Devices A) an additional metal layer can be compared directly. Regarding previous devices from the same manufacturer without such an thin metal interlayer [47], the present devices differ in that the HTL doping concentration has been increased to still permit device operation with the thin metal layer inside the HTL, emitter concentration has been

reduced to 3% (w/w) and the device active area has been increased to 1.81 cm^2 (1.45 cm x 1.25 cm) to prevent possible short circuits due to the additional metal layer.

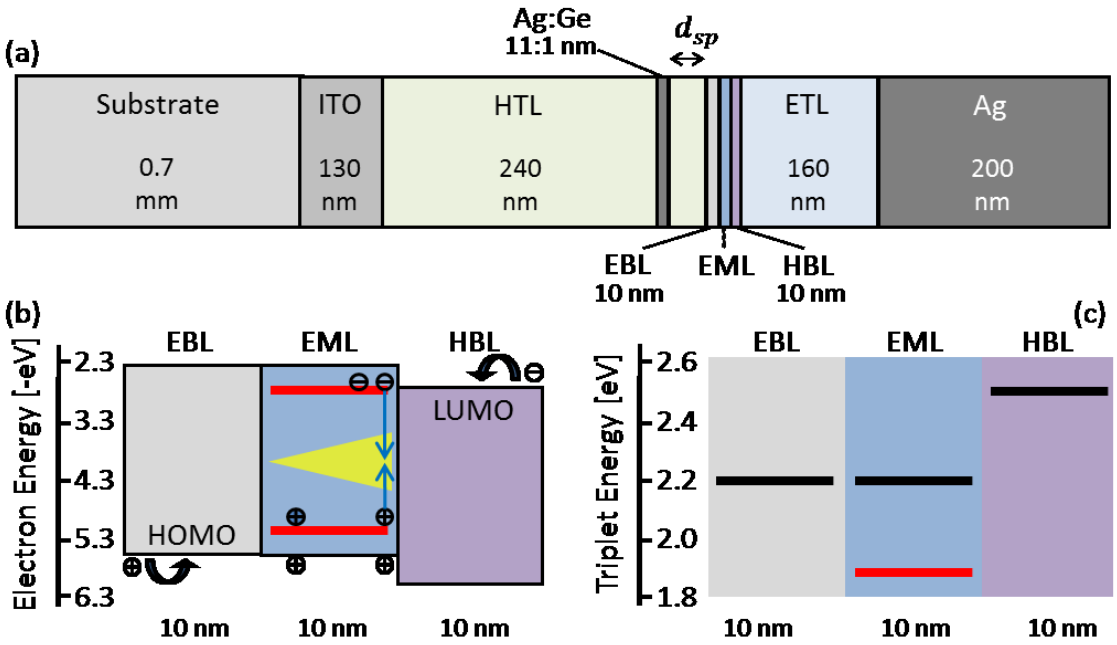

Fig.3.1.2.1 Single emitter device structure and energy levels. *Part (a) shows device layers and thicknesses shown to scale.* $\boldsymbol{d_{sp}}$ *is the thickness of a variable HTL spacer layer, defining the EML – Ag:Ge distance. (b) shows a simplified drawing (neglecting band bending effects) of the HBL, EML and EBL HOMO and LUMO energy levels (taken from Table 3.1.1). Red lines represent the doped emitter and black lines represent the host materials. Circles enclosing a minus and a plus show likely electron and hole build-up respectively. The yellow shape roughly indicates the predicted region of recombination. The blue arrows indicate a recombination event. (c) The triplet energy level structure (taken from Table 3.1.1) near the EML is shown. Again, red lines represent the doped emitter and black lines represent the host materials*

The 160 nm thickness of the electron transport layer (ETL) ensures significant emission from perpendicularly aligned emitters, as will be discussed in Section 3.3. The EML and neighbouring layers' HOMO and LUMO energy structure are shown in Fig. 3.1.2.2(b). The triplet exciton energy level structure is shown in Fig.3.1.2.1(c).

The yellow area of Fig.3.1.2.1 shows the recombination area estimated from the energy levels and the literature. Two recent papers [21, 47] give an EZP for a single emitter $Ir(MDQ)_2acac$ OLED to be quite constant across the EML. For a more

specific expected EZP for our OLED, firstly, the likely areas of hole density in the operating device was predicted. In Fig.3.1.2.1(b) it can be seen that holes can hop at the HOMO level of α-NPD, a good hole transporter [102], into the EML.

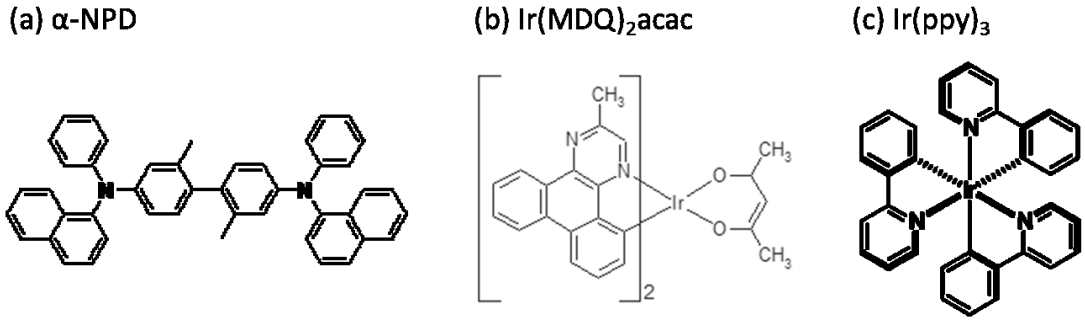

Fig.3.1.2.2 Chemical structure sketches of materials. *(a) shows the chemical structure of the EML host material [103], (b) shows the chemical structure of the EML dopant emitter material [104] and (c) shows the chemical structure of the green emitter of the next section 3.1.3 [105].*

In the EML it is energetically favourable for the holes to jump to the emitter HOMO. The successful transport of holes across the EML HOMO levels is a contest between the availability of low concentration (3%) emitter molecules to accept holes and the well transporting α-NPD. Meerheim et al. [25] state that a $Ir(MDQ)_2acac$ concentration of 10% can give hole transport. Diez et al. [24] in a comparable hole transporting system to ours, but with 5% emitter, state that holes accumulate more towards the cathode side of the EML. In conclusion, here holes can be present on the emitter for recombination across the EML, but likely more to the cathode side.

Secondly the likely areas of electron density in the operating device was predicted. From Fig. 3.1.2.1(b) it can be seen that electrons can hop at the LUMO level of $Ir(MDQ)_2acac$, an electron transporter at 10% concentration [25], but here we have low concentration, possibly hindering transport across the EML. At room temperature not many electrons are expected to have the thermal energy to hop onto the α-NPD LUMO. Again, Diez et al. [24] state that at similar low concentrations (5%) to our device, electrons accumulate more to the cathode side of the EML, but that the EZP extends fully across 11 nm of the EML So, in conclusion, an EZP spreading across the EML but with more weight to the cathode side is predicted from the literature. The triplet levels of α-NPD and the HBL are

sufficiently higher than the emitter so that negligible triplet transfer to non-emitter molecules should occur, which would lead to increased exciton quenching.

3.1.3 Dual red & green emitter OLED structure

The structure of the dual green and red emitter OLEDs is shown in Fig.3.1.3. Layers perform functions as outlined in section 2.1.

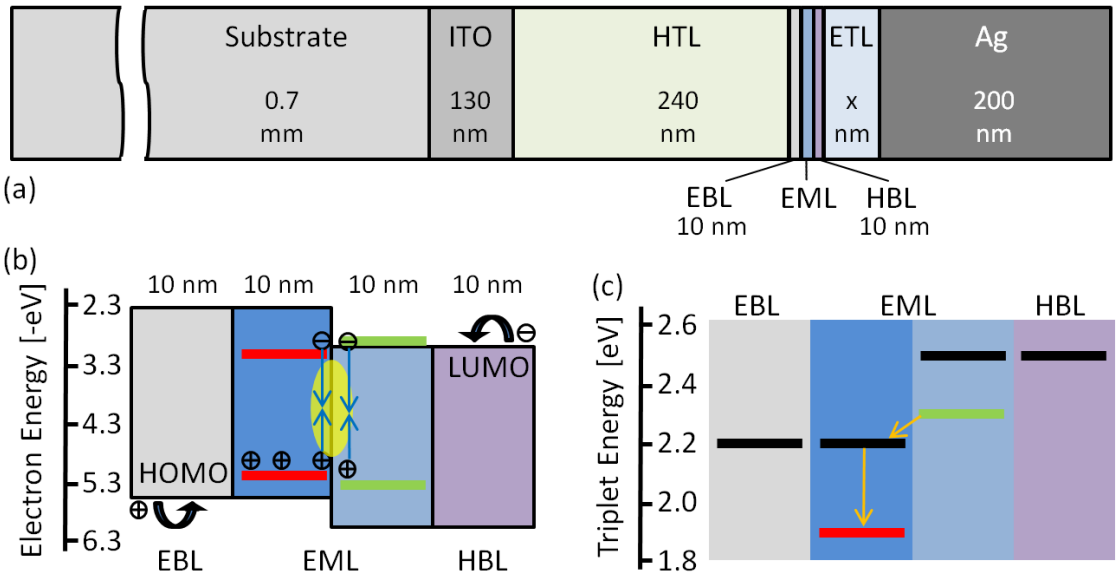

Fig.3.1.3 Dual emitter device structure and energy levels. *In part (a) Device layers and thicknesses are shown to scale. x dictates the thickness of a variable ETL layer, defining the EML – Ag cathode distance. (b) The HBL, EML and EBL HOMO and LUMO energy levels (taken from Table 3.1.1) and the expected charge build-up region (in yellow) are shown. Blue arrows depict recombination. Red and green lines represent the emitter dopants and black lines the host materials. Circles enclosing a minus and a plus show likely electron and hole build-up respectively. In (c) the triplet energy level structure (taken from Table 3.1.1) near the EML is shown. Orange arrows show triplet transfer to the red emitter. Black lines show the energy levels of the host materials.*

The active emissive area of this device series is circular of radius 0.125 cm, giving an area of 0.049 cm^2. The EML contains the green emitter $Ir(ppy)_3$ (fac-tris(2-phenylpyridine)iridium, shown in Fig.3.1.2.2(c)) doped at 11% (w/w) and the red emitter $Ir(MDQ)_2acac$ doped at 5% (w/w) into the host. $Ir(ppy)_3$ is a common emitter in high efficiency OLEDs with a mean wavelength of emission of ~ 550 nm [106]. The red doping concentration is lower because triplet transfer from the green to the red emitter is favoured [24], as can be seen in Fig.3.1.3(c). Other

materials used are proprietary. Devices with different ETL values of 37 nm, 80 nm, 124 nm, 165 nm, 206 nm, 250 nm, 285 nm, and 325 nm were manufactured.

The yellow area of Fig.3.1.3(b) shows the recombination area estimated from the energy levels and the literature. Diez et al. analysed a device with the same structure, materials and concentrations [24]. They reported an emission zone located at the interface of the red and green EMLs and extending 11 nm in each direction from this interface.

3.2 Experimental procedures

3.2.1 Layer characterization

Layer thicknesses have been extracted from spectral reflectivity measurements performed after each layer deposition step as well as with the complete devices by OSRAM Opto Semiconductors GmbH, Regensburg, Germany and also at Fraunhofer IOF Jena, Germany. Data simulated using in-house developed software [107] was compared to the experimental data for each deposition step and for the complete devices. The complex refractive indices of all device thin film materials were measured using a dispersion-model-free approach utilizing reflection-transmission-spectroscopy of single supported films [108]. This technique is perfectly suited for organic thin film materials due to several reasons: reflection and transmission can be conveniently measured with common spectrophotometers (a Lambda 900 from Perkin Elmer here). Additionally one does not need to assume a dispersion model because the calculation of the thin film material constants $n(\lambda)$ and $\kappa(\lambda)$ is carried out by direct inversion. A further discussion of the method can be found in Ref. [108]. Using this approach, all organic materials, ITO layers, and substrates were characterized (data not shown). The optical properties of the Ag cathodes are taken from Palik [109]. The optical properties of the thin metal interlayer in the HTL are discussed in more detail in section 4.1.

3.2.2 General measurement setup

The general measurement setup for measurements of this work is shown in Fig. 3.2.2. The OLED was placed in a holder which featured x,y and z direction linear translation stages. This holder was attached onto a goniometer (resolution

Δθ~0.5°, CR1/MZ7E, Thorlabs). The centre of the OLED active area was aligned to the goniometer centre of rotation using by adjusting the linear translation stages. The centre of the OLED active area was also aligned to be on the fibre entrance optical axis. Rotating a wire grid linear polarizer (NT47-101, Edmund Optics) through 90° allows one to switch the detection polarization between TE and TM.

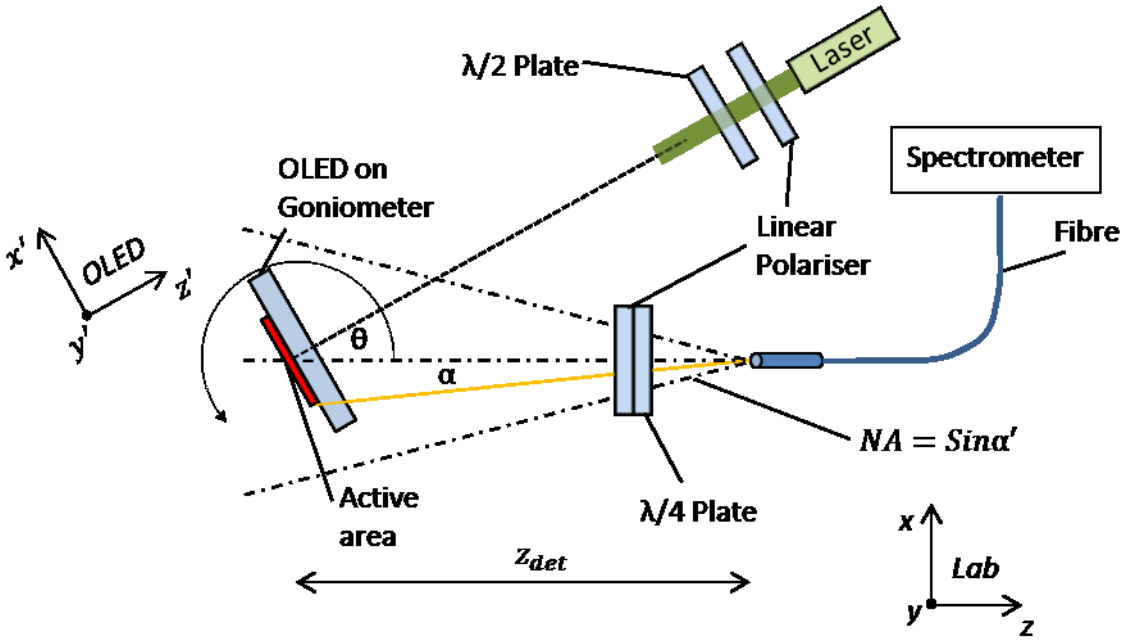

Figure 3.2.2 General OLED emission measurement setup. *α depicts the maximum entrance angle of detection and θ is the OLED observation angle.* $\boldsymbol{z_{det}}$ *depicts the distance from centre of the OLED active area to the fibre collimator entrance. The OLED coordinate system and the lab coordinate system are distinguished. The numerical aperture (NA) of the fibre is marked. A large* $\boldsymbol{z_{det}}$ *is chosen so that* $\boldsymbol{\alpha' > \alpha}$*. The laser and associated optics are always oriented normal to the OLED layers at an angle of* $\boldsymbol{\theta = 0°}$.

An achromatic quarter wave plate (AQWP05M-630, Thorlabs) is fixed to the fibre side of this linear polarizer at an angle of 45° to the linear polarizer axis to convert all linear polarizated light to circular. This is so that the fibre (200 μm core diameter, Δλ resolution ~4nm, NA =0.22, M17L02, Thorlabs) does not modulate TE and TM radiation differently as it travels to be detected at the coupled spectrometer (SD2000, Ocean Optics). A standard spectrometer integration time of 8000 ms was used for all measurements. A thin layer of opaque paint is applied to the OLED sides to block scattered and substrate modes from the side of the device,

particularly significant when the observation angle θ approaches 90°. The different measurement procedures used during this work will be individually described in the following subsections.

3.2.3 Steady-state electroluminescence measurements

The measurement setup is that shown in Fig.3.2.2. The laser is not used for excitation. Instead, a current source (GS610, Yokogawa) was used to apply a constant current through the OLED for the duration of the measurement. A current density of 5 mA/cm^2 was used unless otherwise stated. To ensure it remained constant and that no degradation occurred, which would skew the data, the voltage over the OLED was read at the beginning and end of each measurement. The angular emission spectra were measured from λ= 380 nm … 780 nm at intervals of 2 nm and from θ= -88° … +88° at an intervals of 4°.

3.2.4 Photoluminescence measurements

For photoluminescence measurements the (collimated) λ= 515 nm diode laser was used equipped with a linear polarizer and a half wave plate for excitation. The laser source was modulated with square pulses of 100 µs duration and 5 kHz repetition, resulting in 30mW cw equivalent power. No current was electrically applied to the OLED. The linear polarizer "cleans up" the elliptically polarized laser emission to linear polarized emission. The half wave plate allows for a rotation of the polarization of the laser emission with minimal changes to the intensity (< 5%). A long pass filter (Schott OG 590) was applied in front of the spectrometer fibre entrance to block scattered laser light, and the simulated emission spectra were corrected for this using the measured filter transmission function.

3.2.5 Transient luminescence measurements

Transient luminescence time traces were recorded with pulsed electrical or laser excitation using a photomultiplier tube (Hamamatsu R6356, 2 ns response) connected to an oscilloscope (LeCroy WR 6051A, 2 ns resolution) as a detection system instead of the fibre spectrometer. Transient EL time traces were recorded following Hosokawa et al. [110] by exciting the OLED with square pulses of 1 kHz repetition rate, 4 V amplitude (resulting in 50 mA/cm^2 in the device) and 30 µs duration (Agilent 33250A function generator of resolution 12.5 ns). These conditions ensure steady state EL operation at the end of a single pulse. For

transient photoluminesce measurements, the same laser conditions as in Section 3.2.2 were used. The Schott OG 590 filter was used again for measurement of photoluminescence lifetimes. Emission lifetimes were extracted from the measurement data using Eq.2.4.7.

3.3 Single emitter device active optical property extraction

The extraction of OLED optical properties is performed for single emitter devices following the methods outlined in the dissertation work of M. Flämmich [63]. In this method, the emission pattern is simulated whilst varying the individual optical properties of the emission system and the result is compared with the experimental pattern to give information about these properties. Simulation of OLED emission media was performed as outlined in Section 2.5 using in house software [63]. OLED optical properties can be distinguished as passive: (layer dispersions and thicknesses) and active: (emission zone profile (EZP), the emitter intrinsic spectrum and the emitter orientation ratio or distribution). Prior to an active emitter property analysis, passive properties were measured as outlined in Section 3.2.1.

An important conclusion of the dissertation work of M. Flämmich was that devices optimised for maximum light outcoupling are not the most sensitive in extracting the active optical properties. The device ETL thickness (~ the cathode-emitter distance) can be altered to tune the microcavity interference conditions to prefer different types of emission. A well selected thickness of the ETL yields a microcavity interference minimum in the emission spectra. Here, the majority of light containing little information on the EZP is supressed, leaving mostly light sensitive to EZP changes. “Dark” OLEDs with such an ETL thickness also ensure significant emission from perpendicularly aligned emitters, which is critical to enabling the quantification of the orientation ratio (Section 2.3). OLEDs with a microcavity optimised for the highest intensity emission should be optimised for extracting parallel emission most efficiently. This is because parallel emitters have a generally more efficient outcoupling due to low emission angles with the stack normal and there being two parallel directions and only one perpendicular in the defined coordinate system. These optimised OLEDs will have a quite low perpendicular emission as parallel and perpendicular emitters have opposite

interference conditions [93]. Comparable levels of parallel and perpendicular emission can be established by setting the microcavity emitter-cathode distance (~ETL thickness) to allow for constructive interference and preferred emission for perpendicular emitters. An overview detailing the necessity of using adapted devices in extracting the EZP and orientation ratio is given in [40]. An example of extracting the EZP from the experimental emission spectra of optimised and dark devices is given in [111]. An example of extracting the orientation ratio from the experimental emission spectra of optimised and dark devices is given in [112]. The important aspects of these extraction methods are now summarized for each active property.

The EZP of the OLED is defined by a weight (defining the relative amount of light emitted) for each source position (Eq. 2.5.1). It is determined by fitting the sum of the simulated angular emission spectra from each emission location in the device to the experimentally measured angular electroluminescence (EL) spectrum, while varying the weights. Only TE polarized light is considered here, which is emitted only by emitter transition dipole moment (TDM) components parallel to the interfaces (Eq. 2.3.2). Therefore the effect of emitter orientation distribution is negligible and material birefringence has no effect on the results.

Once the EZP is known, the intrinsic spectrum $S(\boldsymbol{\lambda})$ of the emitter can be extracted from TE polarized emission. If $S(\lambda)$ in Eq.2.5.1 is set as a constant, dividing the angularly averaged experimental intensity $I_{exp}(\lambda)$ by the angularly averaged simulated intensity $I^{cav}(\lambda)$, the resulting normalisation for each wavelength gives the intrinsic spectrum $S(\boldsymbol{\lambda})$ [40].

$$\boldsymbol{S(\lambda)} = \frac{\frac{\mathbf{1}}{\boldsymbol{M_\theta}}\sum_{\boldsymbol{m=1}}^{\boldsymbol{M_\theta}} \boldsymbol{I_{exp}}\,(\boldsymbol{\lambda})}{\frac{\mathbf{1}}{\boldsymbol{M_\theta}}\sum_{\boldsymbol{m=1}}^{\boldsymbol{M_\theta}} \boldsymbol{I^{cav}}\,(\boldsymbol{\lambda})} \tag{3.3}$$

The orientation ratio is then extracted by analyzing the TM polarized angular intensity spectrum. To measure the orientation ratio, a stack which emits comparable levels of parallel and perpendicular emission needs to be prepared. The emitter orientation distribution in the devices of this chapter was assumed to be isotropic in the layer interface plane (Section 2.3). However, the ratio of the parallel to the perpendicular emitter TDM components can be ascertained by

separately simulating their angular emission spectrum (Eq.2.3.2), varying the ratio of both and comparing the sum to the experimentally measured emission pattern, following [51]. Mention of parallel emitters/emission in this work should be taken to mean emission from parallel TDM components, and perpendicular emitters/emission to mean emission from perpendicular TDM components. Whether all TDMs have one single orientation with certain parallel and perpendicular components matching this ratio or there is an emitter orientation distribution with the same average orientation involved will result in the same emission pattern as discussed in Section 2.4. Further details about the emitter orientation distribution are not accessible with this type of analysis, only the parallel and perpendicular contributions as a ratio.

The adapted active optical property extraction methods for dual emitter devices will be outlined in Section 5.1

3.4 Fitting & error Analysis

An outline of the errors of all measured experimental quantities and a description of simulation fitting procedures is given in this section.

3.4.1 Passive optical properties

The layer dispersion accuracy reached ($\Delta n \sim 10^{-2}$, $\Delta \kappa \sim 10^{-3}$) is responsible for negligible experimental errors compared to other experimental limitations such as the signal to noise ratio (SNR) as will be discussed in the next section and so is assumed to have a negligible influence on the active optical properties extracted using TE emission only. However, because birefringence of the layer materials is not measured, the simulations of this work assume isotropic material properties. This assumption will affect the orientation properties extracted using TM emission which feature emission from parallel and perpendicular dipoles. With regard to layer thickness errors, uncertainties of ~ 1 nm result from the reflectivity analyses. Only such a difference in the ETL thickness, which acts as the emitter-cathode distance for microcavity interference, has any measurable effect on the simulated angular intensity patterns. However when setting the extracted ETL thickness value at ±1 nm, no active optical property result given in this work is significantly changed.

3.4.2 Angular intensity spectrum

To measure the angular spectrum correctly, the OLED active area centre should be coincident with the goniometer centre of rotation and aligned with the observation optical axis. Alignment was performed by coupling a light source into the fibre where normally the spectrometer detector is coupled. In this way light was backwards propagated through the measurement system compared to the normal OLED light emission and detection setup shown in Fig3.2.2. In this way, the alignment of the OLED active area (pixel) in the $x'$and y' direction could also be performed relatively well (< 0.5 mm). The $\theta = 0°$ angle could be set more accurately than the accuracy of the goniometer (θ< 0.5°). For the measurements of this work, a large z_{det} is chosen so that $\alpha' > \alpha$ and the angular resolution is set by the OLED active area size and not the detection system NA. To obtain a sufficient angular resolution of α<4°, the OLED active area – fibre entrance distance z_{det} was set to 10 cm. The small OLED pixels of radius 0.125 cm (as in section 3.1.3) and large OLED pixels (as in section 3.1.2) of 1.25 cm, had a measurement angular resolution of α=0.7°, and α=3.6°, respectively. These small angular errors had no effect on the experimental pattern measured due to the slow angular variation of the OLED angular spectra and the acceptance angular range of the system (α <4°). However OLED alignment in the z'-direction was more difficult to ascertain and so had a stronger influence on the angular emission spectra measured. To quantify the effect of z'-axis decentring on the emission spectra the emission spectrum was experimentally measured for different z-axis positions around the goniometer centre of rotation.

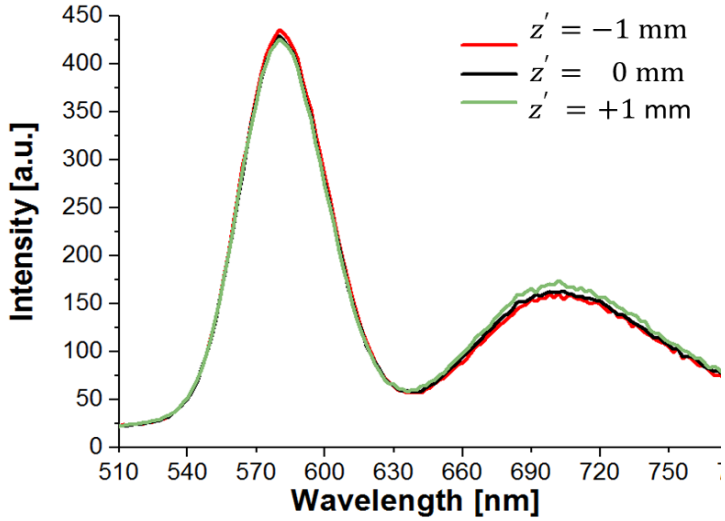

Fig.3.4.1 Intensity spectra with z misalignment. *A misalignment of* $\boldsymbol{z'}$ *= -1 mm is shown in red,* $\boldsymbol{z'}$ *= 0 mm in black and* $\boldsymbol{z'}$ *= +1 mm in green. The effect of higher noise at larger wavelengths can be observed, but there is no definite variation of the intensity error with wavelength.*

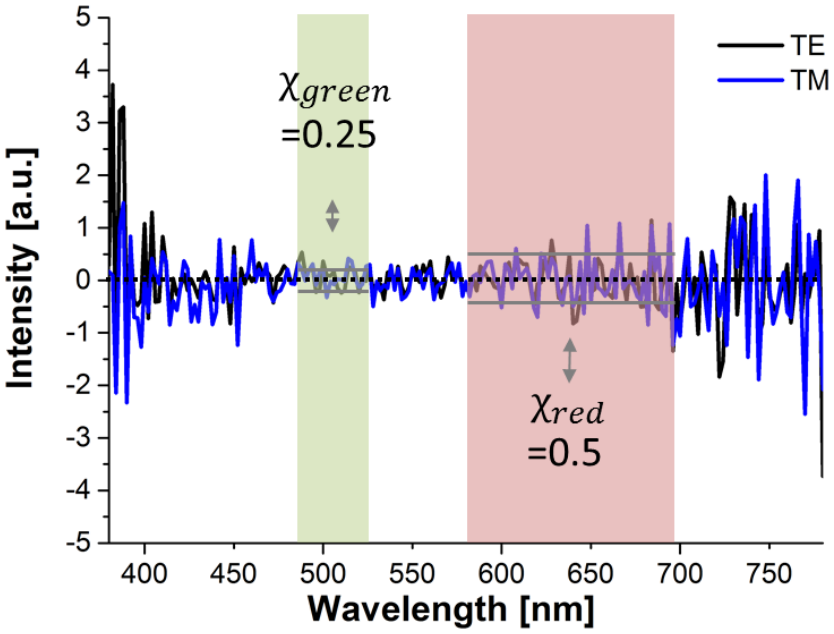

Fig.3.4.2 Noise level at different wavelengths. *The TE (black line) and TM (blue line) intensity are shown with the OLED turned off.* $\boldsymbol{\chi}$ *denotes the noise level at different wavelengths. The green and red columns represent the maximum green and red active optical property extraction wavelength ranges respectively. Grey horizontal lines mark the average noise level for each wavelength band.*

An example θ_A=45° measured experimental spectrum of the device without the interlayer and with d_{sp}=30 nm (Section 3.1.2) is shown in Fig.3.4.1 for best

alignment (z'=0 mm), and misalignments of z'= -1 mm and z'= +1 mm. Observation at θ_A= 45° is shown as it gives a high effect of z' misalignment and also a high emission intensity level. This results in $U(\theta_m)$ the misalignment error of intensity, which had a typical value of ~ 5%.

The noise level of the intensity measured by the spectrometer with the OLED turned off and the laboratory background signal level subtracted is shown in Fig.3.4.2 for a spectrometer integration time of 8000 ms. Average noise levels of χ_{green} =0.25 and χ_{red} =0.5 were measured. The differences result due to the spectral sensitivity of the spectrometer, i.e. it is more sensitive to green light so that a lower lower noise level results.

3.4.3 Fitting procedures

(i) Emission zone profile

The spatial resolution of the EZP in this work are defined using singular value decomposition as described in [42]. Singular value decomposition breaks down the resolution of the detectable EZP into a sum of constant, linear, quadratic, cubic etc. eigenfunctions. It has been calculated using the dynamic range (~280) of the measurement system used in this work that the first three eigenfunctions (EF) of the EZP shape can be resolved. The signal to noise ratio of measurement data is the ratio of the highest measurable value (usually limited by saturation of the detector) and the noise level. The dynamic range in an experiment depends not only on the signal to noise ratio but also on the quantization of the measurement values. Higher dynamic ranges are a result of smaller quantization abilities of the system.

The eigenfunction sum $T(z)$ used in this work to fit the EZP shape is of Legendre polynomial form:

$$\boldsymbol{T(z) = A + B.z + \frac{C}{2}.\left((3z^2) - 1\right)} \qquad \textbf{(3.4.3)}$$

Where *A* is the eigenvalue for the constant term, *B* is the eigenvalue for the linear term and *C* is the eigenvalue for the quadratic term. z is as before the z-axis coordinate, but for this equation real EZP position values are scaled to a range of -1 to 1.

(ii) RMS fitting error of angular spectra fitting

The root-mean squared fitting error of the simulated $I_{sim}$to experimental I_{exp} angular spectrum fit $(RMS_{sim})^2$ is calculated for TE or TM radiation as

$$(\boldsymbol{RMS_{sim}})^2 = \frac{1}{\boldsymbol{M_\theta . M_\lambda}} \sum_{m=1}^{M_\theta} \sum_{n=1}^{M_\lambda} \frac{\left(\boldsymbol{I_{sim}(\theta_m, \lambda_n) - I_{exp}(\theta_m, \lambda_n)}\right)^2}{\frac{1}{\boldsymbol{M_\theta}} \sum_{m=1}^{M_\theta} \boldsymbol{I_{exp}\,(\theta_m, \lambda_n)}} \quad \textbf{(3.4.4)}$$

Where M_θ is the number of discrete angles, M_λ is the number of discrete wavelengths. The intensity difference is divided by a weighting factor of the angularly averaged intensity, to result in a relative error so that the RMS error of different data sets can be compared. The shape of the angular intensity gives the optical property information, not the absolute intensities. A least squares fit is then performed while varying the relevant active optical property parameter.

The fitting error of the experimental data to the experimental data plus the experimental error $\left(RMS_{exp}\right)^2$can be defined as

$$\left(\boldsymbol{RMS_{exp}}\right)^2 = \frac{1}{\boldsymbol{M_\theta . M_\lambda}} \sum_{m=1}^{M_\theta} \sum_{n=1}^{M_\lambda} \frac{\left(\boldsymbol{I_{exp}(\theta_m, \lambda_n)\,.\,U(\theta_m) + \chi(\lambda_n)}\right)^2}{\frac{1}{\boldsymbol{M_\theta}} \sum_{m=1}^{M_\theta} \boldsymbol{I_{exp}\,(\theta_m, \lambda_n)}} \quad \textbf{(3.4.5)}$$

Where $U(\theta_m)$ is the misalignment intensity uncertainty and $\chi(\lambda_n)$ is the noise level.

RMS_{rel} the can then be defined as

$$\boldsymbol{RMS_{rel}} = \frac{(\boldsymbol{RMS_{sim}})^2}{\left(\boldsymbol{RMS_{exp}}\right)^2} \quad \textbf{(3.4.6)}$$

RMS_{rel} can be used to judge whether a fit is a viable solution to the analysis, i.e. if the fit between the simulated and experimental angular spectrum has an RMS_{sim} error less than or equal to the experimental error ($RMS_{rel} \leq 1$).

4. RESULTS & DISCUSSION: SINGLE RED EMITTER DEVICES

In this chapter the extracted active optical properties of single red emitter OLEDs will be analysed and discussed. Firstly in Section 4.1, the EZP will be extracted in the established way but with an adapted assumption allowing for emission from outside of the EML. The intrinsic spectrum of such a device is analysed in section 4.2. In Section 4.3 the orientation ratio will be extracted in the established way, but again allowing for emission from outside of the EML. In section 4.4, a new specialised type of device featuring a thin metal interlayer close to the emitters is introduced. The dispersion of this interlayer was analysed and the EL and PL intrinsic quantum efficiencies of this device without and with the interlayer at various positions are extracted. In Section 4.5 the results of a novel method to investigate the emitter orientation distribution (EOD) in more detail using such an interlayer device is outlined.

4.1 Emission zone profile

Device A (described in Section 3.1.2) without the inter-layer and with a HTL spacer thickness of 30 nm was used to extract the EZP. Only TE polarized emission was considered in this section, so that the effect of the EOD ratio, material birefringence are insignificant. An electron transport layer (ETL) thickness of 160 nm has been selected to yield a microcavity interference emission minimum in the emission spectra. Emission around this minimum is sensitive to the EZP and can be seen running diagonally through Fig.4.1.2.3(a) and Fig.4.1.2.3(b). The fitting range used was always λ =600 nm…700 nm to make use of all high SNR interference minimum data which is most sensitive to the EZP. The experimental noise level for this wavelength range is 0.5 (Section 3.4.3).

4.1.1 EZP confined to EML

In the first part of the analysis it was assumed that emission was only from the EML (for devices in this chapter, 10 nm wide), as is normally assumed in analysis of OLEDs with blocking layers [32, 41]. Fundamental EZPs can be seen in Fig. 4.1.1.1(a), and in (b) their corresponding simulated emission patterns (where the pattern refers to the angular variation of intensity) along with the experimentally measured pattern TE for λ =650 nm, an example wavelength which shows the most of the interference minimum. In Fig. 4.1.1.1(a) and Fig. 4.1.2.1.(a) the EZP

was modelled as 11 discrete points 1 nm apart and 31 discrete points 1 nm apart, respectively. RMS_{rel} has been in Section 3.4.3 introduced as the RMS error of the simulation-to-experimental least squares fit relative to the experimental error. RMS_{rel} values given are always calculated for the complete wavelength fitting range of λ =600 nm … 700 nm, and not just the single example wavelength shown. An EZP is a viable solution to the analysis if the fit between the simulated and experimental angular spectrum has an RMS_{rel} error less than or equal to the experimental error ($RMS_{rel} \leq 1$).

Firstly, a constant EZP (short red lines across the full 10nm in Fig.4.1.1.1(a)) was set. The spectra in Fig.4.1.1.1(b) fit badly with RMS_{rel}=12.3.

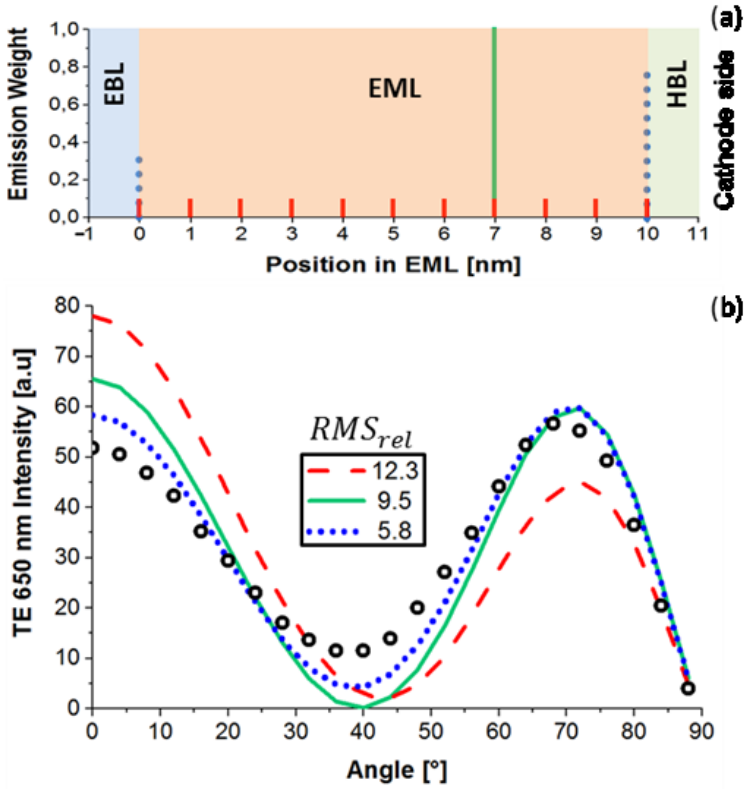

Figure 4.1.1.1 Angular spectrum fitting assuming different confined EZPs. *(a) Shows the fundamental EZPs. The red lines show a constant EZP, the green line the best fitting single point and the blue dotted line the best fitting point-by-point fit and. (b) Shows the resulting simulated angular intensity patterns using these EZPs and the experimental data (black circles) for 650nm TE emission.*

Three fundamental fitting problems were identified: (i) The 0° simulated intensity was too high (ii) The simulated interference minimum intensity at ~40° was too low. (iii) The simulated 70° intensity was too low. A hypothetical single emission

point (highest green solid line) was set to concentrate emission towards the cathode side to improve (i) and (iii) simultaneously. The spectra show an improved but unacceptable RMS_{rel}=9.5. Such shifting within the 10 nm wide EML cannot significantly improve (ii). It is known that the EZP width is directly proportional to the height of the angular emission pattern interference minimum [113]. So, the blue dotted EZP was set at the 0nm and 10nm extremities (again more cathode-sided to satisfy (i) and (iii)). However, the simulated interference minimum intensity still does not near the experimental. The simulated TE angular emission spectrum for this EZP can also be observed over all fitting wavelengths in Fig.4.1.2.3(a).

A singular value decomposition analysis gives the most complex resolvable functional EZP shape as a sum of constant, linear, quadratic, cubic etc. eigenfunctions. The resolvable eigenfunctions have been calculated as described in Section 3.4.3 using the dynamic range (~280, Section 3.4.3) of the measurements that the first three eigenfunctions (EF) of the EZP shape can be resolved. So the spatial resolution was limited to the sum of a constant, linear and quadratic function. Higher order EZP functions cannot be resolved due to the limited dynamic range of the measurements.

Several possible experimental errors which may have caused a higher simulation contrast have been investigated in order to exclude them: (i) Noise in the spectra, which may falsely increase the minimum intensity, can be ruled out as a cause due to the low measured noise intensity level of 1 for the measurements of Fig. 4.1.1.1(b). Further experimental data as that shown in Fig.4.1.1.1 (b) but with an increased integration time were taken resulting in an intensity ratio at the interference minimum at 40° of experimental:simulation:noise = 50:25:1. Therefore the contrast mismatch is not caused by measurement noise. The simulation used the best fitting blue-dotted EZP of Fig.4.1.1.1 (ii) Scattering inside the spectrometer, which could cause a reduction of contrast in the spectra, was ruled out by detecting an appropriately narrow emission spectrum of the green laser diode (Section 3.2.2). (iii) The possible presence of significant internal scattering inside the OLED itself, which would require a more sophisticated emission model, was investigated by an angularly resolved scattering investigation [114]. It revealed an angularly resolved scattering in the range of $10^{-4}\,sr^{-1}$, which yields negligible intensities compared to those measured at the minimum of the

angular emission. (iv) The effect of positional and angular OLED misalignment on the emission spectrum was measured (Section 3.4.2) and also ruled out as a cause of this contrast mismatch. In conclusion, as no possible EML-constrained EZP results in a fit to the experimental data within the experimental error, so one or more of the simulation assumptions must be wrong. The interference minimum fitting problem suggests a wider EZP than first assumed. Therefore, in the proceeding section, the allowed EZP width was increased to also allow for emission from the surrounding blocking layers.

4.1.2 EZP Extended into blocking layers

In such a multi emission-layer analysis, separate emission simulations for each layer are summed to be compared with the experimental emission pattern. Since only one intrinsic spectrum can be extracted from the combined emission of all active layers, a total emission effective intrinsic spectrum was actually used for each layer, and not the individual spectrum for each layer. The intrinsic spectrum of the emitter should be different in the α-NPD host layers (EBL and EML) than in the different material HBL layer. It was assumed here that this change was small enough as to not affect the EZPs extracted. With regard to resolution, since a 30 nm EZP is wider, constant, linear and quadratic function components can still be resolved, but there is still not yet a high enough dynamic range to resolve cubic-shaped functions.

Shown in Fig. 4.1.2.1(a) are all the qualitatively different types of EZP solutions found in the analysis, where their simulated spectrum in Fig. 4.1.2.1(b) fits the experimental spectrum with RMS_{rel} ~1. The extended EZP gives a much better fit to the interference minimum of the experimental angular spectrum as can be well observed in Fig.4.1.2.3. Lines in Fig. 4.1.2.1(a) are only for visualization purposes, the EZP was modelled as before by discrete points. The different solutions arise from different emission combinations of the three layers. Point-by-point fits were first performed (not shown) to show all possible solutions, then more physically expected Gaussian and exponential functions were used to model these solutions.

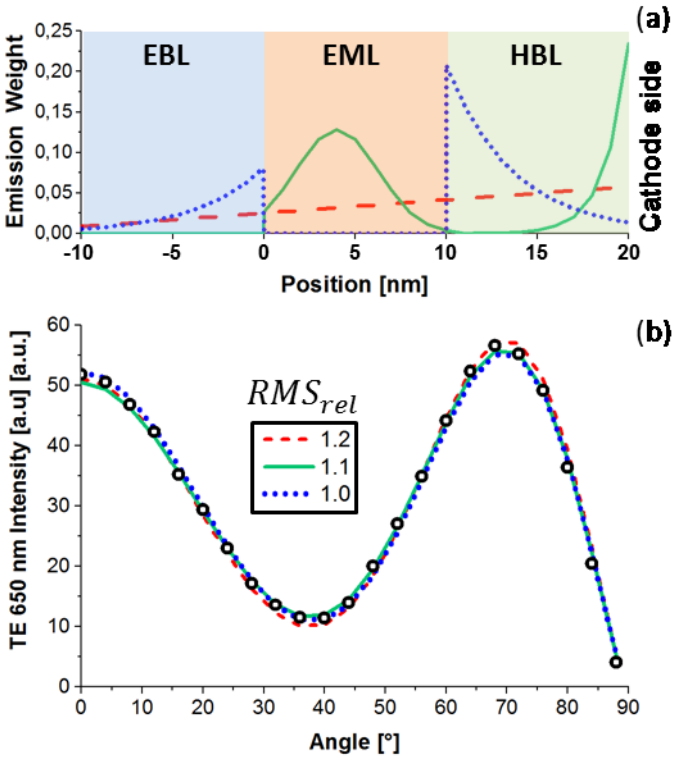

Figure 4.1.2.1 Angular spectrum fitting assuming multiple layer emission. *In part (a) the red line shows an EF sum solution, the blue dotted line shows two exponential decays in the EBL and HBL and the green solid line shows a Gaussian in the EML and an exponential in the HBL. (b) Shows the resulting simulated angular intensity patterns using these EZPs and the experimental data (black circles) for 650 nm TE emission.*

The red linear EZP has emission from all 3 layers and results from a best fit of the function parameters of an EF sum. Thus, as mentioned before, this solution is within the measurement resolution. Of course, EZPs with stronger spatial modulations are possible, such as sum of gaussians and exponentials, the spatial average of which corresponds to the fitted EF-shape according to the noise limited resolution. The blue dotted EZP is composed of an exponential in the EBL and in the HBL. The green solid line EZP is composed of a Gaussian in the EML and an exponential in the HBL. Since these former two solutions show higher spatial variation than the resolution allows, they are indistinguishable compared the EF solution. Whereas it can be stated that the red dashed extended EZP is a better fit to the experimental data than all confined EZPs, it cannot be concluded that the green solid and/or the blue dotted extended EZPs are a better fit than the red

dashed extended EZP. No EBL and EML combined emission solution with comparably low error can be found.

The effect of Förster transfer on device emission can be estimated by simulating the emitter lifetime (Section 2.4) with position in the device. The lifetime of parallel and perpendicular oriented emitters is plotted both in the EML and for positions in the blocking layers in Fig.4.1.2.2. Förster transfer from the emitters to the ETL can be observed. For emission from the EML, the 10 nm thick blocking layers (which are selected to have negligible visible spectrum absorption) ensure negligible Förster transfer. However, emitters in the HBL approaching the Förster radius of a few nanometres results in a rapid lifetime decrease.

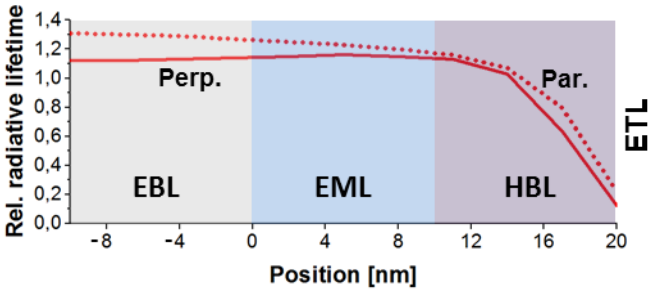

Fig.4.1.2.2 Förster transfer from emitters to the ETL. *Parallel and perpendicular oriented emitter lifetimes are simulated for positions in the EML and the blocking layers. A quantum efficiency of q=0.3 (value from measurement of Section 4.4.2) and a wavelength of λ =640 nm is used. The EML dispersion is assumed for all layers, this should not affect the lifetimes significantly.*

Lifetime changes due to Förster transfer from the emitters to neighbouring layers are possible where the layer absorbs in the emitter intrinsic spectrum. The simulated lifetime of parallel and perpendicular orientated emitters are slightly different because of different microcavity interference conditions for each emitter (Section 2.3). Devices with an extended EZP can in this way have a reduced intrinsic quantum efficiency.

The fit for the complete angular spectrum using the best fitting cathode-preferred both-extremities EZP – the blue lines in Fig. 4.1.1.1(a), is shown in Fig.4.1.2.3. A contrast difference between the simulated and experimental patterns at the interference minimum (λ~620 nm, θ_A~50°) can be observed.

Since the effective intrinsic spectrum of the emitting molecules extracted matches the one determined by photoluminescence very well (Section 4.3), it

seems likely that emission is not from the blocking layer materials but from $Ir(MDQ)_2acac$. So the evidence of emission from the blocking layers points to diffusion of emitters into the blocking layers. Small molecule emitter diffusion over such distances into adjoining layers for controlled doping of OLED active layers [39, 115] has been reported in the literature. However, these devices were heated at 100° C and 80° C respectively, unlike in this work. Perhaps with the devices of this work, device operation over time has a similar diffusion effect as this heating.

Additionally, an abnormally low EL q =0.30 at the same current density as the patterns measured here, but an expected PL q =0.83 has been measured for this device as outlined in Section 4.4. The low EL q might be attributed to an extended EZP as discussed in Section 4.4. The normalized angular spectra and therefore the EZPs at 1 mA/cm^2 and 20 mA/cm^2 show no differences.

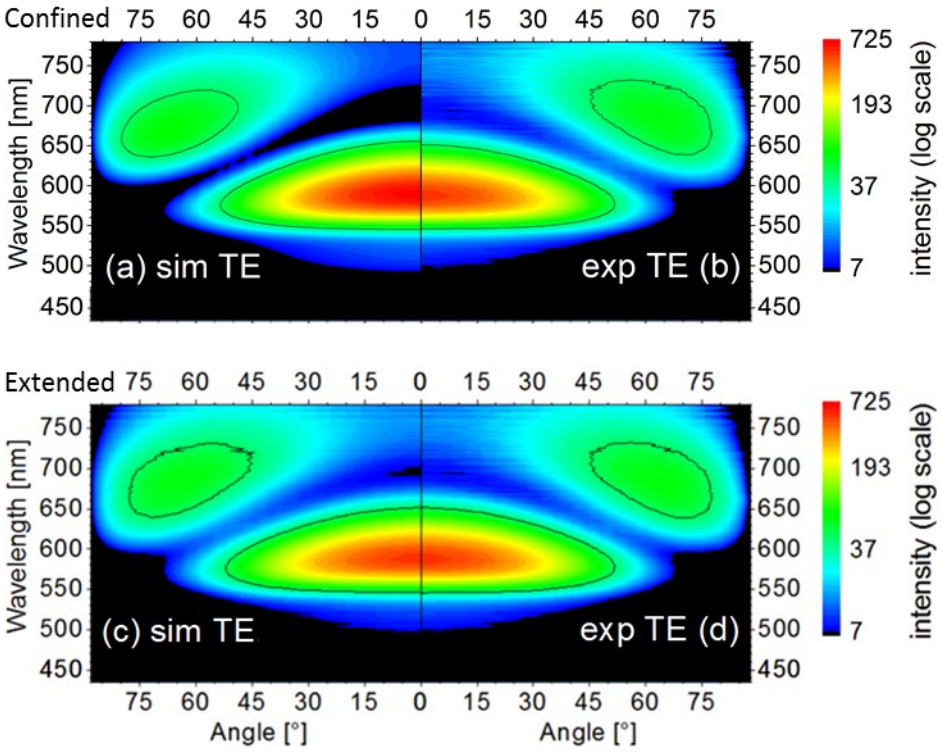

Figure 4.1.2.3 Confined and extended EZP angular spectra comparison. *The interference minima in the confined EZP simulated angular spectrum (a) is too low compared to the experimental data. The experimental spectrum is shown for comparison twice in (b) and (d). In the extended EZP simulated angular spectrum (c) a better interference minimum (centred at around λ ~620 nm and* $\boldsymbol{\theta_A}$*~45°) fit results. The black contour line shows an intensity value of 50 as a viewing aid. All diagrams have the same intensity scale.*

The red dashed EZP of Fig. 4.1.2.1(a) could be explained by charge recombination and triplet exciton formation in the EML, followed by triplet diffusion (triplets were found to diffuse 11 ± 3 nm for an $Ir(MDQ)_2acac$ in 4P-NPD host OLED [19]) across the blocking layers, where they can reach the similarly diffused emitters and emit. The triplet levels of α-NPD and the HBL are sufficiently higher (Section 3.1.2) than the emitter so that negligible triplet transfer to non-emitter molecules should occur. The blue dotted EZP could be explained in a similar way, but perhaps with large triplet polaron quenching in the EML, caused by either a high buildup of electrons to the cathode side of the EML due to poor emitter electron transport. The green solid line EZP could be explained by even poorer emitter electron transport and increased emitter diffusion further into the HBL, causing a charge buildup and TPQ further towards the cathode.

Further experiments to investigate whether emitters are present in the blocking layers need to be performed to prove the hypothesis presented here. The simplest test would be to, during the manufacturing phase, codope the emitter in the blocking layers as well as the EML and analyze the output to check if a similar EZP extraction results as in this work. Analogously, emitters could be deposited in a very thin layer of ~2 nm and the EZP extracted. Changes with time should be monitored or an ageing analysis should be performed. Diffusion barriers or thin quenching or sensing layers could be incorporated in the device, but these layers could alter the device charge transport.

To confirm or rule out the other higher spatial frequency solutions, through improvement of the resolution of the EZP extracted, it has been calculated that measurements using a 5 % transmission filter could show the EZP 3rd order cubic EF. The lower intensity part of the wavelength spectrum can be measured without the filter, and the higher part with the filter, then the lower part intensity values can be scaled up with knowledge of the filter transmission behavior. This filter increases the dynamic range by a factor of 20, but one also additionally needs one order of magnitude increased dynamic range of the detector.

In conclusion, no EML-confined EZP can be found in this analysis. The evidence points to an extended EZP, probably due to emitters having diffused into the blocking layer(s).

4.2 Emitter ensemble intrinsic emission spectrum

It is helpful in this work to think of the emitters' intrinsic spectrum as a weight function of emission for different wavelengths. Once the EZP is known, it can be normalised in the simulation to an area of 1. The resulting normalisation for each wavelength by dividing the angularly averaged experimental intensity by the angularly averaged simulated intensity is the emitters' intrinsic spectrum (Section 3.3). However even with the non-optimised devices which are sensitive to, and so are used to extract the EZP, there was no difference (within the noise level) in the intrinsic spectra extracted using any of the different EZP solutions presented for this device in Chapter 4.1. The extracted EL intrinsic spectrum is compared with PL spectra of single layers of the same emitting system with different emitter dopant concentrations in Fig.4.2.1. All emission systems are $Ir(MDQ)_2acac$ emitter in α-NPD host. PL measurements were supplied by Osram Regensburg and were carried out on thin thermally evaporated single films.

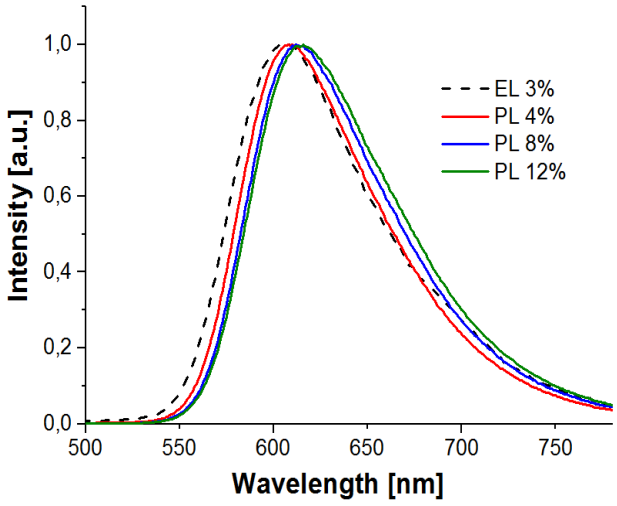

Figure 4.2.1 Intrinsic spectra measurements. *The intrinsic EL spectrum extracted from non-inter-layer device A with 30 nm HTL spacer is shown alongside PL spectra of single layers of the same emitting system with different emitter dopant concentrations.*

The wavelength redshift with increasing emitter concentration can be noted, as described for $Ir(ppy)_3$ and $Btp_2Ir(acac)$ emitters due to self-quenching interactions

at increased dopant concentrations [116]. A device of 160 nm ETL was used to extract the internal spectrum, so it is sensitive to the EZP, and the three-layer extended EZP of Fig.4.1.2.1 was used in the simulation. The unstructured line shape of the extracted spectrum agrees with that expected from $_3$MLCT emission [117].

4.3 Emitter ensemble orientation ratio

Non-inter-layer devices which have been designed for orientation analysis (Section 3.3) are analysed in this section. Results here are presented (Fig.4.3.1) for the device with 30 nm HTL spacer and the simulation uses the 3-layer extended EZP result from Section 4.1.2. For all the extended EZP results shown in Fig.4.1.2.1(a), a more perpendicular best fitting orientation ratio of ∥:⊥ =2:0.75 with RMS_{rel} = 1.7 results. The most likely reason that the fit cannot reach the experimental error value would be that birefringence of the stack layers was not accounted for. This affects the orientation ratio extracted as emission from parallel and perpendicular emitters experience different dispersions.

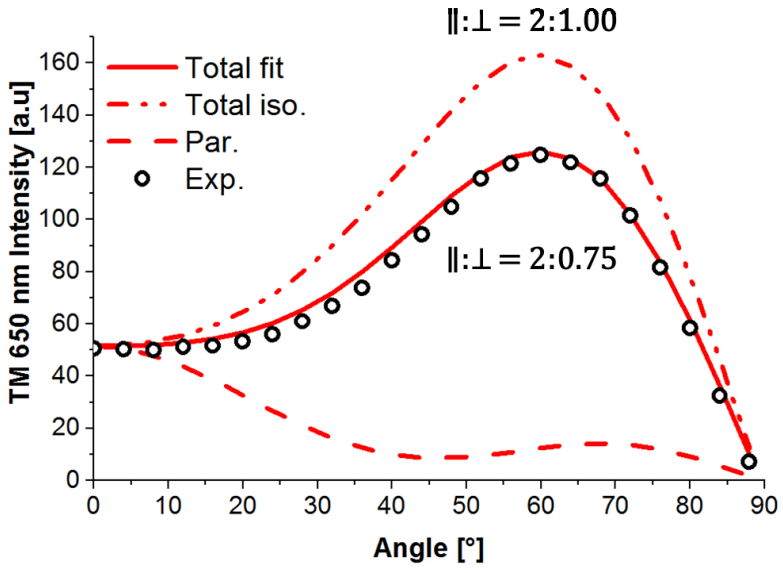

Figure 4.3.1 Orientation ratio fitting with an extended EZP. *TM emission for an illustrative wavelength of λ=650 nm with an extended EZP (the red dashed line in Fig.4.2.2.1(a) is shown. The total TM emission for the fitted orientation ratio is shown as the solid red line. The total isotropic TM emission is shown as the dashdot red line. The emission contribution of parallel emitters is shown as the red dashed line. Experimental data points are shown as black circles.*

A comparison of the simulated (with an extended EZP and ||:⊥=2:0.75) and experimental TM emission spectra is shown in Fig.4.3.2.

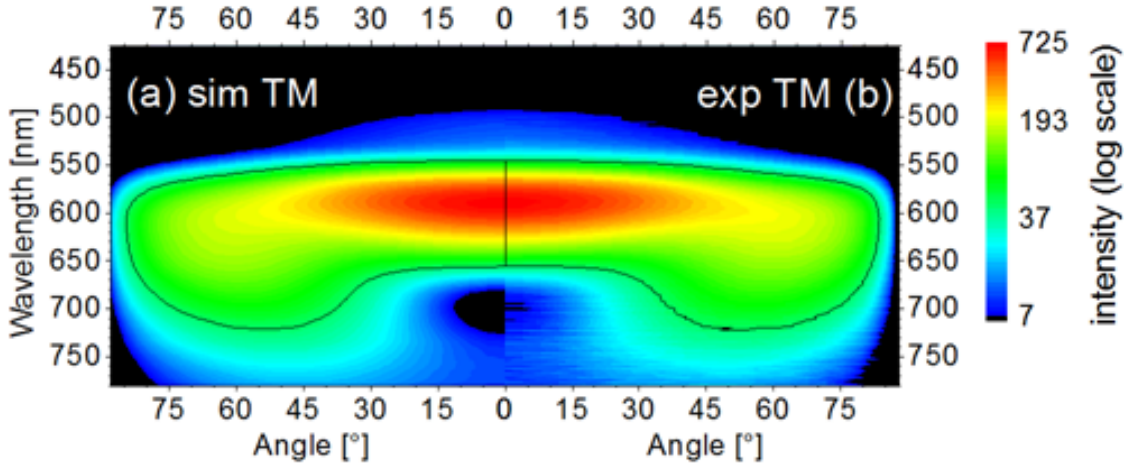

Figure 4.3.2 TM angular spectra fitting comparison. *The device measured here is a non-inter-layer device A with 30nm HTL spacer. The simulated TM spectrum (a) for an extended EZP with ||:⊥=2:0.75 and the experimental spectrum (b) are shown. The black contour line represents a value of 50.*

For the lowest-error confined EZP simulation an orientation ratio of ||:⊥=2:0.69 with a TM spectrum fitting error of RMS_{rel} =4.9 results. The RMS_{rel} doubles at orientation ratios of 2:0.61 and 2:0.77. The parallel and perpendicular radiative lifetimes change differently with distance from the cathode in an extended EZP, but at an intrinsic EL quantum efficiency of 0.30, as measured in Section 4.4, a difference in the emission lifetime (derived from the radiative and non-radiative lifetimes, see Section 2.4) should be unresolvable. The EML position in the device stack was originally optimized to result in high emission from perpendicular emitters (and low parallel emission) via the microcavity modulation (Section 3.3). The further the emitters are from this point, the less their simulated perpendicular emission is (and the higher the parallel emission is). In this analysis the experimental TM emission pattern was modelled by the simulated perpendicular emission intensity spectrum multiplied by the amount of perpendicular emitters. So if the simulated perpendicular emitter intensity spectrum decreases, the perpendicular emitter contribution must increase. Where the simulated parallel emitter intensity spectrum also increases, the perpendicular emitter contribution will increase even more.

Perhaps different orientation ratios in the EBL and EML than in the HBL of different material is a reason that the experimental error was not reached. However, even allowing this degree of freedom, an RMS_{rel} of 1.42 resulted. To get an idea of the range of orientation ratios close to the local minimum of the fit, a 50% increase to the best RMS_{rel} results in an orientation ratio range of ||:⊥ =2:0.69…2:0.81. Both this extended EZP orientation ratio result and the confined EZP agree well with previous results indicating a more parallel aligned emitter ensemble for this emitter of 2:0.65 in the same host as this work [47] and 2:0.72 in an NPB host [52].

In conclusion, the orientation ratio extracted agrees with previously published results. A significant increase in error and a change in the orientation ratio was observed when comparing extended and confined EZPs. Every orientation ratio measured in the literature thus far assumes EML confined emission. Investigating a possible extended EZP should be performed in all orientation ratio extraction processes.

4.4 Intrinsic quantum efficiency of interlayer devices

In this section emission lifetimes are measured for devices A with, and devices B without an inter-layer and with varying HTL spacer thicknesses (*d*). First, in Section 4.4.1, the dispersion of this thin metal interlayer was analysed to check if bulk material dispersions applied well to its optical behaviour. In Section 4.4.2, intrinsic quantum efficiencies are then extracted for EL and PL operation. The plasmon mediated radiative lifetime difference between parallel and perpendicular emitters caused by the inter-layer in the HTL depends on the radiative rate and therefore the intrinsic quantum efficiency *q* of the devices. For a large difference, a high *q* is needed. Since emitter radiative and emission lifetimes will be affected depending on proximity to the inter-layer by having several different emitter- inter-layer separations, the device *q* can be extracted [58, 59]. The emitter- inter-layer separations in this case are controlled by different HTL spacer thicknesses. It is to be noted that it was assumed here that device electrical behavior which could affect device *q* does not significantly change with the different HTL spacer thicknesses.

4.4.1 Thin Ag:Ge interlayer optical properties

Half of the single red emitter devices feature a 12 nm inter-layer composed of ~1 nm Ge and the remainder from Ag (Devices B), as detailed in Section 3.1.2. The thin Ge layer acts as a nucleation / wetting layer which reduces the surface roughness of the deposited Ag layer by up to an order of magnitude [118, 119]. Firstly, for devices (Devices A) without the inter-layer, the measured device reflectivity after each layer deposition was compared with simulated data using layer dispersions measured as described in Section 3.1.4. and using Ag and Ge dispersion data for bulk samples as outlined by Palik [109] for the cathode. Layer thicknesses were successfully extracted from the fitting process and agreed well with those specified by the manufacturer. Secondly, devices *with* the inter-layer were analysed. Directly after the inter-layer deposition step, the fitting became very unsatisfactory, indicating that the dispersion model of the inter-layer was not accurate enough. The effect on the complete stack fitting can be seen for a device with a 30 nm HTL spacer layer in Fig. 4.4.1.1(a).

Palik data corresponds to bulk layer behaviour but the layers of this work are on the tens of nm scale. Maroof et al. reported that effective refractive indices were needed to model Ag nanolayers due to nanoisland and void formation [120]. They derived an altered permittivity featuring an increased real part of refractive index for a 10nm film in the visible range compared to the bulk case while having a very similar imaginary coefficient behaviour for both the 10nm and bulk film cases. Zhao et al. [121] and Gong et al. [122] reported refractive index results qualitatively in agreement. Following the models of these publications the Ag permittivity here was modified, as shown in Fig.4.4.1.2, to better simulate the experimental reflectivity data, the fitting of which is shown for the 30 nm HTL spacer device in Fig. 4.4.1.1(b). Reflectivity fitting of devices with a 10 nm or 75 nm HTL spacer fit well also (not shown). In this way a modified refractive index of the inter-layer was used in the simulations for the rest of the sections in this chapter. In conclusion, Ag films of thickness of the order of 10 nm cannot be well described by the bulk Palik dispersion. The dispersion needs to be adapted for nanofilm properties.

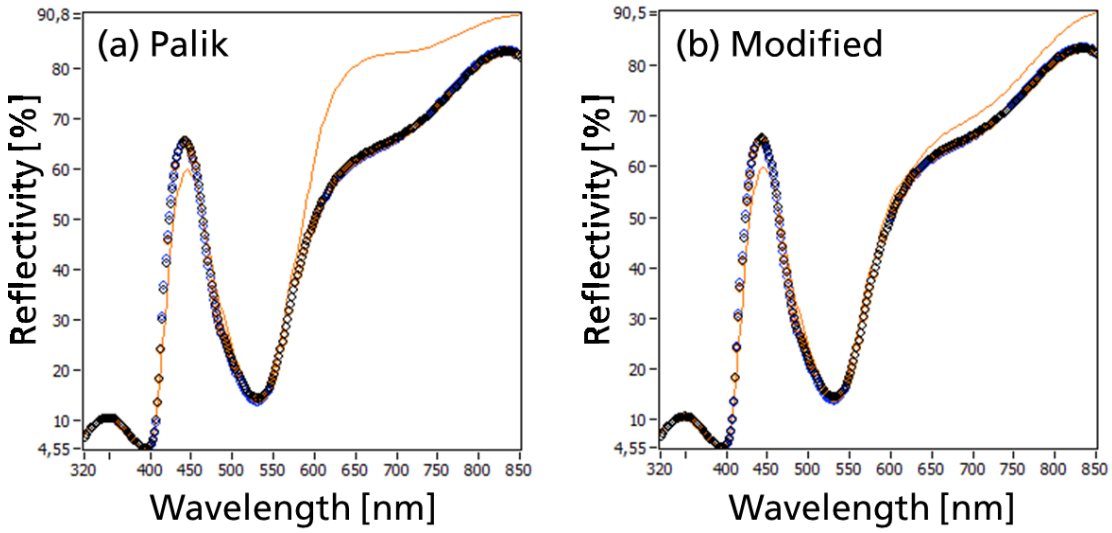

Figure 4.4.1.1 Complete inter-layer device reflectivity fitting. *(a) Shows the complete 30 nm HTL spacer device experimental reflectivity and a simulation using Palik bulk Ag and Ge data. Circles represent two sets of experimental data and the solid line is the simulation. (b) Shows the fitting performed with the modified Ag refractive index.*

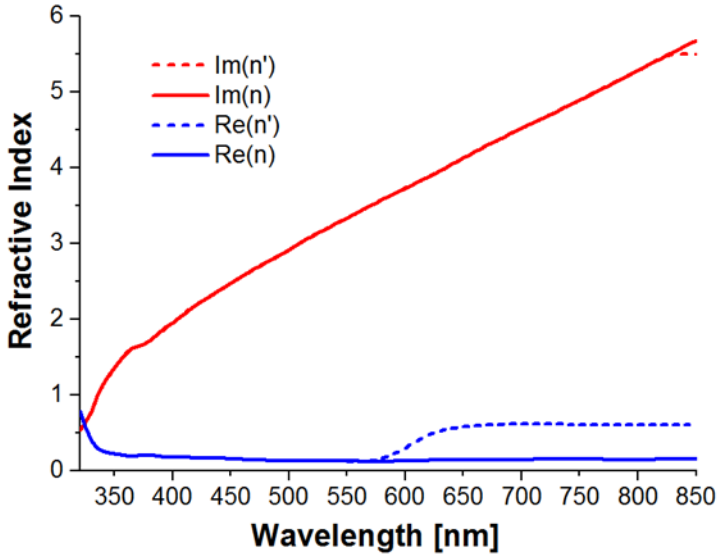

Figure 4.4.1.2. Refractive index modification. *Palik data is shown as solid lines and modified data as dashed lines. Red lines show the imaginary part and blue lines the real part of the refractive index.*

In conclusion, an adapted dispersion other than the bulk Palik data.needs ot be used to better simulate thin (~10 nm) Ag film optical properties.

4.4.2 EL and PL intrinsic quantum efficiency

In Fig.4.4.2.1 the effect of HTL spacer thickness d_{sp}, i.e. the emitter-inter-layer distance on emission lifetimes can be seen. The simulations are performed for a single central emitter position. A stack without the inter- layer features emission rates that are almost independent of emitter orientation (black lines with y-axis values around 1.0).

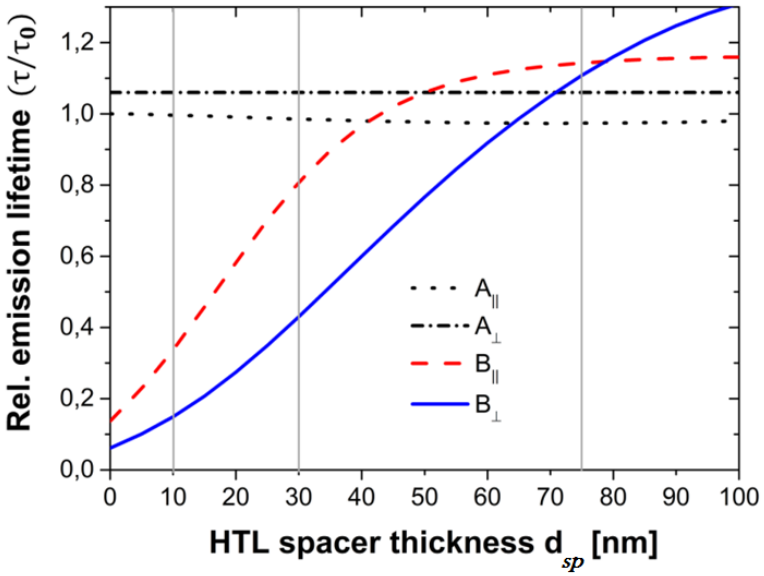

Figure 4.4.2.1 Variation of emitter emission lifetimes with HTL spacer layer thickness. *Non- inter-layer devices A and inter-layer devices B with HTL spacer thickness d in the OLED stack is plotted assuming ideal (q=1) parallel or perpendicular emitters. Grey vertical lines indicate the devices analyzed in this work.*

Referring to the device outline of Section 3.1.2, Fig.4.4.2.1 illustrates that the relative emission lifetime is nearly independent of emitter orientation for all devices A and for devices B with d=75 nm, whilst the other devices B with 10 nm and 30 nm thick HTL spacer layers should introduce significant emission lifetime splitting of up to a factor of two.

Transient EL and PL experiments (Section 3.2) have been performed with all devices and with different observation conditions, i.e., varying angles and polarizations of the measurement. When observing at such different conditions no emission lifetime variation was found within the experimental error that was estimated from repeated experiments and the temporal resolution of the measurement system to be $\Delta\tau < \pm$ 0.02 µs. They are thus shown as one data point in Fig.4.4.2.2

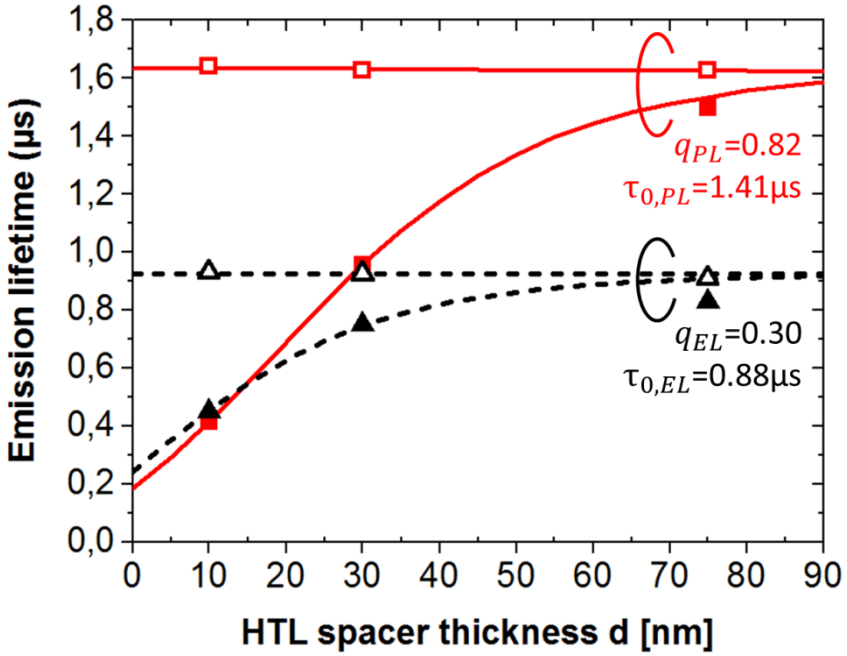

Figure 4.4.2.2 Intrinsic quantum efficiency from emission lifetime measurements. *PL (squares) and EL (triangles) experiments with Devices A (empty symbols) and B (filled symbols) and plotted vs. HTL spacer layer thickness d. The simulated curves illustrate the best fit for PL (red solid line) and EL (dashed black) lifetimes. Symbol size is set to illustrate experimental errors of* $\Delta d < \pm 2$ *nm and* $\Delta\tau < \pm 0.02$ *µs.*

All transient data could be well fitted by single exponential decays. Both types of devices follow a behavior somewhere between the parallel and perpendicular emitter curves shown in Fig.4.4.2.1. The reasons for these observations will be discussed in Section 4.5. Using the measured extended EZP orientation ratio of Section 4.3, and the measured EL and PL emission lifetimes for the different devices, the intrinsic quantum efficiency q and the emission lifetime in the infinite homogeneous medium $\tau_0 = 1/\Gamma_0$, are extracted by fitting the data with Eq.2.4.7, which can be seen as the simulated lines in Fig.4.4.2.2. These simulations assumed an extended EZP, in that the simulation results at three emitter positions (the center of each blocking layer and the EML centre) were averaged together. For EL experiments q_{EL}=0.30 and $\tau_{0,EL}$=0.88 µs are obtained, whilst q_{PL}=0.82 and $\tau_{0,PL}$ = 1.41 µs are derived for PL excitation, which is close to previous reports of $\tau_{0,PL}$ = 1.37 µs and q_{PL}=70% for the same material system but with 8% emitter concentration [58, 123, 124].

With the least-error confined EZP which resulted from Section 4.1.1, the extracted orientation ratio changes and a confined EZP would result in a weaker lifetime dependence with position in the stack as described in Section 4.1.2. From these two effects, values for the EL intrinsic quantum efficiency and decay time in infinite homogenous medium would change from to 0.30 to 0.19 and to 0.88 μs 0.83 μs respectively. Values for the PL intrinsic quantum efficiency and decay time in infinite homogenous medium would change only slightly from 0.82 to 0.83 and to 1.41 μs to 1.37 μs respectively. The fitted curves match the experimental emission lifetimes almost perfectly. As predicted by Fig.4.4.2.1, a minimal effect of HTL spacer thickness on the emission lifetime is apparent for devices A, whilst devices B feature a pronounced emission lifetime decrease with decreasing HTL spacer thickness *d*. The amplitude of this plasmon induced loss was much larger for the PL compared to the EL case, as expected from their respective *q* values.

The results obtained for the EL emission lifetimes and the intrinsic quantum efficiency are quite low. An EL experiment performed as a cross check by a University of Augsburg research group [125] has confirmed the low EL emission lifetime result reported here. Such a low value reduces the orientation dependent radiative lifetime differences, thus reducing the desired difference in the emission lifetimes below the experimental accuracy to be used in Section 4.5. For this reason PL measurements were also performed. An EL intrinsic quantum efficiency of 0.84 has been reported at 1.5 mA/cm^2 for the same emitting molecule in a different host material [126]. Apart from the different host (if the host was the cause then the PL q should also be low), the differences in this dissertation work are (i) higher current density (ii) device inter-layer, (iii) lower emitter concentration of 3% and (iv) most likely a much larger device active area.

Each difference will now be considered as a cause of the low EL q;

(i) The higher current density (50 mA/cm^2) of this work could cause the reduced EL q. The preferably aligned emitter molecules of the present work have been shown to exhibit pronounced roll-off at emitter–cathode separations that are well suited for orientation analysis [26]. This matches the device designs used in the present study. In this work, with a current density of 1 mA/cm^2 an increased q of ~ 0.50 results (the emission lifetime error at these low signal levels was too high to result

in measurable parallel to perpendicular emitter emission lifetime differences). So the efficiency roll-off at larger current densities [127], as described before for the emitter under study but at 8% doping concentration [26, 27, 123] partially causes the low EL intrinsic quantum efficiency, but cannot fully explain it.

(ii) With regard to the devices A without the inter-layer, the simulated curve is in good agreement with the experimental values in Fig.4.4.2.2. Therefore the low emission lifetime observed in EL operation is not governed solely by the additional inter-layer but also apparent in the devices A. Impurities, which could be connected to the deposition of the inter-layer, would also decrease the PL performance and thus can be excluded.

(iii) A lower emitter doping concentration normally increases the q due to impeding concentration quenching. However in cases where electric field quenching by disassociation of excitons is significant, lower doping concentrations lead to higher field induced quenching [128, 129]. The reason is that excitons on lower band gap (further in energy from HOMO and LUMO) dopants have higher energy barriers to dissociate. So less doping concentration leads to a higher fraction of excitons formed on host molecules (although the emitting system in the reference is different than here), which the electric field can easier dissociate.

PL emission lifetimes point to an electrical or a different EL and PL EZP cause. The unexpected extended EZP result from Section 4.1.2 could be much different to the PL EZP, and so could cause increased EL losses. In conclusion, it is not clear why such a low EL q is measured. The emitter doping concentration has been changed because of large active area, designed to decrease short circuits in the devices with the thin metal interlayer. Electric field quenching of excitons or a different EL and PL EZP were presented as most probable causes.

4.5 Emitter ensemble orientation distribution

Devices A were prepared without, and Devices B with a inter-layer (See Fig. 4.5.1.1) to investigate the angular width of the emitter ensemble orientation distribution (EOD) in state of the art red OLED devices.

4.5.1 Emission lifetime analysis of interlayer devices

In this section, orientation results from angular emission intensity spectra analysis (Section 4.4) were combined with the separate observation of parallel and perpendicular emitters in a device with orientation dependent radiative and thus emission lifetime changes. In this way, the extraction of angular EOD details may be possible, provided other conditions to be seen are met. Devices with adapted ETL thicknesses (Section 3.3) give one the choice to observe either mostly parallel or mostly perpendicular emitters in the substrate using an index matched half ball lens, or in air, by polarisation and angle dependent observation (Fig.4.5.1.1(a)). It is known from Section 4.4.2 that a strong orientation dependent emission lifetime splitting of up to a factor of two due to interaction with the inter-layer is induced in the case of Device B and that the relative emission lifetime is nearly independent of the EOD for Device A. The different orientation averaging cases (b,c,d) and their transient decay behaviours for the ensemble, parallel and perpendicular emitter observation are sketched in the transient luminescence decay graphs (e,f,g) on the right of Fig.4.5.1.1.

The detailed temporal behaviour depends on the EOD combined with a weighting function that considers the contribution of each emitter TDM to the experimental result. In the wide angular EOD (90°) case, parallel emitter observation would result in a mostly parallel emitter emission lifetime (oblique emitters have a mixed emission lifetime), which is not plasmonically damped by the inter-layer. Perpendicular emitter observation would result in a mostly perpendicular emitter emission lifetime, which would be shorter, due to the plasmonic losses. However, if the angular width of the EOD is 1° (or in fact up to 17°, as will be shown), for the near single orientation assumption, the parallel and perpendicular emitter emission lifetimes would be indistinguishable within the range of the experimental error.

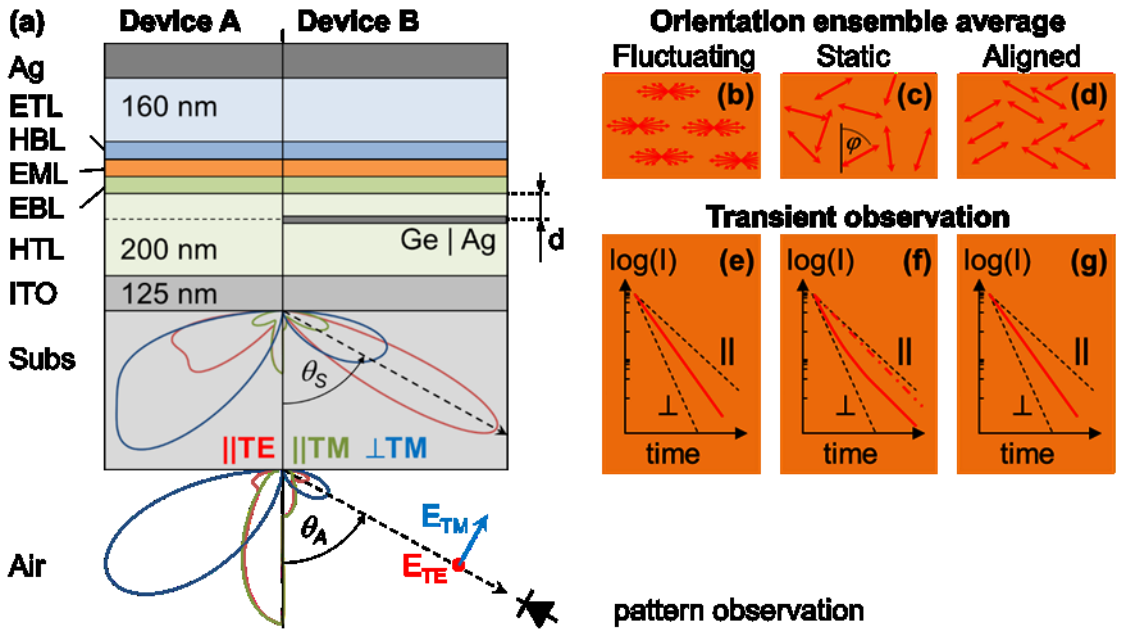

Figure 4.5.1.1 Device emission characteristics. *The geometry of the two OLED types (a) is shown with an illustration of the orientation averaging (b, c, d) and the expected transient observation (e, f, g). In (a) the emission patterns generated by the three orthogonal dipoles are plotted inside the substrate (angle θ_S with respect to the normal, accessed experimentally by half ball lens coupling) or in air (angle θ_A) for a 30 nm. HTL spacer device. Observation direction and orientation of the polarized electric field are shown. The temporal evolution of the intensity observed in a transient experiment is shown in for the fluctuating (b), static (c) and aligned (d) cases in diagrams (e), (f) and (g), respectively. The latter diagrams plot the transient intensity observed for strictly parallel (||) or perpendicular (⊥) emitters (black dashed) along with the ensemble observations (straight red). Diagram (f) additional includes another time trace expected for any different observation direction.*

As discussed in Section 4.4, PL experiments have been conducted because their higher q than EL enables the emission lifetime difference effect to be observed outside of the experimental error. As has been previously found [47], no effect of the pump polarization on the emitted intensities has been found. This means that even if 0° TE excitation is applied, EL-like emission from all emitter orientations occurs. The polarized emission is independent of both the excitation direction and the excitation polarization, for both in-plane emission from mostly parallel emitters and out-of-plane emission from mostly perpendicular emitters. Possible

reasons for this will be discussed in the next section. Transient data of one temporally resolved PL experiment is shown in Figure 4.5.1.2.

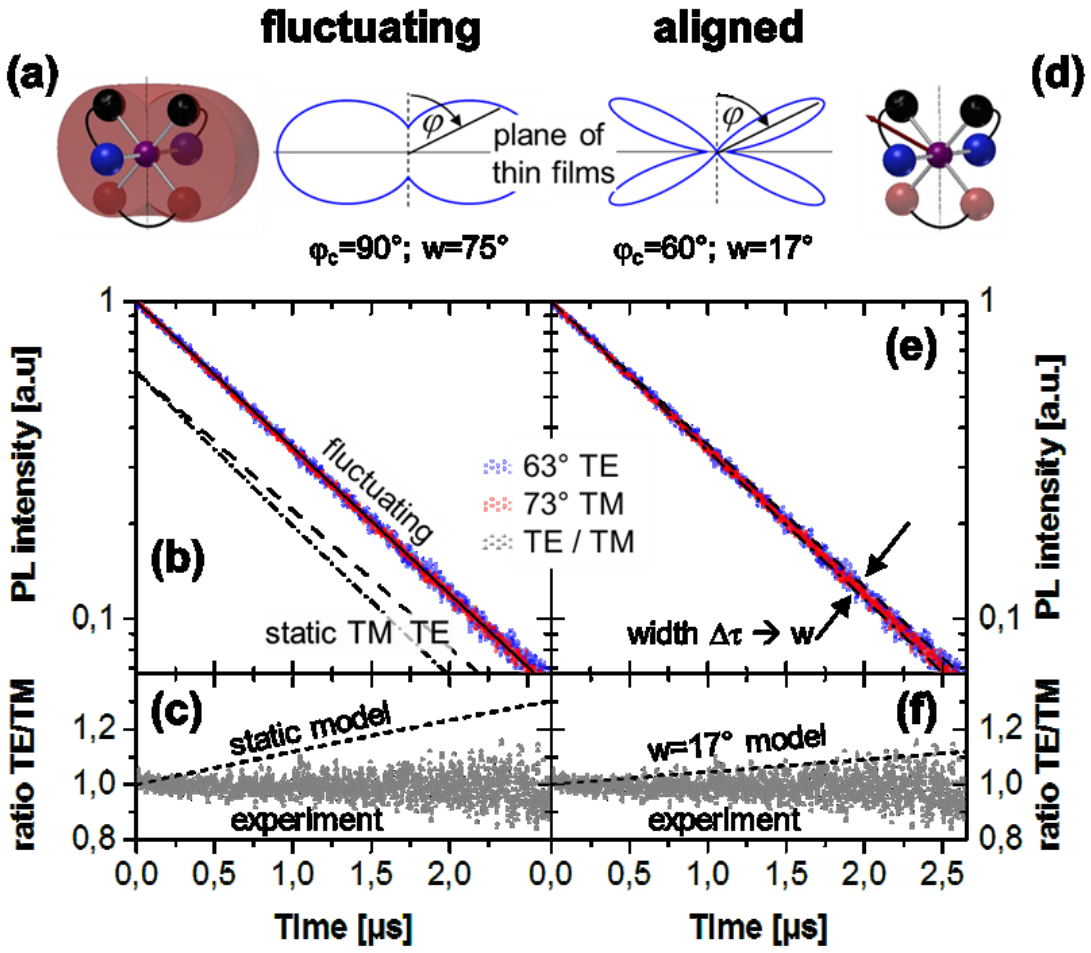

Figure 4.5.1.2 Polarization filtered emission lifetime measurements. *Analysis of one experimental data set obtained for device B with a 30 nm HTL spacer layer to analyze the EOD of the emitter ensemble. Dots represent experimental data for TE θ_S=63° (red), TM θ_S=73° (blue) as well as their ratio (grey). The fluctuating average (a) is modelled by a horizontally centred, wide Gaussian function and predicts a single exponential decay (b), the decay time of which (straight black line, τ=0.93 µs) would change in case of a static ensemble average to TE (dashed, τ=0.88 µs), static TM (dash dot, τ=1.00 µs). The same fact is well illustrated by the ratio of TE and TM polarized intensities in (c). Assuming an aligned ensemble with a narrow Gaussian distribution (d) models the experimental data well (e, f). From the experimental errors an upper limit of the distribution in the w~17° range can be deduced. Figures (a, d) illustrate the distribution function assumed in the model along with the molecular geometry adapted from Ref. [54]. This value is not taken from an absolute simulation value but a relative simulation difference.*

Different observation conditions have been set-up to preferably view parallel or mostly perpendicularly emitters. However, as discussed in Section 4.4, both transient data sets are indistinguishable (see the constant intensity ratio (grey dots) in Fig.4.5.1.2(c) and do not point towards observation dependent emission lifetimes. It should be noted here that the thin metal interlayer causes a large lifetime difference compared with the non-interlayer devices (Fig.4.4.2.1). However, this lifetime change is equally recorded for parallel and perpendicular observation measurements. The simulated static TE parallel emitter, static TM perpendicular emitter and fluctuating model decays have emission lifetimes of τ=0.88 µs, τ=1.00 µs and τ=0.93 µs respectively. For the static model an emission lifetime difference between parallel and perpendicular emitter decays of 0.12 µs results. Radiative lifetime variations due to emitter orientation or external cavity alterations decrease with decreasing intrinsic quantum efficiency. In the case of EL with a low q of only 30%, the two ensemble averages will yield emission lifetime differences in the range of 0.02 µs only. This was within the range of experimental errors. Accordingly, a conclusion from the EL time traces on the ensemble averaging and/or the EOD angular width cannot be made. But the large emitter quantum efficiency obtained in the PL case allows one to distinguish such an emission lifetime separation.

The simulations in Fig.4.5.1.2 assume an extended EZP. A confined EZP as resulted in Section 4.1.2 would result in a different orientation ratio and also lead to a small position dependent lifetime effect (Fig.4.1.2.2). Due to both these effects, the simulated static perpendicular emitter emission lifetime and fluctuating emission lifetime as seen in Fig.4.5.1.2 would change slightly from 0.88 µs to 0.89 µs and 0.93 µs to 0.94 µs respectively. The emission lifetime for static simulated parallel emitter lifetime would not change within two decimal places.

The EL emission intensity based orientation ratio analysis indicates the expected preferred parallel EOD. As outlined previously, only the relative emitter contributions of parallel or perpendicular emitters can be extracted. This ratio will be used as a constraint for a more detailed angular EOD analysis. Any EOD model is an assumption and cannot be further quantified by this experiment. Therefore, one could exemplarily assume two different situations: (i) A Gaussian EOD, which gave the best fit for comparable experiments performed by M.D. Pace et al. [130],

centered in the plane of layers φ_c= 90° with an approximate width w~75° (Fig. 4.5.1.2a). This corresponds to an "almost isotropic" ensemble with slightly less perpendicularly aligned emitters, matching the orientation ratio previously extracted from angular intensity spectra. (ii) Another valid assumption is all molecules being oriented at an "average" angle $\bar{\varphi}$ ≈59.6°, corresponding to a perfectly aligned ensemble, matching the previously extracted orientation ratio. Note that the latter value is only slightly above the "magic angle" (the angle between the 3D diagonal of a cube and any of its three connecting edges), $\overline{\varphi_{iso}}$ ≈54.7° obtained in fluorescence anisotropy measurements of isotropic ensembles.

Emission lifetimes will be used for judging these different assumptions. The experimental observations yield a single exponential time trace that contradicts the presence of multiple, sufficiently different single exponential decays associated with different orientations. Therefore a fluctuating ensemble average exhibiting the emission rate $\langle\Gamma\rangle_\varphi$ according to Eq. 2.5.3 might be deduced and fits the simulations shown in Fig.4.5.1.2(b, c) well. Previous single molecule experiments on single homoleptic emitters [99] could support such a conclusion. But computational models of the TDMs in the present heteroleptic emitter Ir(MDQ)$_2$(acac) shows practically overlapping TDMs of the two ligands [53]. This assumption of only one possible TDM direction rules out a fluctuating ensemble average. Rotation of the emitter molecule could cause some orientation randomization. However, sufficient energy reorientation via rotation of the whole molecule is very unlikely due to the EML host's glass transition temperature of 96° C [131]. Below this temperature there is little molecular motion in amorphous molecular materials [132, 133]. If such a motion were to occur, it would have a much slower timescale than the emission process of Ir(MDQ)$_2$(acac) (~µs) [96, 134]. Intermolecular transfer processes could also cause orientation randomization. But transfer of the excitation energy to the EML matrix or directly neighboring layers are not expected because of the increased gap width of these materials, which was experimentally apparent by missing absorption in the optical properties at wavelengths equal or larger than the excitation. Interactions of excited emitter molecules are mediated by Förster transfer, the radius of which has been reported to be in the 2 nm range [135]. Such a value is approximately a factor two below the average emitter separation resulting from a 3% emitter

concentration. Furthermore, concentration dependent effects should be apparent in case of excited state interactions. These have been observed for the same emitter in a different host above emitter molecule concentrations of 18% [136], which is well above the 3% emitter used here.

According to these arguments, the static ensemble average applies. Then, the single exponential emission lifetime observed indicates a rather narrow EOD of emission lifetimes. As different observation conditions yield the same emission lifetime, a narrow angular EOD was deduced. The EOD shown in Fig.4.5.1.2(d) illustrates such a case when supposing the EOD to be of a Gaussian shape. Increasing the width of such a narrow EOD will increase the differences observed in the emission lifetimes outside of the experimental error. Therefore, from the uncertainty of the emission lifetime measurement ($\Delta\tau$±0.02 μs) a reasonable upper limit for the EOD width $w \leq 17°$ (with an extended EZP this value remains the same) can be extracted. The corresponding simulations are shown in 4.5.1.2(e, f). This suggests a rather well oriented TDM ensemble for the emitter under study. However, a fuller understanding of the orientation dynamics in the photoluminescence of in this system is needed to completely rule out a fluctuating hypothesis. Verification of this narrow EOD result could be verified by the method of electron spin resonance (ESR) spectroscopy. In ESR spectroscopy the electron spins of the probe molecule interact with an applied magnetic field to produce line shapes which depend on the EOD of the molecules. M.D. Pace et al. used this method to measure the EOD of transition metal ions doped at 3% into an organic phthalocyanine ring host film [137]. The transition metal ions were used as probes to indirectly measure the host EOD due to their paramagnetic properties, which bodes well for the use of ESR spectroscopy in the EOD measurement of current phosphorescent emitters. An EOD width w= 30°, with $\bar{\varphi}$ =80°, resulted. Similar experiments this group performed on $CuPcX_4$ [130] resulted in a much narrower EOD width w= 5°, with $\bar{\varphi} = 80°$. Azumi et al. [138] performed ESR spectroscopy on the small organometallic molecule PM (tetrakis(3,5-di-t-butylphenyl)porphinatocopper(II)) which was found to have two orientation components due to aggregation of the molecules. The main component had EOD width w ≈ 14°, with $\bar{\varphi} = 58°$ and the second component an EOD width w ≈ 14°, with $\bar{\varphi}$ =80°.

4.5.2. Excitation reorientation in non-interlayer devices:

It was observed that there was a reorientation of excitation energy from absorption to emission during polarized photoluminescence experiments. The PL emission was observed to be practically independent of the excitation polarization. This effect is present in the PL excitation of the experiment shown in Fig.4.5.1.2, where linearly polarized excitation is applied to uniformly excite every emitter orientation of the ensemble. The effect that this energy reorientation has on the emission lifetime experiment must be determined.

A device without a inter-layer was analysed in order to analyse the influence of pump polarization on the emission independently. Optical excitation was at normal incidence and TE polarized. The emission of mostly parallel emitters in air at θ_A =23° (closest to normal observation possible due to mechanical limits) in air was detected. Without the additional inter-layer, the emission intensity in air allows one to quantitatively compare the spectra with different simulation models. Fig. 4.5.2.1 illustrates this comparison for all combinations of excitation and detection polarizations. All simulated curves have been scaled to the data with the same factor. An intensity error of 6% was measured to be caused by polarization switching.

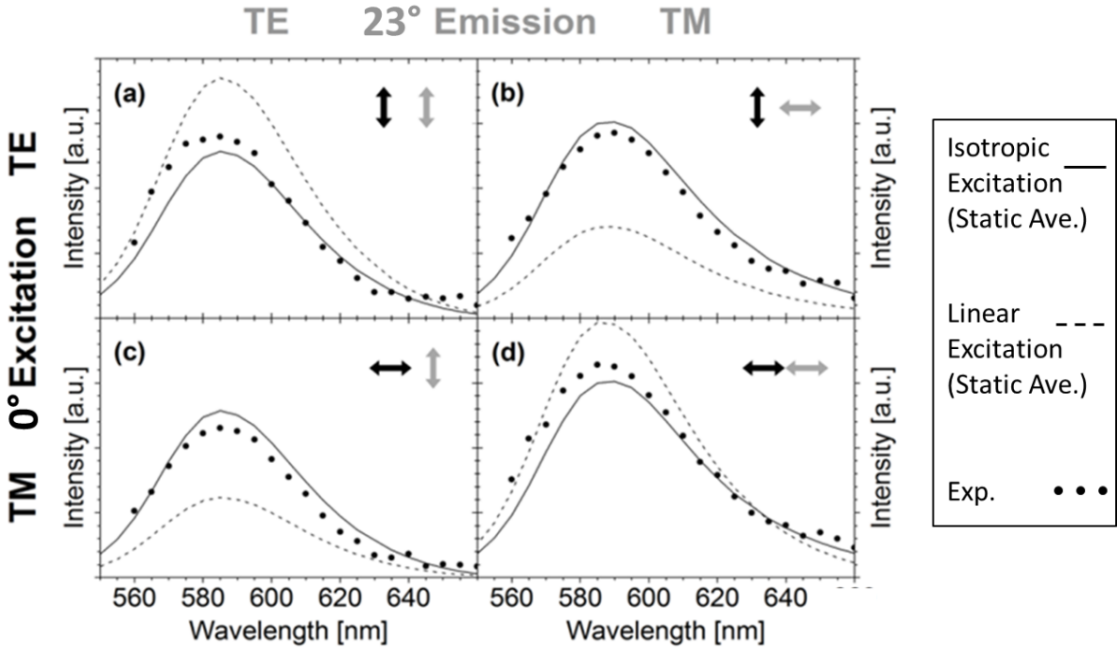

Figure 4.5.2.1 In-plane polarized PL of non- inter-layer device with d_{sp}=30 nm. *Different excitation/ emission polarization combinations are shown for 23° emission, where parallel emitter emission dominates. Experimental PL emission spectra for device A without additional inter-layer (dots) are shown with simulations assuming isotropic excitation (solid curve) or linear excitation (dashed line). TE (a, b) and TM (c, d) polarized excitation is shown along with TE (a, c) and TM (b, d) polarized detection. Inset black (excitation) and grey (emission) arrows illustrate the respective polarizations for convenience.*

Figs. 4.5.2.1 and Fig.4.5.2.2 plot the absolute experimental spectral intensities for different excitation and observation conditions. Simulations have been performed when assuming the excitation of a single emitter to be proportional to the squared cosine of the angle between the exciting electric field and the (oriented) emitter. TE polarized excitation is then modelled by an electric field along one coordinate (e.g. y) while TM polarized excitation would be aligned along the orthogonal in-plane coordinate (x). The "isotropic" model has been compiled from the average of three excitations along the three axes of the coordinate system.

Emission at a higher angles of 68° was also analysed as seen in Fig.4.5.2.2 to show out of plane effects where perpendicular emitter emission dominates. Normalisation was performed as for the results of Fig.4.5.2.1.

In both experiments emission was shown to be independent of excitation and/or detection polarization within the absolute intensity uncertainty, indicating an internal orientation redistribution of the excitation energy from absorption to emission. Detected intensity was expected to vary when changing the polarizations, with much decreased intensity for orthogonal polarizations. But, all four spectra yield emission intensities that agree well with the emission of an isotropically excited ensemble (taking into account our preferred parallel EOD). Measurements at 45° clockwise and counter-clockwise (data not shown for conciseness) also showed the same emission intensity (as the same measurements shown in Fig.4.5.2.1. and Fig.4.5.2.2 but rotated in the device layer plane shown in the figures), indicating a homogenous in-plane EOD.

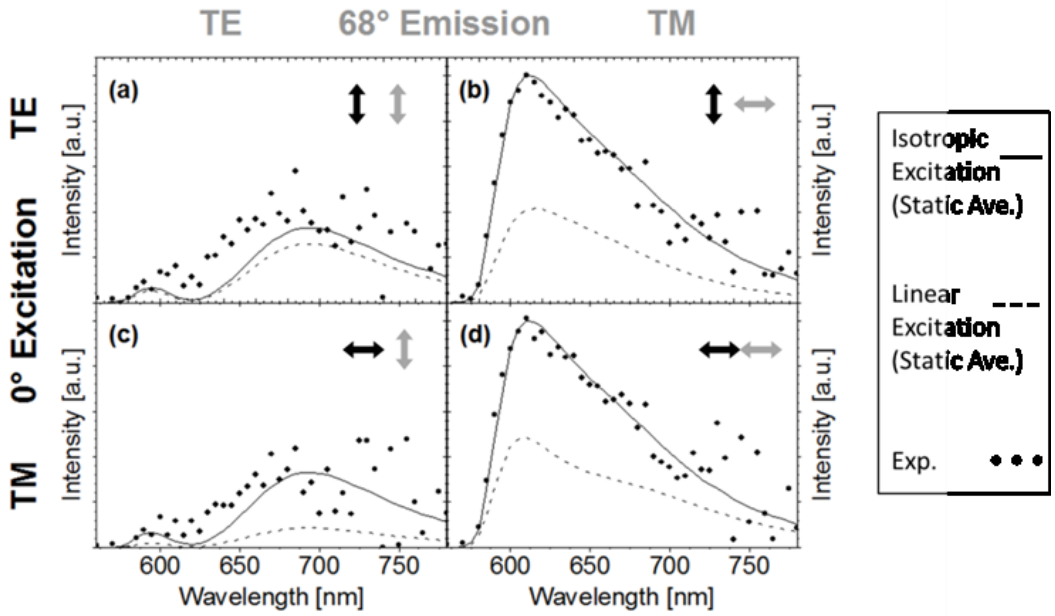

Fig.4.5.2.2 Out-of-plane polarized PL of non-inter-layer device with d_{sp}=30 nm. *Results of different in-plane excitation/ emission polarization combinations are shown which deals mostly with perpendicular emission. Experimental PL emission spectra for device A without additional metal layer (dots) are shown with simulations assuming the static average S with isotropic (solid curve) and linear PL excitation (dashed line) when combining TE (a, b) and TM (c, d) polarized excitation with TE (a, c) and TM (b, d) polarized detection. Black (excitation) and grey (emission) arrows illustrate the respective polarizations for convenience.*

Possible physical mechanisms to explain this energy reorientation result are hereby addressed. Lamansky et al. illustrate that the emitter has a triplet ^{3}MLCT

absorption band from ~435 nm to 550 nm [117] and Tang et al. agree [83]. The laser illumination should be absorbed via charge transfer by TDMs which have a sufficiently matched orientation to the laser polarization. The intrinsic spectrum extracted from the device (Section 4.2) matches very well with known PL spectra of the emitter molecule. Emission from the emitter is also from a ^{3}MLCT state [83, 117]. Energy reorientation via rotation of the whole molecule and energy transfer with other molecules has already been ruled out in Section 4.5.1. Different orientations of absorption and emission TDMs seems to be the most probable explanation for this energy redistribution. Either excited state, two-photon, ^{3}LC or different orientation ^{3}MLCT absorptions could occur in addition to an ^{3}MLCT absorption of the same orientation as the emission ^{3}MLCT TDM as discussed below;

(a) The excitation optical power of Section 2.1 here was relatively low at ~150 mW/cm^2 so it was assumed that excited state absorption was negligible. Excited state absorption for $MLCT_3$ states of other heteroleptic phosphors were shown to have a significant extinction coefficient of ~1000 M^{-1} cm^{-1} at the 515 nm wavelength of excitation of the experiments of Fig.4.5.2.1 and Fig.4.5.2.2 but only after excitation at 266 nm at power of the order of 100 W/cm^2 with a Xenon lamp [139].

(b) Two photon absorption was assumed to be unlikely in the experiments of Fig.4.5.2.1 and Fig.4.5.2.2 . Very high optical intensities in the range of kW cm^{-2} were needed to observe two-photon absorption in another organometallic Ir(III) phosphor $Ir(ppy)_3$ resulting in ns timescale fluorescence [140], which was not observed in the temporal resolved experiments of this work.

(c) At the same energy as the ^{3}MLCT absorption band of $Ir(MDQ)_2(acac)$, there could be a ^{3}LC absorption band. You et al. [141] and Columbo et al. [142] state that in Ir(III) complexes the ^{3}MLCT and ^{3}LC absorption bands are seldom distinguished due to their small molar absorbances and featureless band shapes and that the ^{3}LC absorption states are probably buried under the ^{3}MLCT states. However, Lamansky et al. state that the absorption at 515 nm (the

excitation wavelength in this dissertation work) is solely due to ^{3}MLCT excitation [117].

(d) Our emitting system features a Stokes shift of 0.3 eV, so it is possible that higher energy ^{3}MLCT TDMs exist, possibly at different orientations, where absorption is possible. Harbach and Dreuw show that many higher excited states are available for energy localization in a simpler dimer molecule and predict it to be so for larger molecules [143].

(e) Interligand energy transfer could cause different orientation of the absorption and emission TDMs. An orientation difference between the absorption and emission dipole due to interligand energy transfer (over ns timescale) could explain finding (1). Higher energy TDM at other ligands/orientations could be excited before emission from the lowest energy TDM as detailed for other heteroleptic Ir(III) complexes [141,144,145]. However, this effect has not been reported for Ir(MDQ)$_2$(acac).

In summary, firstly, the most probable situation to explain this finding is (d), where the ^{3}MLCT absorption TDM is differently oriented to the ^{3}MLCT emission TDM, with angle between them of ψ_{abs-em}, seems the most likely. Small organic molecules with heavy halogen substitutions have been reported in the literature to have such differently oriented dipoles. Rhodamine 6G was reported to have a ψ_{abs-em} of 13° +/- 3° with the assumption of planar oriented dipoles [146]. Fluorescence from Erythrosine B was measured to have a ψ_{abs-em} of 55° +/- 2° for absorption at 355 nm and a ψ_{abs-em} of 13° +/- 2° for absorption at 532 nm [147]. In the same paper, phosphorescence from Erythrosine B was measured to have a ψ_{abs-em} of 55° +/- 2° for absorption at 355 nm and a ψ_{abs-em} of 29° +/- 1° for absorption at 532 nm. The same group then measured three similar derivative molecules and found similar values [148]. Fluorescence of DiIC1(5) was fitted to have a ψ_{abs-em} of 32° [149]. Unfortunately no literature examples have been found which investigate ψ_{abs-em} for organometallic small molecules like ours. As a rough estimate, without taking microcavity effects into account and assuming an isotropic EOD, following Lettinga et al. [147], a ψ_{abs-em} of ~ 55° would be required to account the low photoluminescence anisotropy observed in Fig.4.5.2.1.

This hypothesis could be investigated by a polarized absorption analysis of thin films [138] to isolate the absorption TDM orientation. Additionally, ultrafast absorption transmission spectroscopy of thin films [141, 150] could give information on the dynamics of the absorption TDM

4.5.3 Excitation reorientation in interlayer devices

In principle, it is possible to extract information on the EOD width from parallel and perpendicular emitter emitted intensities of devices B. However, for emission intensity measurements, the energy redistribution effect must also be accounted for. If a complete redistribution of energy as per the results of Section 4.5.2 is assumed, an estimation of EOD width can be obtained. EL has been shown to have q =0.30, so not enough to observe a usable parallel-perpendicular emitter lifetime difference. TE polarized normal excitation causing isotropic excitation results in a PL with a q =0.82. A half ball lens was used for the inter-layer containing OLEDs as too low an intensity was emitted in air.

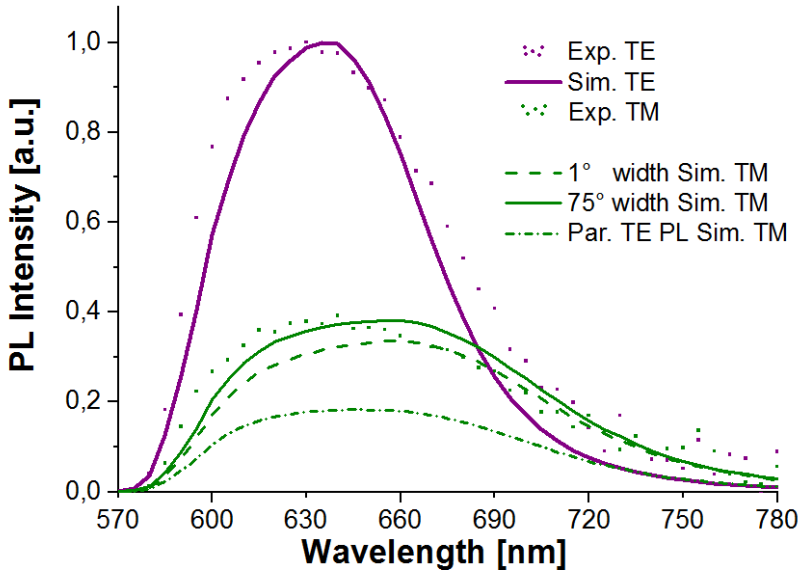

Figure 4.5.3.1 Out of plane polarized PL of inter-layer device with d_{sp}=30 nm. *TE emission (purple) and TM emission (green) are shown. Experimental (dots), 1° width, 60° centre EOD simulated TM (dashed line), 75° width, 90° centre EOD simulated TM (solid line) and 1° width, 60° centre EOD PL simulated TM (dashdot) emission are shown. The various TE simulations are identical here as all TE and TM different excitation data sets are normalized to the TE maximum. A 17° EOD width simulated TM curve (data not shown) lies between the 1° and 75° cases. Widths of 1° or 75° for the PL TM simulation do not vary significantly.*

PL emission filtered for TE polarization maximized the visibility of parallel emitters, and then detection with TM polarization allowed observation of mostly perpendicular emitter contributions. Both polarizations were observed at θ_S=63° which gives a high intensity level for both. Normalisation was performed as before in Section 4.5.2.

One of the prerequisites of this analysis was sufficient emission from perpendicular emitters. TE polarized excitation at normal incidence used here has resulted in the highest parallel and, counterintuitively, also the highest perpendicular emitter emission. It should be noted here that this excitation angle excites the highest electric field in the device EML, albeit at a parallel orientation. As in the non- inter-layer case, near isotropic excitation was observed in spite of the initial linear incident light. This is seen in Fig.4.5.3.1 where the PL (linear excitation) case would excite fewer perpendicular emitters to emit, but much more perpendicular emitter emission was observed fitting the isotropic EL excitation assumption well. At lower wavelengths the wider EOD seems to fit better, but at higher wavelengths the thinner EOD. In conclusion, details of the EOD width cannot be determined from this experiment due to the high uncertainty of the data for inter-layer devices.

4.5.4 Intrinsic quantum efficiency: EL and PL spectral intensity comparison

EL and PL have quite different quantum efficiencies. The difference between perpendicular and parallel emitter emission rates depends on this q. If the different excitation methods do not create an additional anisotropy effect, the angular intensity spectra from both can be compared to give information on how fully parallel or perpendicularly aligned the emitters are.

We can define a ratio u which depends on the intrinsic quantum efficiency of EL and PL:

$$\boldsymbol{u} = \left(\frac{\boldsymbol{I}_{\parallel}}{\boldsymbol{I}_{\perp}}\right)_{\boldsymbol{EL}} / \left(\frac{\boldsymbol{I}_{\parallel}}{\boldsymbol{I}_{\perp}}\right)_{\boldsymbol{PL}} \tag{4.5.4}$$

where $I_{\parallel}$ is the intensity measured at an emission angle of 67°, a wavelength of λ =625 nm and TE polarization filtered. These observation conditions detect a maximum emission intensity from parallel emitters at an experimentally feasible angle for PL (θ_S =0° observation gives a slightly higher intensity but was not feasible as for simpler simulation a PL excitation angle of θ_S =0° was used). $I_{\perp}$ is

the intensity measured at an emission angle of θ_S =79°, a wavelength of λ =625 nm and with TM polarization filtering. These observation conditions detect a maximum perpendicular:parallel emitter emission intensity ratio. This ratio u will differ for the single emitter orientation approximation whereby all emitters experience similar damping or for the EOD centered in the plane of layers at $\varphi_c = 90°$ with an approximate width ~75° within the parallel preferred limit, whereby emitters with a more perpendicular orientation will be damped more compared to more parallel emitters. This analysis was performed for Device B with 30 nm HTL spacer that gives the highest perpendicular:parallel emitter emission ratios, upon which observation of the EOD width above experimental noise was dependent. The PL signal for emission in air was too low to measure accurately enough with the measurement setup, even though one would have a 15.2% difference in u between a single emitter orientation and the wide EOD. For substrate mode emission, viewed with the use of an attached half ball lens, the difference in u for the two EODs was calculated from simulations to be 8.7%. These 15.2% and 8.7% values were calculated for an extended EZP, which gives a higher perpendicular emitter contribution and has a slightly higher percentage difference than the confined EZP. Unfortunately due to the experimental error of the measurement setup the measured u has approximately the same value. In Fig. 4.5.4.1 the high noise level of the EL measurement for the inter-layer device can be seen for confirmation.

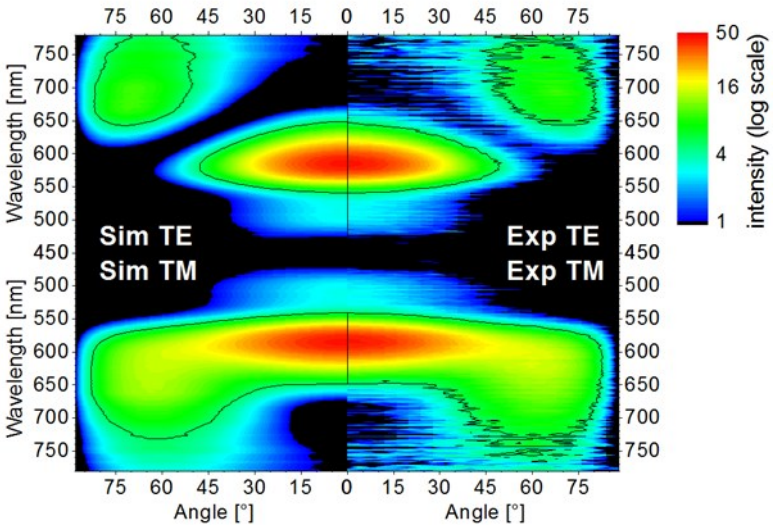

Figure 4.5.4.1 Inter-layer device EL angular spectra comparison. *The device has a 30nm HTL spacer. High noise levels can be observed, compare with Fig.4.1.2.3 (TE) and Fig.4.3.2 (TM).*

If a inter-layer device with better charge behaviour giving a higher EL intrinsic quantum efficiency were available, the spectral measurements could have been used to support the emission lifetime results of Section 4.5.1. Additionally with such a device, EL emission lifetime analysis would completely rule out possible PL selective excitation effects, and the OLED would be analysed in the same operation mode as the device would normally be used.

5. RESULTS & DISCUSSION: DUAL EMITTER DEVICES

Single emitter AOP (active optical property) extraction is an established analysis procedure as discussed in Section 3.3. However, as previously mentioned, the latest commercial displays and lighting products, are generally composed of OLED devices featuring two or three layers of different-colour emitters. Therefore it is much desired to expand AOP extraction to analyze multi-emitter OLEDs. This is however not straightforward. When obtaining knowledge of single emitter device AOPs, the measured emission is from a single emitter species. When a dual or triple-emitter device is operated, generally all emitter types emit at the same time. Small molecule emitters used in OLEDs have wide intrinsic emission spectra at room temperature due to disorder effects and their complex morphology [151]. The resultant full width at half maximum of the emission spectrum is typically in the range of 0.3 eV and corresponds to a ~50…100 nm spectral width. To cover the whole visible light spectrum (~ 300 nm) usually three emitters (blue, green and red) are needed. The intrinsic spectra of these emitters will generally overlap (as can be seen in the case of the green PL and red EL spectra of Fig.5.1.1). Consequently, when emitted radiation of such a multi-emitter stack is measured, it is not usually possible to find wavelength ranges where each emitter emits alone. This chapter describes an attempt to extract the individual properties of two emitters in a dual-emitter device. Findings will then be compared to single emitter device results.

5.1 Adaption of AOP extraction methods for the dual emitter case

OLED devices with a dual emitter system were manufactured as described in Section 3.1.3. To obtain information on the AOP of an individual emitter, the measured emission from only that emitter should be analysed. As can be seen from

Fig.5.1.1, this can be possible with a limited wavelength range for the green emitter but for AOP analysis at red emitter wavelengths, significant green emitter emission is also measured. To obtain an assumption of only red emitter emission, the green emitters' emission needs to be simulated and subtracted from the total emission measured. To do this, an assumption of the green emitters' intrinsic spectrum in the region where both spectra overlap is necessary. The PL spectrum for a single green EML layer from these devices provided by the manufacturer was used as the assumed individual spectrum. To check the validity of this assumption, the red EL intrinsic spectrum of Section 4.2 was assumed to be the red emitter individual spectrum. The device of Section 4.2 has the same emission system as the red EML of these dual-colour devices but with a slightly different emitter concentration (3% rather than 5%). The sum of these two spectra was then compared with the extracted intrinsic spectrum of the dual-colour device. The combined intrinsic spectrum was extracted using the experimental angular emission spectrum as explained in Section 4.3, assuming a constant 20 nm EZP covering both the green and red EMLs.

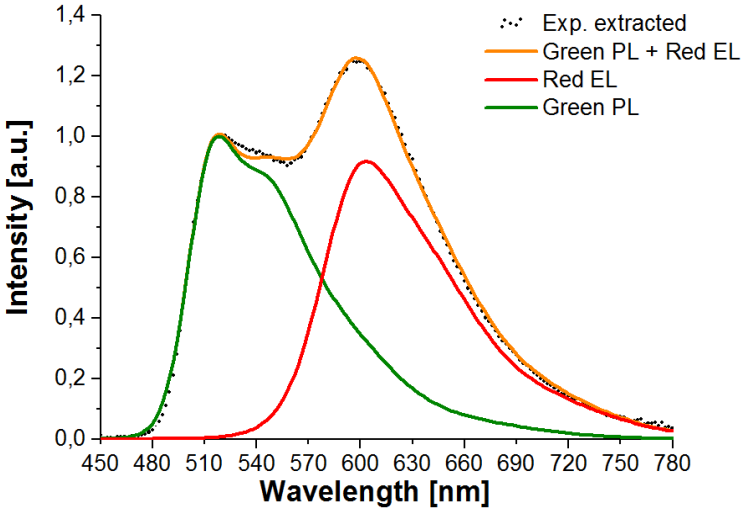

Fig.5.1.1. Dual emitter intrinsic spectrum fitting. *The internal spectrum extracted from the device with the 37 nm ETL is shown as black dots. The green PL spectrum is shown using the green line, the red EL spectrum is shown using the red line and their sum using the orange line. The green PL spectra and the extracted device intrinsic spectrum are normalised at 515 nm and the red EL spectrum is scaled to the best fit.*

The analysis was performed using a device with an ETL thickness of 37 nm which has minimal sensitivity to the EZP at both green and red emission wavelengths

(See Fig.5.1.2). The angular spectra were measured at a current density of 5 mA/cm^2 in the same way as for the single colour devices as detailed in Section 3.2.1. The slight discrepancy at 490 nm is not crucial as green emitter AOPs can be extracted as single emitter devices around this wavelength point. For the device with the 37 nm ETL, a certain green to red spectral ratio fits the experimental extracted spectrum. However it should be noted that the green to red intrinsic spectral ratio changes for devices with different ETL thicknesses due to microcavity interference effects. For all devices with varying ETLs, using the assumed individual spectra, the red emission of the devices is not more than 1% of the green emission for λ <530 nm. Therefore, in this chapter, it is assumed that there is no red emission present at wavelengths below 530 nm. In this wavelength range, the green AOPs of the dual colour devices can be extracted as for the single emitter red devices of the Chapter 4. The green EZP results are analysed in section 5.1 and the green orientation ratio results in section 5.2.

To extract red emitter AOPs, the emission from the red emitters was simulated (whilst varying the relevant AOP) and compared to an assumed red emitter emission pattern. This assumed red emission was calculated by subtracting the simulated green emission from the experimentally measured combined emission of green and red emitters. The green emission was simulated using the previously extracted green AOPs and the assumed green emission spectrum for wavelengths of 530 nm and above (the wavelength region of red emitter emission).

As can be seen also in Fig.5.1.1, the green PL spectrum along with the red EL spectrum fits the extracted intrinsic spectrum of the device well. Some discrepancies in the fit between the extracted combined spectrum and the sum of the assumed individual emitter intrinsic spectra can be observed at $\lambda \sim$530 nm which could be due to the green spectrum having a different spectral shape due to the presence of the red emitter, energy transfer processes or the fact that this is a PL spectrum compared with an EL measurement. EL spectra should be a better assumption than PL for the actual intrinsic spectra in this analysis as they are to be compared with EL experimental measurements. Because of this, fitting of red emitter properties will be restricted to wavelengths above λ =572 nm. The red intrinsic spectrum extracted in the single emitter device way will then be compared with the expected red EL spectrum.

As described in Section 3.3, devices with different ETL thicknesses have different sensitivity to EZP and orientation ratio. As a microcavity interference effect, this dependency is also wavelength dependent. To choose devices which are most sensitive to EZP, the emitted intensity in air at θ_A=45° from parallel emitters only was simulated and is plotted in Fig.5.1.2(a). An angle of θ_A =45° was chosen to have as much as possible of the EZP-sensitive interference minimum in the angular spectrum from θ_A = 0°…90°. Only parallel emitters are chosen so that there is no dependence on the orientation ratio. For emission at the chosen green wavelength of λ =510 nm it can be seen from Fig.5.1.2(a) that devices with the 124 nm ETL and the 285 nm ETLs have the most destructive interference of the observed intensity at the green wavelength and so are the most sensitive to the EZP (Section 3.3). The green representative wavelength was chosen as λ =510 nm as the midpoint between the low noise level at λ =490 nm and the onset of significant red emission at λ =530 nm. The red representative wavelength was chosen as λ =640 nm as it is the midpoint between a low red to green emission ratio at lower wavelengths and a low SNR at higher wavelengths. Devices with an ETL of 124 nm, 165 nm and 325 nm have the most destructive interference at the red wavelength and so are the most sensitive to the EZP. The green EZP results are shown in Section 5.2 and the red EZP ratio results in Section 5.4.

To choose devices which are most sensitive to orientation ratio, the angular integrated emission from θ_A= 0°…90° from perpendicular emitters is simulated and plotted in Fig5.1.2(b). High perpendicular emission is the most crucial property to measure an orientation ratio as in optimised devices perpendicular emission is of a very low intensity (Section 2.3). Emission from all angles is helpful in extracting the orientation ratio. It can be seen that for the green wavelength, the devices with the highest perpendicular emission are those with ETLs of 124 nm, 250 nm and 285 nm thicknesses. The 124 nm ETL device shows also a high red perpendicular emission but this will not affect the green orientation ratio extraction due to the chosen fitting wavelength range. For the red wavelength, the devices with the highest perpendicular emission are those with ETLs of 124 nm, 165 nm and 325 nm thicknesses. The device with the 124 nm ETL also has a high green perpendicular contribution and because of the spectral overlap, this device is not very sensitive to the red orientation ratio. The green

orientation ratio results will be discussed in Section 5.3 and the red orientation ratio results in Section 5.5.

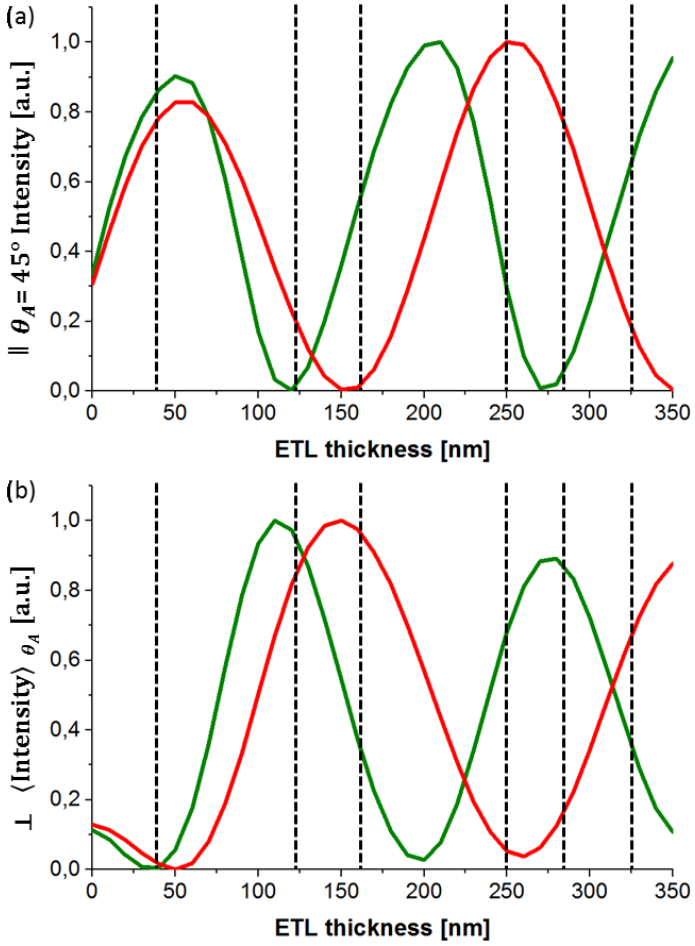

Fig.5.1.2. Choosing the most AOP sensitive devices. *(a) shows the parallel emitter intensity observed at 45° versus ETL thickness. (b) shows the perpendicular emitter observation angle averaged intensity versus ETL thickness. Simulation is for emission from the centre of the green or red EML. The green curve represents a wavelength of 510 nm. The red curve represents a wavelength of 640 nm. Curves shown are for q=1. For different q values the curve maxima scale but the ETL values of the maxima and minima do not change by more than ~4 nm. The ETL thicknesses of devices used in this work are marked with a black vertical dashed line.*

Emitter intrinsic quantum efficiency can significantly affect simulations and therefore EZP and orientation ratio results. It is difficult to measure the individual intrinsic quantum efficiencies in dual-colour devices using decay lifetimes in the same way as in Section 4.5. The red lifetimes measured in Section

4.5 had a natural lifetime of ~ 1.0 μs and the natural lifetime of the green emitter, Ir(ppy)3 is also ~1 μs [152]. So, individual lifetimes are difficult to distinguish when fitting the decay of the combined emission. An EL intrinsic quantum efficiency of the green dye of ~0.4 for 1 mA/cm^2 and ~0.3 for 10 mA/cm^2 was measured for the same emitter and host system, but in a single emitter device [153]. A value of 0.35 will be assumed as the most likely value in the analysis of this chapter due to the 5 mAcm-2. An EL intrinsic quantum efficiency for the red dye of 0.84 has been reported at 1.5 mA/cm^2 in a different host material [126]. Due to the higher current density here, a value of 0.7 will be assumed as the most likely value.

5.2 Green emission zone profile

The most sensitive devices to green wavelength EZP and orientation ratio from observing Fig.5.1.1. are the devices with a λ =124 nm or a λ =285 nm ETL. The EZP is extracted using the same methods as in Section 4.2. Resolution is again limited to cubic eigenfunctions. Simulation of the green emitter emission from the red EML is always stationary as the red EML absorbs at the mean emission wavelength of the green emitters. Emission from the green EML and the HBL are simulated with q =0.35. The EZP is first extracted from the 124 nm ETL device as shown in Fig.5.2.1. The λ =528 nm cross section is shown as it shows the sensitive interference minimum optimally. A wavelength fitting range of λ =490 nm…528 nm was used. The experimental noise level for the green wavelength range was 0.25 (Section 3.4.2).

In Fig.5.2.1, all EZPs are normalised to area 1. The fundamental EZPs which give information on basic EZP details such as the centre position, width and cathode/anode side bias are shown in Fig.5.2.1(a). The best fitting single point EZP is slightly towards the cathode side. In Fig.5.2.1(b) the blue-dotted edge simulated emission fits the experimental data close to the experimental error with RMS_{rel}=1.2. Such an EZP of two discrete edge emission points is highly physically unlikely and it is incompatible with the diffusion hypothesis (Section 4.2.2) as diffusion cannot increase the emitter spatial distribution order due to entropy. Such a solution, with emission concentrated at the EML edges should instead indicate extended emission (Section 4.2.1). In Fig.5.2.1(c) possible extended EZPs are shown. The two-layer limited EZPs do not approach the experimental error but

also show a cathode sided preference. The blue-dotted three-layer EF sum EZP simulation in Fig.5.2.1(d) fits the data within the experimental error with RMS_{rel}=0.7. Therefore from analysis of this device, the evidence suggests an extended, quite central EZP.

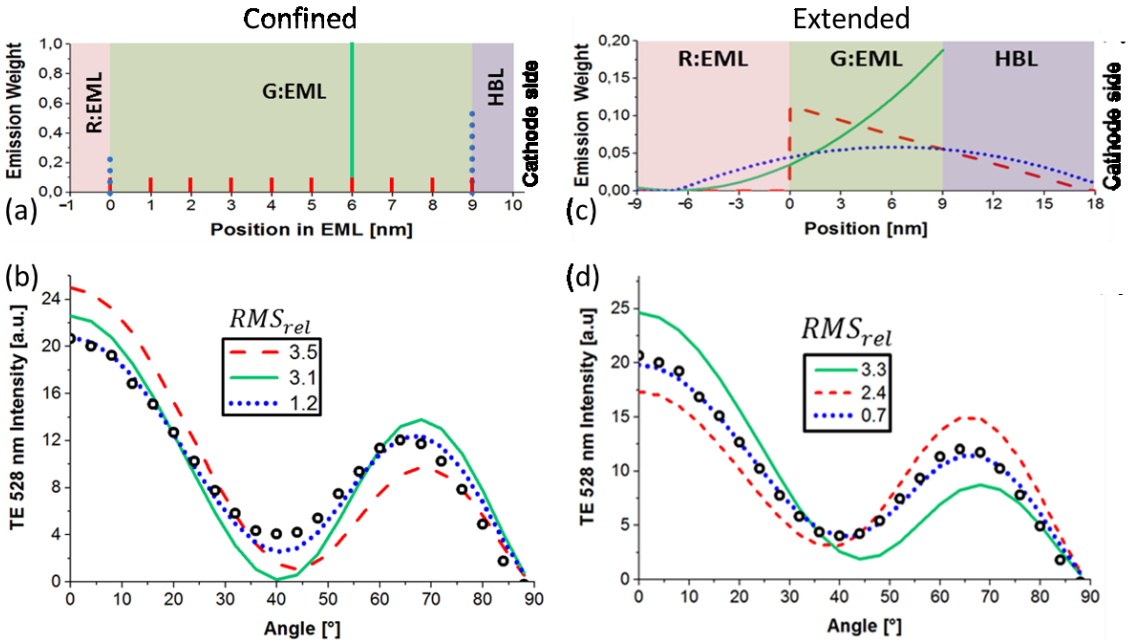

Fig.5.2.1. Green EZP extraction for the 124 nm ETL device. *(a) Shows fundamental confined EZPs. The red lines shows a constant EZP, the blue dotted line the best fitting point-by-point fit and the green line the best fitting single emission point. (b) Shows the resulting simulated angular intensity patterns using these confined EZPs and experimental data (black circles) for λ =528 nm TE emission. Extended EZPs are shown in part (c). The green solid line shows an EF sum solution in the red EML and the green EML, the red lines show a green-EML and HBL EF sum solution and the blue dotted line shows an EF sum solution of the three layers. (d) Shows the resulting simulated angular intensity patterns using these extended EZPs and experimental data (black circles) for λ =528 nm TE emission.*

A simulated versus experimental angular spectra comparison is shown over the green emitter emission range for confined and extended EZPs in Fig.5.2.3. The difference between the confined EZP and extended EZP simulation fits can be observed at the interference minimum centred at λ ~515 nm and θ_A =50°. It can be seen that the extended EZP fits to the experimental data much better.

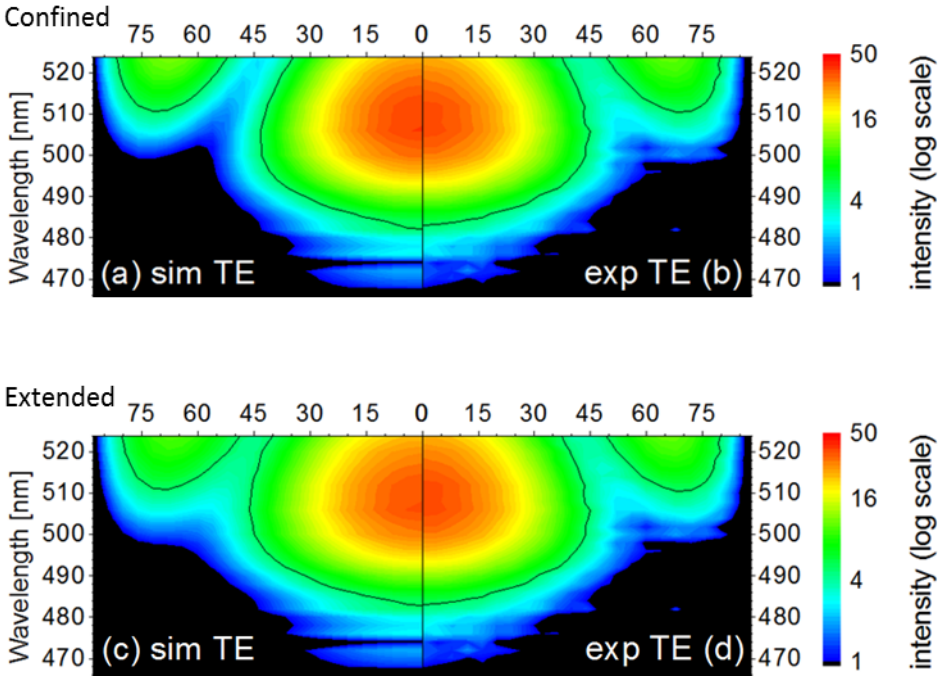

Fig.5.2.3. 124 nm ETL device angular spectra comparison. *The interference minima in the confined EZP simulated angular spectrum (a) is too low compared to the experimental data. The experimental spectrum is shown for comparison twice in (b) and (d). In the extended EZP simulated angular spectrum (c) a better interference minimum (centred at around 515 nm and 50°) fit results. The black contour line shows an intensity value of 5 as a viewing aid. All diagrams have the same intensity scale. Best fitting EZPs were used for the simulations.*

Next, the EZP is extracted from the 285 nm ETL device, the results of which are shown in Fig.5.2.4. The λ =528 nm cross section is shown as it shows the sensitive interference minimum optimally. A wavelength fitting range of λ = 490 nm…528 nm was used. The fundamental EZPs which give information on basic EZP details such as the centre position, width and cathode/anode side bias are shown in Fig.5.2.4(a). The best fitting single point EZP is slightly anode sided. In Fig.5.2.4(b) it can be observed that both a constant and a single point EZP simulation fit the experimental data close to the experimental error with RMS_{rel} =1.1. The best fit of the 11-point point by point fit pushes all emission to the green EML interfaces and fits within the experimental error with RMS_{rel} =0.8, but is not physically expected. More likely, it suggests a slightly extended EZP. In Fig.5.2.4(c) possible extended EZPs are shown. It should be noted here that lifetime simulations were not possible in the red EML due to absorption of the green emission by the red emitters. In Fig.5.2.4(d) it can be observed that the

simulations of both 2-layer EZPs yield an increased error than all the confined EZPs. The 3-layer extended EZP is very central and fits within the experimental error. In summary, the EZP results for this device conclude a very central EZP with a slight extension into the neighbouring layers.

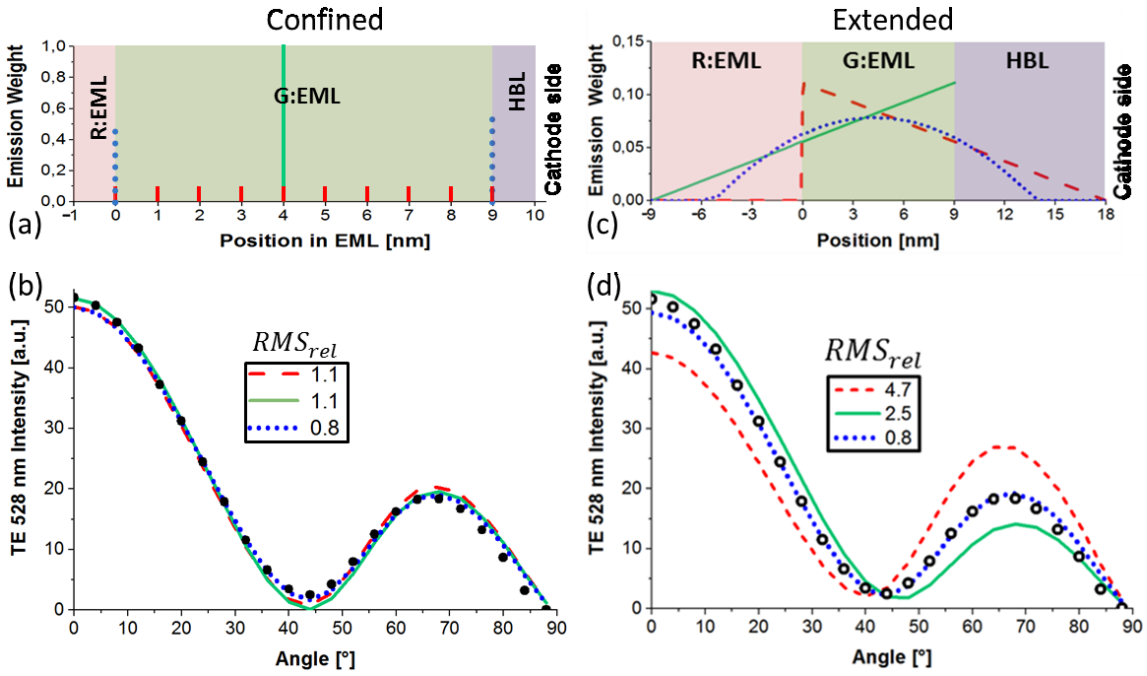

Fig.5.2.4. Green EZP extraction for the 285 nm ETL device. *(a) Shows confined fundamental EZPs. The red dashed line shows a constant EZP, the best fitting point-by-point fit and the best fitting single emission point are the same and are shown by the green line. (b) Shows the resulting simulated angular intensity patterns using these confined EZPs and experimental data (black circles) for λ =528 nm TE emission. Extended EZPs are shown in part (c). The green solid line shows a EF sum solution in the red EML and the green EML, the red lines shows a green-EML and HBL EF sum solution and the blue dotted line shows an EF sum solution of the three layers. (d) Shows the resulting simulated angular intensity patterns using these extended EZPs and experimental data (black circles) for λ =528 nm TE emission.*

A simulated versus experimental angular spectra comparison is shown over the green emitter emission range for confined and extended EZPs in Fig.5.2.5. The difference between the confined EZP and extended EZP simulation fits can be observed at the interference minimum centred at λ ~510 nm and θ_A =55°. It can be seen that the extended EZP fits to the experimental data much better.

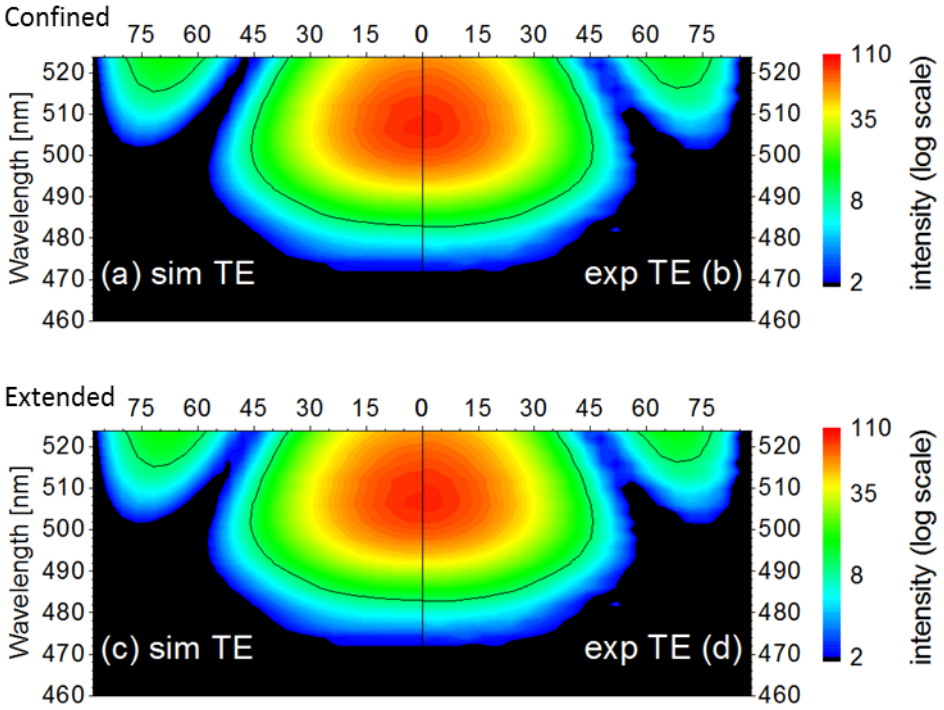

Fig.5.2.5. 285 nm ETL device angular spectra comparison. *The interference minima of the confined EZP simulated angular spectrum (a) is too low compared to the experimental data. The experimental spectrum is shown for comparison twice in (b) and (d). In the extended EZP simulated angular spectrum (c) a much better interference minimum (centred at around 510 nm and 55°) fit results. The black contour line shows an intensity value of 5 as a viewing aid. All diagrams have the same intensity scale. Best fitting EZPs were used for the simulations.*

The effect of Förster energy transfer on emitter lifetimes has been estimated via optical simulation using the measured layer absorptions and an assumed emitter intrinsic quantum efficiency. Energy transfer from green emitters to red emitters or molecules of the ETL would result in a large lifetime decrease which can be observed in Fig. 5.2.2. Green emitters have a higher triplet energy and so can transfer energy to the red emitters (see Fig.3.1.3). It can be observed that, due to energy transfer to the red emitters, a decreased green emitter lifetime occurs even for confined EZPs. The presence of red emitters in the green EML (this will be analysed in section 5.3) would further decrease the green emitter lifetime towards the red EML side. Lifetime simulation in the red EML is not possible due to absorption of this layer at the 556 nm mean wavelength of the green emitter intrinsic spectrum. An extended EZP analysis is important to estimate increased Förster transfer effects due to increased emitter coincidence and the resulting

intrinsic quantum efficiency of the emitters. In this analysis the green q was an assumed value. If the q was somehow measured, then a more accurate energy transfer analysis would result. Emitter lifetimes will decrease more with a higher emitter q as the radiative proportion of available energy increases and vice versa.

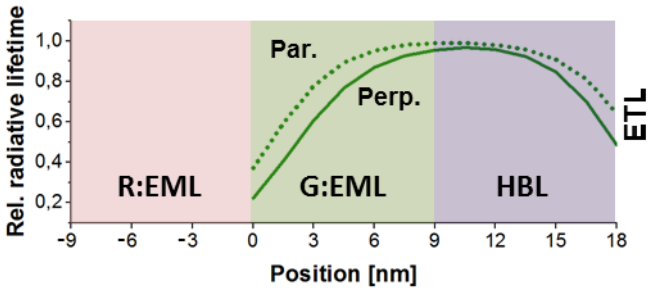

Fig.5.2.2. Green emitter lifetime change with position. Parallel-oriented emitter lifetimes (dotted line) and perpendicular-oriented emitter lifetimes (solid line) are shown versus position. Simulation is of the 124 nm ETL device with q=0.35 at a mean emission wavelength of 550 nm. The lifetime behaviour does not change significantly for devices with differing ETL thicknesses.

In conclusion, for the green emitter EZP, with the 124 nm ETL device, the confined edge emission EZP fits close to the experimental error with RMS_{rel} = 1.2. For the 285 nm ETL device the constant and single point EZPs fit close to the experimental error with RMS_{rel} = 1.1, but such EZPs are physically unexpected and do not fit to a diffusion hypothesis. These devices do not give as strong evidence of a significantly extended EZP as the single emitter device of Section 4.2. With an extended EZP, both devices show a very good fit below the experimental error for central extended EZPs. This EZP could be explained by diffusion of emitters (Section 4.2.2). The extension however, varies and so an average value of the three-layer EF best fit (blue dotted lines) of both devices will be concluded and assumed for the analysis of different ETL devices in the remainder of this chapter. As discussed in Section 3.1.3 recombination should occur at the red EML and green EML interface. Since the green emitters are deposited in the green EML, most emission would be expected there. Both devices are observed to show high emission from the green EML, so this work agrees with the previously published results.

5.3 Green orientation ratio

The two devices most sensitive to green orientation ratio will now be analyzed. These are the devices with the same 124 nm and 285 nm ETLs as were used for the green EZP extraction. Therefore, the best fitting 3-layer EZP of each respective device was used for this orientation ratio analysis. In this analysis, the emitters are assumed to be in different device layers. For different host materials the orientation of the green emitter ($Irppy_3$) was measured to change from isotropic orientation to borderline horizontal [154]. As the experimental data includes possible emission from all layers, the orientation ratio extracted from extended EZP devices here will be an effective 3-layer orientation ratio. The ratio for each individual layer can be varied, but this results in many possible solutions as this analysis does not have the sensitivity to measure such changes. The orientation ratio fitting for the 124 nm ETL device at an illustrative wavelength of λ =510 nm is shown in Fig.5.3.1. The complete green AOP fitting range of λ =490…530 nm contains high levels of both parallel and perpendicular emission and so was used. An orientation ratio ‖: ⊥ =2:1.20 gave the lowest RMS_{rel} = 1.0.

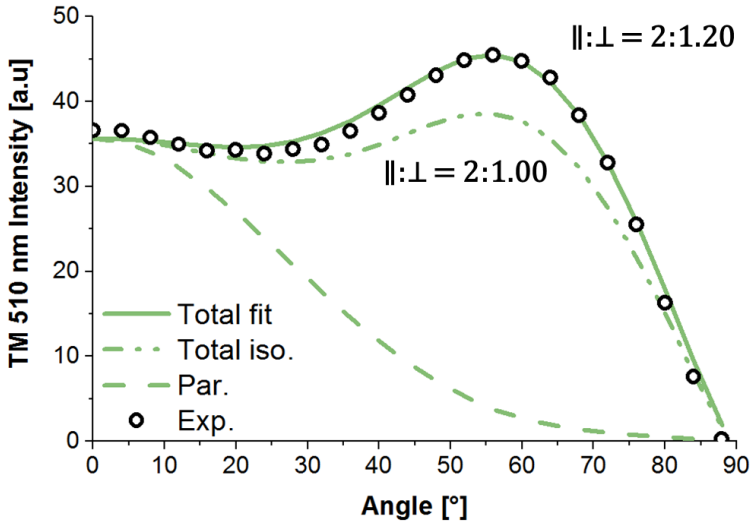

Fig.5.3.1. Orientation ratio fitting for the 124 nm ETL device. *TM emission at an illustrative wavelength of λ =510 nm is shown. The total TM emission for the fitted orientation ratio is shown as the solid green line. The total isotropic TM emission is shown as the dashdot green line. The emission contribution of parallel emitters is shown as the green dashed line. Experimental data points are shown as black circles.*

A small systematic error in fitting, in that simulated emission is lower than the experimental at θ_A=0° but higher at θ_A~35° is evident. Orientation ratio extraction was also performed at increments of 0.1 for q = 0…1. With changing q, the EZP changes slightly. When the corrected best fit EZP is then set, the orientation ratio is $\|:\perp = 2:(1.20 \pm 0.08)$.

The orientation ratio fitting for the 285 nm ETL device is shown in Fig.5.3.2. A fitting range of λ =490..528 nm was used. An orientation ratio ||: ⊥ =2: 1.19 gave the lowest RMS_{rel} = 0.8. A small systematic error in fitting, in that simulated emission is lower than the experimental at θ_A~60° but higher at θ_A~30° is evident.

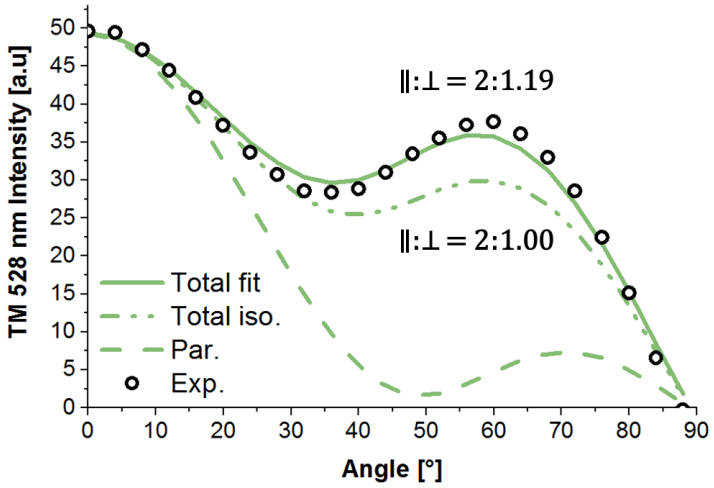

Fig.5.3.2. Orientation ratio fitting for the 285 nm ETL device. *TM emission for an illustrative wavelength of λ =528 nm is shown. The total TM emission for the fitted orientation ratio is shown as the solid green line. The total isotropic TM emission is shown as the dashdot green line. The emission contribution of parallel emitters is shown as the green dashed line. Experimental data points are shown as black circles.*

As explained previously, with a variation of q, the orientation ratio varied as $\|:\perp = 2:(1.20 \pm 0.08)$. To conclude the green orientation results, for both devices, a clearly more perpendicular orientation ratio than the isotropic case results. The small systematic errors should result from the assumed neglection of birefringence (Section 3.4.1). Previous published works extracted the orientation ratio for this $Ir(ppy)_3$ emitter in a single emitter device, all at 8 wt.% emitter doping concentration, the results of which are presented in Table.5.3. All show a near isotropic emitter orientation ratio. All these values shown in Table 5.3 were for thermally evaporated devices as also with the devices of this work. Interestingly, for solution processed devices with an EML composed of 8% wt. $Ir(ppy)_3$ doped

into a CBP host Lampe et al. [154] reported a perpendicular preferred orientation ratio of $\|:\perp = 2:(1.18 \pm 0.02)$. This perpendicular preferred orientation cannot be explained.

Author	**Host material**	**Orientation ratio** $\|:\perp = \mathbf{2}:\boldsymbol{x}$
Liehm et al. [56]	CBP	(0.90 ± 0.06)
Lampe et al. [154]	CBP	(1.00 ± 0.02)
Kim et al. [49]	TCTA	(0.99 ± 0.02)
Murawski et al. [26]	TCTA:TPBi	(0.99 ± 0.09)

Table 5.3 Ir(ppy)$_3$ published orientation ratio results. *The x of the third column title represents the perpendicular orientation component with the given error.*

Different deposition conditions can cause a different orientation ratio, possibly due to a changed emitter environment. This same effect could cause the preferred perpendicular oriented green emitter ensemble in this work, due to the presence of the red emitters. Of course, more research needs to be done to clarify these effects.

5.4 Red emission zone profile

As the devices of this section have differing ETL thicknesses, for simulations to extract the red EZP, the average 3-layer EZP of the 124 nm and the 285 nm ETL devices will be assumed. The devices most sensitive to the red emitter EZP are those with ETL thicknesses of 124 nm, 165 nm and 325 nm. However, for the 124 nm ETL device, the interference minimum occurs more significantly for the green wavelength (Fig.5.1.2) so the interference minimum is dominated by green emitter emission. The interference minimum for this device is actually at λ =530 nm where green emission far outweighs red emission so this device is not very sensitive to the red emitter EZP, therefore red emitter EZP results for this device are not shown. Nevertheless, the extracted EZPs that will be shown from the 165 nm and 325 nm ETL devices also fit well for this device.

The device with the 165 nm ETL has a high red emitter contribution at the interference minimum and so a high red emitter AOP sensitivity. However, the

interference minimum occurs at λ =680 nm so there is a low absolute red intensity level and so the data has a very low SNR of ~7 (Fig.5.4.1).

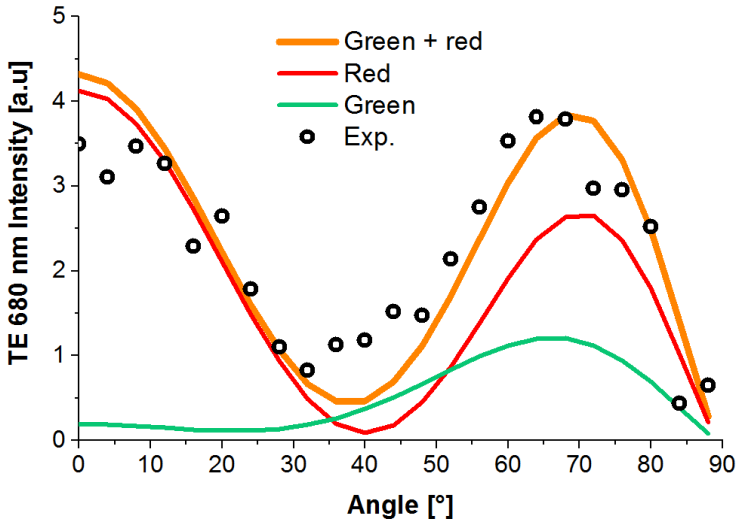

Fig.5.4.1 Interference minimum of the 165 nm ETL device. *Simulated emission is shown compared with the experimental data. The green line shows simulated emission from green emitters, the red line from red emitters and the orange line the sum of both. Black circles show the experimental data. The best fitting single point EZP was used to simulate the red emission. The interference minimum occurs at ~ 680 nm. A very low SNR of ~7 is observed.*

Since the interference minimum wavelength has a very high red contribution, data at 50 mAcm^{-2} was measured to give a higher SNR which allows for AOP extraction to a higher degree of accuracy. However, it should be noted that the EZP and hence the angular shape at the interference minimum could change with the increased current. The scaled data of both current densities is shown in Fig.5.4.2. From observing the data, it can be assumed that the EZP does not change qualitatively with the higher current. Such a current density comparison was also performed for the devices sensitive to the green EZP and no significant change in the emission pattern was observed.

Next, the EZP is extracted from the 165 nm ETL device using 50 mAcm^{-2} data, the results of which are shown in Fig.5.4.3. The λ =680 nm cross section is shown as it shows the sensitive interference minimum optimally. A wavelength fitting range of λ= 630 nm…690 nm was used as it covers the EZP sensitive region always with a much higher red than green contribution. The simulation uses an

estimated reduced q =0.6, to compensate for the higher current density. The experimental noise level for the red wavelength fitting range is higher at 0.5.

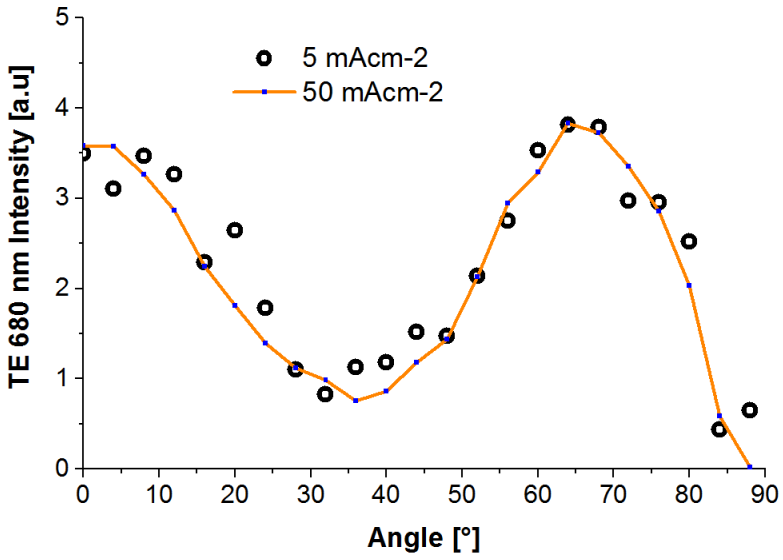

Fig.5.4.2. Interference minimum from 165 nm device at different current densities. *A scaled comparison of the TE 680 nm measured emission data is shown. 5 mAcm^{-2} data is shown by black circles and 50mAcm^{-2}data by blue squares. 50 mAcm^{-2} data is scaled by factor of 0.385 to compare the angular shapes. The best fitting single point EZP was used to simulate the red emitter emission.*

The fundamental EZPs which give information on basic EZP details such as the centre, width and cathode/anode side bias are shown in Fig.5.4.3(a). The single point result shows a slightly cathode sided EZP. The best fit of the point by point fit pushed all emission to the EML sides. The simulated spectrum of such an EZP fits the experimental data close to the experimental error with RMS_{rel} =1.2. (Fig.5.4.3(b)), but again does not agree with an emitter diffusion hypothesis. More likely, it suggests a slightly extended EZP. The constant and single point EZP simulation fit with high RMS_{rel} =3.1 and RMS_{rel} =1.9 respectively. In Fig.5.4.3(c) possible extended EZPs are shown. In Fig.5.4.3(d) it can be observed that the simulations using the EBL and red EML EZP when fitted give a RMS_{rel} =1.9. The simulated spectra of the red and green EML EZP and the three-layer extended EZP fit within in the experimental error with RMS_{rel} =0.9 and RMS_{rel} =0.8 respectively. This two-layer EZP is not inconceivable but it is difficult to physically explain.

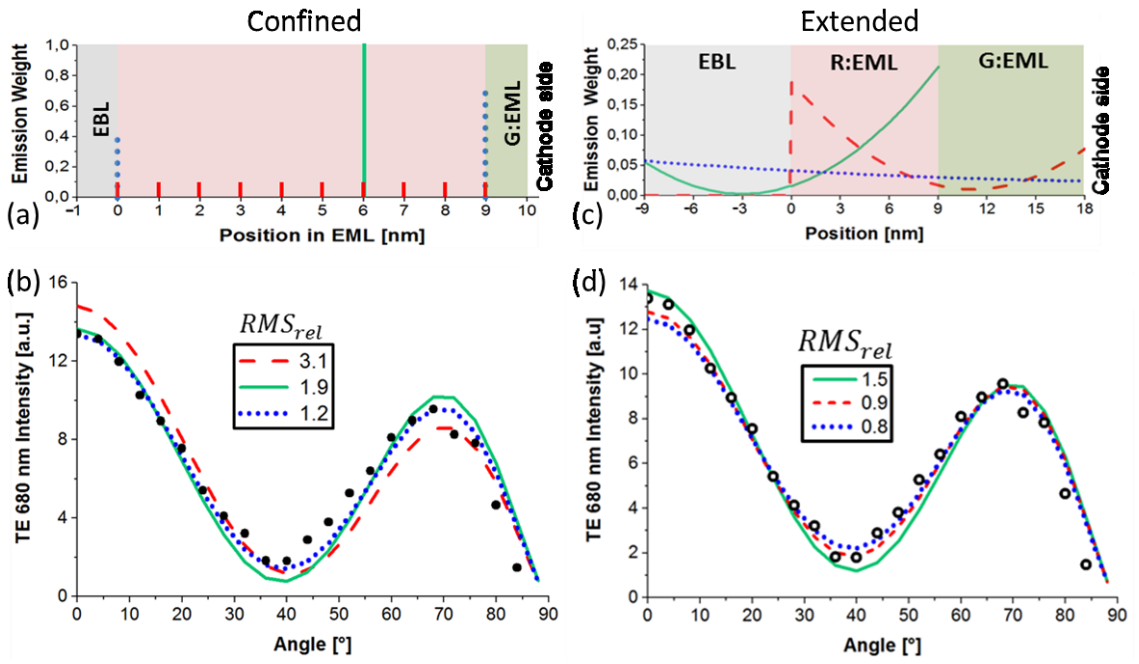

Fig.5.4.3. Red EZP extraction for the 165 nm ETL device at 50 mAcm^{-2} *(a) Shows fundamental confined EZPs. The red lines show a constant EZP, the best fitting point-by-point fit is shown by blue dotted lines and the best fitting single emission point is shown by the green line. (b) Shows the resulting simulated angular intensity patterns using these EZPs and experimental data (black circles) for 680nm TE emission. In part (c) the red dashed line shows an EF sum solution in the red EML and the green EML, the green solid line shows a red EML and EBL EF sum solution and the blue dotted line shows an EF sum solution of the three layers. (d) Shows the resulting simulated angular intensity patterns using these extended EZPs and experimental data (black circles) for 680 nm TE emission.*

Again where emission is pushed to the edges should indicate an extended EZP. The three layer EZP fits within the experimental error and can be explained, as before by emitter diffusion. The 3 layer EZP is anode sided although the single point result is cathode sided. However, the differences between slightly cathode sided and slightly anode sided are around the order of RMS_{rel} =0.1 and so a central, slightly extended EZP is concluded.

Differences in the RMS_{rel} values for errors appearing of similar magnitude in Fig.5.2.3 can be explained by the fact that the calculated RMS_{rel} depends not only on the noise level, but also the absolute signal level (Section 3.4.3(ii)).

A simulated versus experimental angular spectra comparison is shown over the green and red emitter emission range for confined and extended EZPs in

Fig.5.4.5. The difference between the confined EZP and extended EZP simulation fits can be observed at the interference minimum centred at λ ~625 nm and θ_A =65°. It can be seen that the extended EZP fits to the experimental data much better.

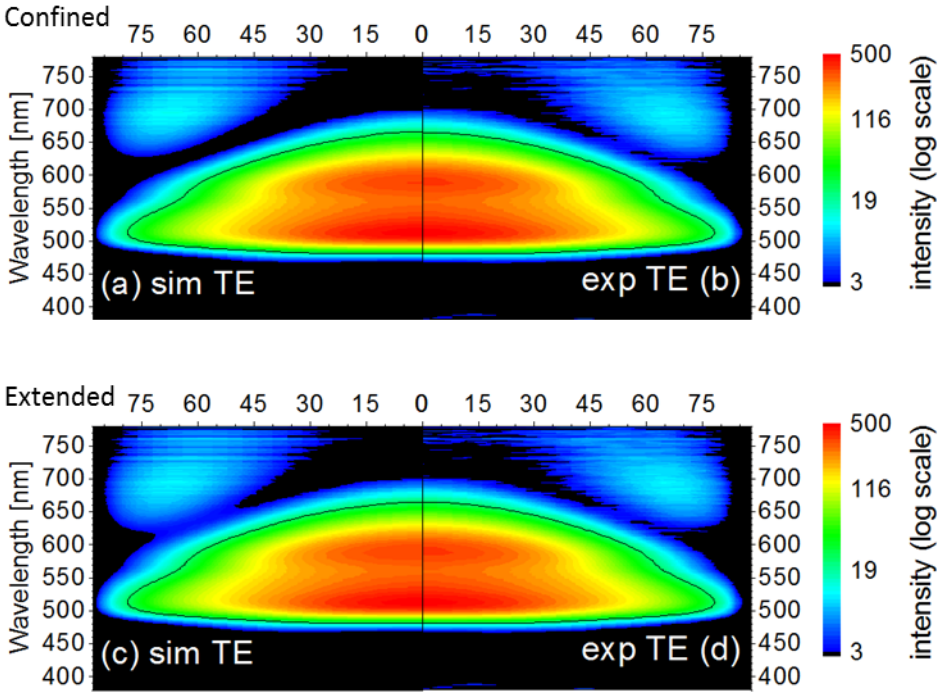

Fig.5.4.5 165 nm ETL device complete angular spectra comparison at 50 mAcm-². *The interference minima in the confined EZP simulated angular spectrum (a) is too low compared to the experimental data. The experimental spectrum is shown for comparison in (b) and (d). In the extended EZP angular spectrum simulation (c) a better interference minimum (centred at around λ =625 nm and θ =65°) fit results. The black contour line shows an intensity value of 20 as a viewing aid. All diagrams have the same intensity scale. Best fitting EZPs were used for the simulations.*

The green PL spectrum was assumed as the green intrinsic spectrum for this analysis part, however, simulation errors due to the green intrinsic spectrum assumption have not been included in the RMS_{rel} in this section. Instead, the effect of changing the magnitude of this assumed spectrum by 10% will be analysed. The change of 10% is assumed to be sensible from the data fitting shown in Fig. 5.1.1. From 572 nm to 600 nm the percentage fitting error of the extracted combined spectrum and the sum of the assumed individual emitter intrinsic spectra is <1%, rising to 2% at 654 nm, to 3% at 670 nm and 5% at 700 nm. Wavelengths above

700 nm with high error due to a low SNR will not be used in any fitting processes. When the intensity of this green spectrum is increased or decreased by 10%, the best fitting extracted red EZP does not change, but the RMS_{rel} increases from 0.8 to ~ 1.1. The red EZP also depends on the assumed green EZP. When each individual green device extracted EZP is set in the simulation there is a small shift of the red EZP in position. For example, when the more cathode- sided green EZP of the 124 nm ETL device is set, the red EZP is slightly shifted to the anode side to compensate for the shifted emission. However, the red EZP result is qualitatively the same and the RMS_{rel} does not change within one decimal place.

Next, the EZP is extracted from the 325 nm ETL device. It should be noted that this device is not as sensitive to the EZP as the 165 nm ETL device (Fig.5.1.2(a)). The λ =610 nm cross section is shown as it shows the sensitive interference minimum optimally. In Fig.5.4.6 it can be observed that data at 5 mAcm^{-2} shows a better SNR~100 than the 165 nm ETL device as the interference minimum occurs at a lower wavelength where the red intrinsic spectrum has a higher absolute value.

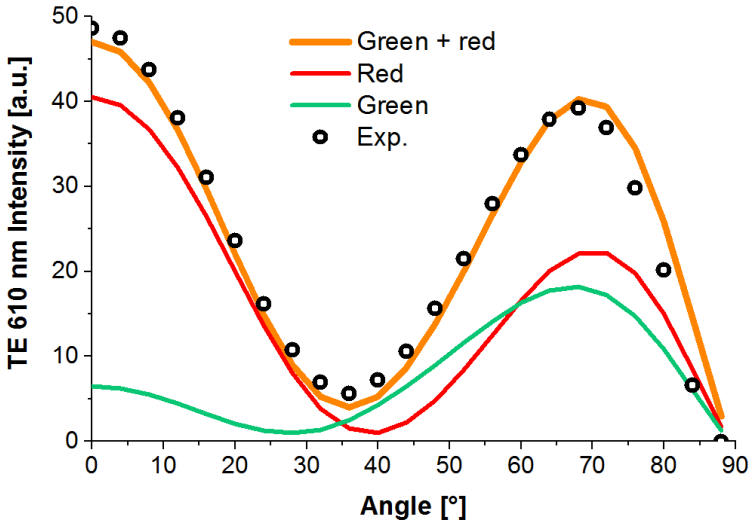

Fig.5.4.6 Interference minimum of the 325 nm ETL device at 5 mAcm^{-2}. *Simulated emission is shown compared with the experimental data. The green line shows simulated emission from green emitters, the red line from red emitters and the orange line the sum of both. Black circles show the experimental data. The EZP for the red simulation was the best fitting single point emission. The interference minimum occurs at λ ~610 nm. A much higher SNR of ~ 100 compared to the 165 nm device at the same current is observed.*

This device has a quite high red contribution relative to green at the interference minimum and so a quite high red AOP sensitivity.

The confined and extended EZP extraction of the 325 nm ETL device is shown using 5 $mAcm^{-2}$ data in Fig.5.4.7. A fitting range from λ =580 nm…650 nm covers the EZP sensitive region, here for every wavelength a higher red than green contribution is observed. The fundamental EZPs which give information on basic EZP details such as the centre position, width and cathode/anode side bias are shown in Fig.5.4.7(a). The single point result shows an anode sided EZP.

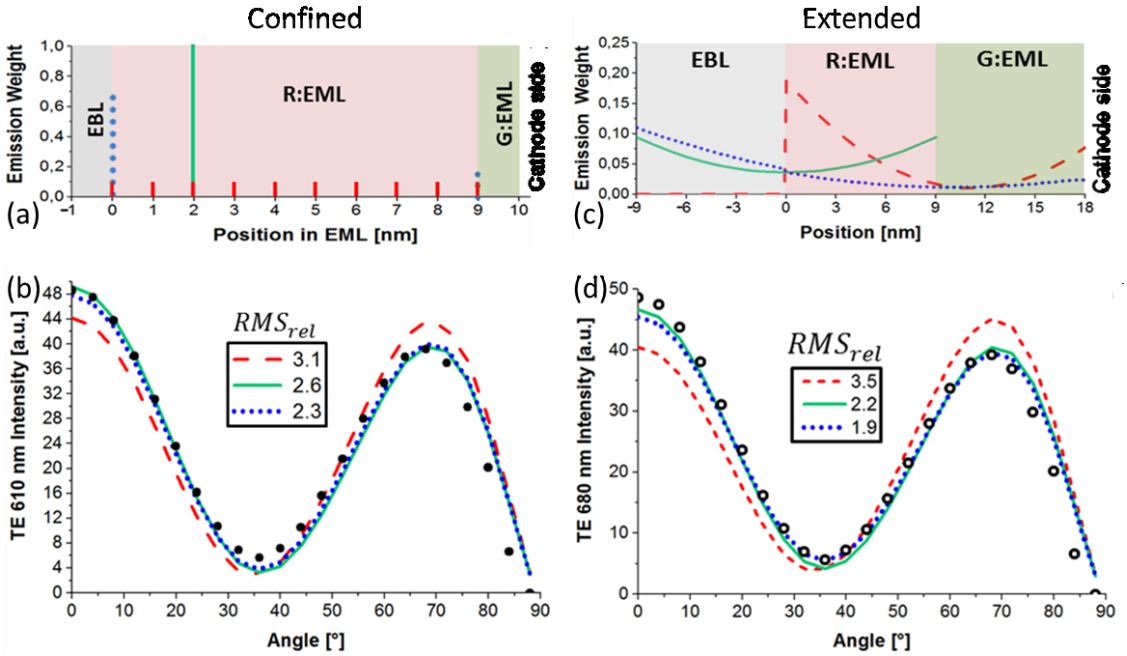

Fig.5.4.7 Red EZP extraction for the 325 nm ETL device at 5 $mAcm^{-2}$ *(a) Shows fundamental confined EZPs. The red lines show a constant EZP, the best fitting point-by-point fit is shown by blue dotted lines and the best fitting single emission point is shown by the green line. (b) Shows the resulting simulated angular intensity patterns using these EZPs and experimental data (black circles) for λ =610nm TE emission. In part (c) the green solid line shows a EF sum solution in the red EML and the EBL, the red dashed line shows a red EML and green EML sum solution and the blue dotted line shows an EF sum solution of the three layers. (d) Shows the resulting simulated angular intensity patterns using these extended EZPs and experimental data (black circles) for λ =610 nm TE emission.*

The best angular point by point fit also pushed most emission to the anode side. The simulated spectrum of such an EZP fits badly with RMS_{rel} =2.3 (Fig.5.4.7(b)). The constant and single point EZP simulation also fit with high

RMS_{rel} =3.1 and RMS_{rel} =2.6 respectively. In Fig.5.4.7(d) no extended EZP simulation fits the data within the experimental error, but the anode-sided 3-layer EZP fits the data closest to the experimental error with RMS_{rel} =1.9. The fitting problem is that a higher simulated intensity at θ_A=0° is needed for a better fit. To do this, the EZP needs to be shifted to the anode side, which is not possible in this 3 layer assumption analysis. So this result could indicate possible emission from the HTL. The RMS_{rel} is not reduced with a $\pm$ 1 nm variation of the ETL thickness. When changing the magnitude of the green PL spectrum by up to 10%, the EZP extracted does not qualitatively change but a reduced best RMS_{rel} of 1.7 can be reached. Again when changing the green EZP to the one extracted from the device with the 124 nm ETL or the device with the 250 nm ETL, the result is qualitatively the same and the RMS_{rel} does not change.

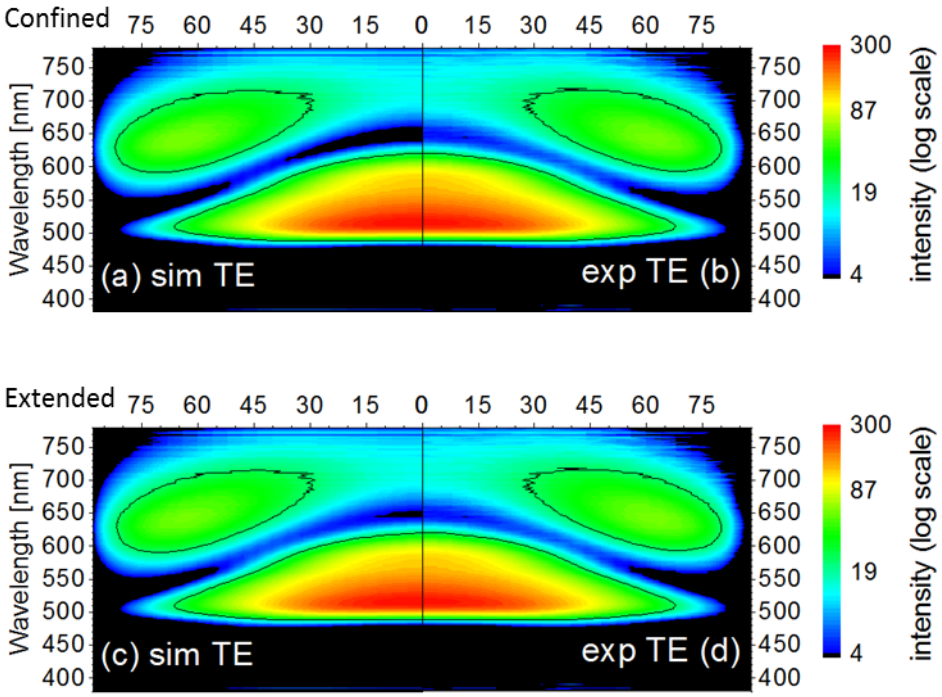

Fig.5.4.8. 325 nm ETL device full angular spectra comparison at 5 mAcm^{-2}. *The interference minima in the confined EZP simulated angular spectrum (a) is too low. The experimental spectrum is shown (b) and (d). In the extended EZP angular spectrum simulation (c) a better interference minimum (centred at around 600 nm and 30°) fit results. The black contour line shows an intensity value of 20 as a viewing aid. Both diagrams have the same intensity scale. Best fitting EZPs were used for the simulations.*

A simulated versus experimental angular spectra comparison is shown over the green and red emitter emission range for confined and extended EZPs in Fig.5.4.8. The difference between the confined EZP and extended EZP simulation fits can be observed at the interference minimum centred at λ ~600 nm and θ_A =30°. It can be seen that the extended EZP fits to the experimental data only slightly better.

When dealing with emission from different positions in the device, it should be noted that the emitter lifetime is not constant as can be observed in Fig.5.4.4. The lifetime for the red emitters can be simulated in all three layers as there is no absorption at the red average emission wavelength of λ = 630 nm. Förster transfer from red emitters to the HTL is possible as it absorbs in the red emitter intrinsic spectrum. As mentioned previously, an accurate measure of the emitter q is important where extended emission zones are evident. The simulated lifetime of parallel and perpendicular orientated emitters are slightly different because of different microcavity interference conditions for each emitter (Section 2.3).

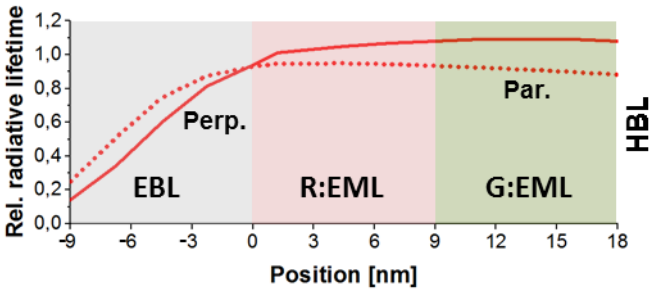

Fig.5.4.4. Red emitter lifetime change with position. *Parallel-oriented emitter lifetimes (dotted line) and perpendicular-oriented emitter lifetimes (solid line) are shown versus position. The simulation is for the 165 nm ETL device with q=0.7 for λ =630 nm radiation. The lifetime does not change significantly for devices with differing ETLs.*

In this case an extension of the EZP into the EBL would significantly reduce the emitter lifetime and hence intrinsic quantum efficiency.

Using the best fitting 3-layer extended extracted EZPs for each device, the extracted red intrinsic spectra are shown in Fig.5.4.9 compared to the red EL spectrum from section 4.2. The 165 nm ETL device intrinsic spectrum is extracted from data measured at 5 mAcm^{-2}, whilst the 325 nm ETL device intrinsic spectrum is extracted from data measured at 50 mAcm^{-2}.

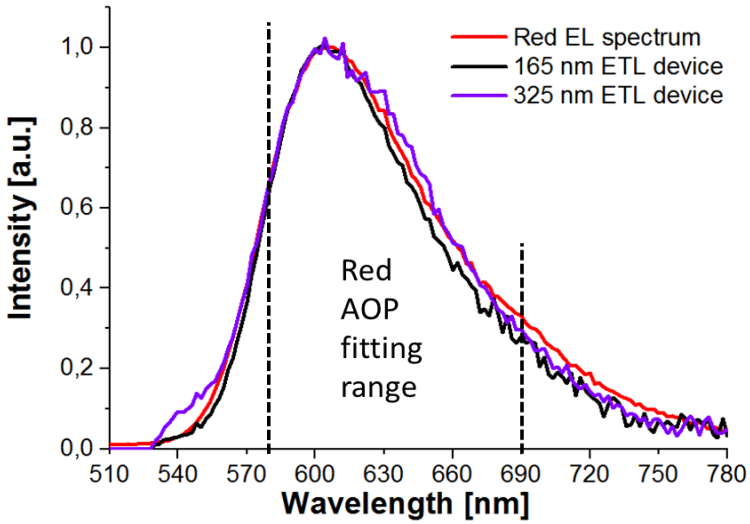

Fig.5.4.9. Comparison of extracted intrinsic red spectra to red EL spectrum. *The extracted intrinsic spectra from the two devices are compared with the red EL spectrum extracted in Section 4.2 (red line). The intrinsic red spectrum extracted from the 165 nm ETL device is shown as a black line and the 325 nm ETL devices a blue line. Vertical dashed black lines indicate the red AOP fitting range of this section.*

The maximum used AOP fitting range incorporating both red AOP sensitive devices in this section is from λ =580…690 nm. The assumption of using the single emitter device intrinsic green spectrum results in a red intrinsic spectrum close to the single emitter device red EL spectrum. The percentage error difference between the EL and the extracted spectrum is never more than 10% over the red AOP fitting range. This indicates that the intrinsic spectra of the emitters in a dual-emitter device does not change significantly compared to the single emitter device case. The significant discrepancy in the 325 nm ETL device spectrum at λ =545 nm is due to the same discrepancy as the one in Fig.5.1.1. However this is not within the fitting range. The differences between the two device extracted spectra could be due to the different current densities of the experimental data used. A slightly extended, anode-sided red emitter EZP is concluded from these results. Recombination should occur at the interface of the red and green EMLs, which is not indicated by the results here.

5.5 Red orientation ratio

For the simulations of this section, a green orientation ratio of ||:⊥=2:1.20 and again the average 3-layer EZP of the 124 nm and the 285 nm ETL devices found for the green emitters will be assumed. As illustrated in Fig.5.1.2, devices with a high

red perpendicular emission contribution are the devices with a 124 nm, a 165 nm and 325 nm ETL. The device with the 124 nm ETL also has a high green perpendicular contribution and so is not very sensitive to red orientation and so analysis of this device not shown. First, the orientation ratio is extracted from the 165 nm device, the results of which are shown in Fig.5.5.1. Data measured at 5 $mAcm^{-2}$ already has a high SNR of ~39 and is used for the extraction procedure. However, the EZP extracted from the 50 $mAcm^{-2}$ TE polarized data is set. The fitting range is from λ =620 nm…670 nm to show both comparable amounts of parallel and perpendicular emission and a high red to green emission ratio.

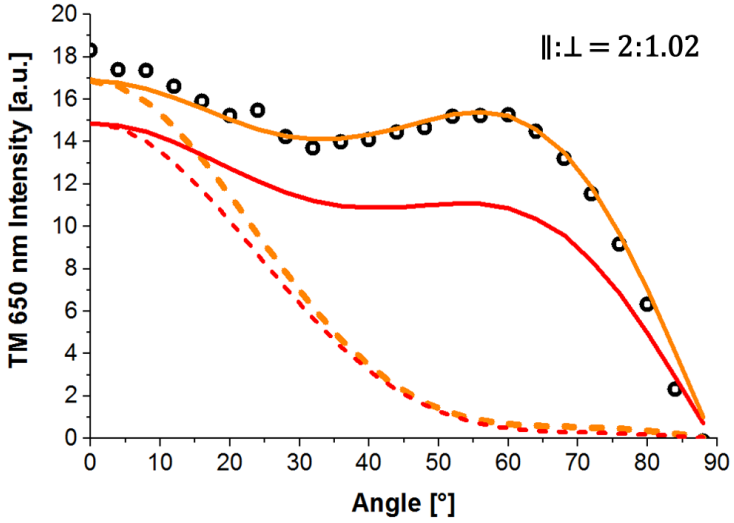

Fig.5.5.1. Orientation ratio fitting for the 165 nm ETL device. *Fitted simulated data is compared with the experimental. Simulated red emitter emission is in red. Red plus green simulated emission is shown in orange. Parallel emission contributions are shown as dashed lines. Parallel plus perpendicular or the total TM emission contributions are shown as solid lines. Experimental data points are shown as black circles. Emission for an illustrative TM wavelength of λ =650 nm is shown.*

The green TM emission contribution in this wavelength range is approximately a third of the red, for λ =650 nm this can be seen from the difference between orange and red curves in Fig 5.5.1. An almost isotropic orientation ratio of ‖:⊥=2:1.02 is extracted for the red emitter with q=0.70 and a green orientation ratio of 1:20. The RMS_{rel} of the fit is outside of the experimental error at 1.2. When RMS_{rel} is restricted to a maximum of 1.50, the orientation ratio varies as ‖:⊥ =2:0.87…2:1.18. When the red emitter q is changed in the simulation from 0 to 1

the EZP must be corrected and the orientation ratio changes by ‖:⊥ =(2:1.02±0.06).

Next, the orientation ratio for 325 nm device is extracted. The wavelength fitting range is λ =580 nm…650 nm to show both comparable amounts of parallel and perpendicular emission and a high red to green emission ratio. The green TM emission contribution in this wavelength range is higher than for the 165 nm device, but the red emission still dominates. For λ =610 nm this can be seen from the difference between orange and red curves in Fig 5.5.2.

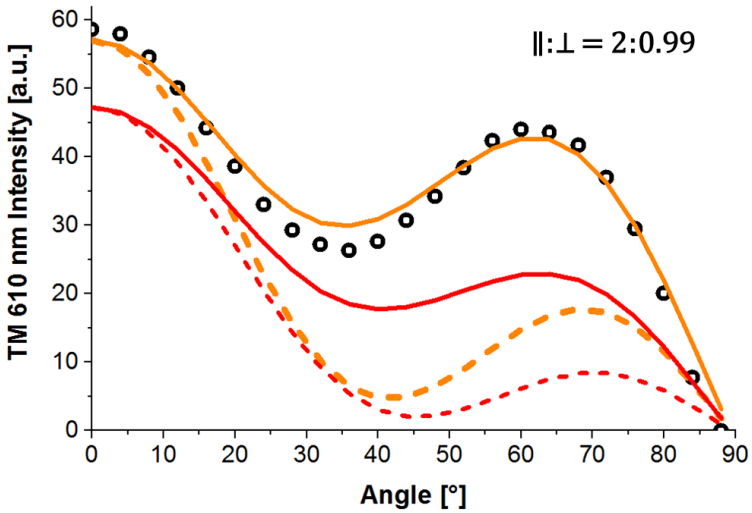

Fig.5.5.2 Orientation ratio fitting for the 325 nm ETL device. *Fitted simulated data is compared with the experimental. Simulated red emitter emission is in red. Red plus green simulated emission is shown in orange. Parallel emitter emission contributions are shown as dashed lines. Parallel plus perpendicular or the total TM emission contributions are shown as solid lines. Experimental data points are shown as black circles. Emission for an illustrative TM wavelength of 610 nm is shown.*

Again a near isotropic orientation ratio of ‖:⊥= 2:0.99 is extracted for a red emitter q=0.70 and a green orientation ratio of 1:20. The RMS_{rel} of the fit is slightly worse than for the 165 nm device at 1.4. The θ=0°:35° simulated emission ratio is too high. When the red emitter q is changed in the simulation from 0 to 1 the EZP must be corrected and the orientation ratio changes again by ‖:⊥ =(2:0.99±0.06).

The orientation ratios extracted here feature a higher perpendicular component than the single emitter device result for the same emitter and host of ‖:⊥=2:0.65. As discussed for the green emitter, the prescence of the other emitter

species diffused into each others EMLs could cause this difference in the ensemble orientation ratio. Perhaps anisotropic energy transfer occurs, in that, depending on the device ETL thickness, different lifetime changes of differently oriented emitters affects energy transfer rates.

This work showed a first attempt at extracting the individual AOP from a dual emitter device. The green emitter EZP and orientation ratio was extracted within the experimental error for two different devices. However, these results used the established single emitter approach. When using the novel separated spectra approach, only one of two devices enabled red emitter EZP extraction within the experimental error. Red emitter orientation ratios could not be extracted within the experimental error. Since AOP fitting outside of the experimental error occurs only for red emitter EZP and orientation ratios, the individual internal spectra assumptions should be at fault. In Fig.5.5.1 and Fig.5.5.2, systematic errors in the TM spectra are evident. These should be due to the presence of birefringence in the device layers. Further work in this area should measure such birefringence of the device layers to improve the simulation assumptions and fit the experimental data within the measurement error. Evidence for extended EZPs was found for red and green emitters, under low current density laboratory conditions, with fresh devices. For commercial, much-operated OLEDs this effect could become stronger, if the extension is due to emitter diffusion, which increases with heating (Section 4.1.2). Emitter lifetimes have been simulated with varying position in the device and observed to change significantly when present close to absorbing layers. This effect could be very important in analyzing the orientation ratio and intrinsic quantum efficiency of devices where a significant amount of emitters have diffused over distances of ~5 nm.

6. CONCLUSIONS AND OUTLOOK

In this work, small molecule emitter bottom-emitting OLEDs featuring only the commonly used OLED red phosphor $Ir(MDQ)_2(acac)$ and dual-emitter devices featuring this emitter and the green $Ir(ppy)_3$ emitter have been analyzed. The device active optical properties such as the emission zone profile (EZP) and the emitter orientation ratio (of parallel to perpendicular emission components) are critical towards determining the device performance. Procedures to extract information on these properties in single emitter devices by comparing simulated angular spectra with the experimental spectra has been previously established [63].

(1) The first goal of this work was to adapt the established microcavity inverse light outcoupling approach of extracting the device EZP to investigate if there is light emission from other layers as well as the emission layer.

An established EZP extraction method was improved upon to investigate if emission originated from outside of the emission layer. A cathode-sided emission result agrees with the literature. However experimental findings could not be explained by light emission originating strictly from the emission layer. A widening of the EZP into the blocking layers (which confine charges to the emission layer) yields a simulation result that fits the experimental data within the measurement error. For a state-of-the-art OLED with blocking layers, emission from outside the emission layer has not been considered before in the literature. Diffusion of the emitter molecules outside of the EML is given as a hypothesis for this extended, multi-layer EZP. A more precise investigation of the EZP would be enabled by the methods developed in this work. When the orientation ratio was extracted using the established method, it agreed with previously published parallel preferred orientation distributions. However the effect of an extended EZP on the ratio extracted was significant even though this ratio still agreed with comparable published results. Every measured orientation ratio in the literature assumes emission layer-confined emission. The results of this work could allow for more accurate measurements of device orientation ratios.

(2) The second goal of this work was to use specialised devices to measure both parallel and perpendicular emitter lifetimes which could give information on the detailed emitter orientation distribution, rather than just the orientation ratio.

Specialised devices with a thin metal interlayer placed near the emitters allowed the observation of a high lifetime orientation splitting and also a high perpendicular emitter emission. This results in a pronounced increase of the decay rate of perpendicularly oriented emitters due to energy transfer into the surface plasmon at the interlayer. For these devices, the parallel and perpendicular emitter emission lifetimes were measured under different observation angles and polarizations. Photoluminescence lifetime measurements were performed in addition to electroluminescence measurements to make use of an increased intrinsic quantum efficiency and thus increase the orientational lifetime splitting. This measurement was combined with the orientation ratio resulting from the established analysis method in order to extract more details of the emitter orientation distribution of the emitters. Despite this orientation selective quenching, when observing mostly parallel or perpendicular emitters at different angles and polarizations, no expected emission rate difference was observed. From such an observation either a wide emitter orientation distribution featuring a fluctuating ensemble average or a well-oriented narrow distribution exhibiting a static orientation ensemble average can be deduced. Due to other work showing that the emission transition dipole moments of the excited triplet states of $Ir(MDQ)_2(acac)$ are highly overlapping [53], giving practically one possible orientation, a well aligned, narrow emitter orientation distribution was concluded. Experimental errors of the lifetime measurement indicate the upper limit of such a normal distribution standard deviation to be 17°. That is to say that ~68% of the emitters have an orientation within +/- 17° of the "average" orientation representing the orientation ratio. This surprisingly narrow distribution is comparable to those of well-ordered Langmuir-Blodgett films.

Currently, emitter orientation analysis and optimization are based upon the knowledge of the orientation distributions' second moments. The detailed form of the emitter orientation distribution is not observable in the standard

approaches, meaning that qualitatively different orientation distribution models which potentially lead to different orientation optimization strategies, cannot be compared. Additionally, the interpretation of OLED orientation distribution measurements depends on the averaging of all the orientations in the real emitter ensemble. Such effects will become more pronounced when introducing lateral structures in an OLED, e.g. in the case of a grating or scattering based outcoupling enhancement. The results of this work show a new level of ensemble orientation detail, i.e. the width of the emitter orientation distribution can be accessible.

During photoluminescence measurements, the emission observed was unexpectedly practically independent of the excitation polarization. A difference in the orientation of the absorption dipole and the emission dipole was given as the most likely cause of this observation.

(3) The third goal of this work was to extend the established single emitter device emitter property extraction methods to dual emitter devices.

As a novel adaptation of the active optical property extraction method, the EZP and orientation ratio were extracted for each individual emitter in a dual emitter OLED device. Dual emitter active property extraction involves a separation of overlapping emission from two dyes. An assumption of the intrinsic emission spectra was made and analysed for suitability. The results for the red and green EZPs in the dual emitter devices indicate a lesser extension than for the red single emitter devices. The experimental emission pattern of the single red emitter devices were measured 12 months after manufacture but the spectra of the dual emitter devices were measured 4 months after manufacture. This would agree with the emitter diffusion hypothesis.

The orientation ratios of each emitter in a dual emitter device were extracted. An isotropic red emitter orientation ratio was extracted compared to a parallel preferred ratio for the single emitter case. A more perpendicular orientation ratio was extracted for the green emitter compared to the isotropic published values for single emitter devices. These different orientation ratio results could be due to the fact that an effective ratio is extracted from emitters in multiple different material layers. The orientation ratio is known to vary with host material. These differences should also be caused to some degree by inter-emitter energy transfer from the green to the red emitter, as the extended EZP results

denote the presence of red emitters in the green emission layer and vice versa. Whereas EZP extraction only uses emission from parallel oriented emitters, the orientation ratio extraction intrinsically uses emission from perpendicular emitters also. Energy transfer should affect the intrinsic quantum efficiency of parallel or perpendicular emitters differently. Modern lighting and displays predominantly feature multi emitter OLED devices. It is of utmost interest to be able to extract individual emitter active optical properties from such devices, as the assumption of single emitter behaviour should not be reliable. This works shows successful single emitter optical property extraction results for the first time.

This work suggests a route to obtain further information about the photo-physical processes and emitter properties from analysis of OLED emission from specialized devices. The first evidence for significant emission from blocking layer(s) presented should be of interest to all in the OLED field. Further experiments are necessary to prove the hypothesis that emitters are present in the blocking layers. The simplest test would be to manufacture an OLED with as thin an emission layer as possible and measure the EZP with time/operation. The proposed method of emission lifetime analysis in plasmonic Purcell modified OLED stacks indicates a route to better understand the emitting material morphology, to tailor the emitter orientation and to significantly improve OLED external efficiency. The surprising single emitter device emitter orientation results of this dissertation gives new insights into emission processes of a common OLED emitter which should stimulate renewed research in this area. This approach should also be relevant to next generation thermally activated delayed fluorescence emitters. High speed transient resolution absorption measurements could further clarify photoluminescence processes. The quite narrow emitter orientation distribution interpretation could be independently verified by electron spin resonance spectroscopy. The emitter orientation measurement methods developed in this work could also be interesting in the fields of, organic lasers and organic photovoltaics. This work shows how to successfully adapt the standard optical property extraction processes for single emitter devices for use with multi-emitter

devices. Experimental measures giving the quadratic functional shape of a red and a green emitter ensemble in a single device have been shown. The effect of energy transfer on the orientation ratio should be further investigated to enable reliable measures of the individual emitter orientation distribution in multi-emitter OLEDs. However, this work should encourage a serious advancement in the knowledge of emitter properties in multi-emitter devices.

BIBLIOGRAPHY

[1] S. Ho, S. Liu, Y. Chen, F. So, “Review of recent progress in multilayer solution-processed organic light-emitting diodes”, Special Section on Solid-State Lighting: Photonics and Technologies, J. Photon. Energy. 5(1), 057611 (2015).

[2] “LG’s new Signature OLED TV is only 2.5 millimeters thick” (05.01.2016). Retrieved from http://bgr.com/2016/01/05/ces-2016-lg-signature-oled-tv-4k/

[3] “Lomox Getting Closer to Bringing Us Glowing Wallpaper” (30.12.2009). Retrieved from http://www.treehugger.com/clean-technology/lomox-getting-closer-to-bringing-us-glowing-wallpaper.html

[4] “Samsung's latest OLED can be a mirror, a window or a TV” (11.06.2015). Retrieved from http://www.techradar.com/news/television/samsung-s-latest-oled-screen-can-be-a-mirror-a-window-or-a-tv-1296418

[5] “Watch Samsung’s rollable OLED smartphone display unfold before your eyes” (25.05.2016). Retrieved from http://bgr.com/2016/05/25/samsung-galaxy-x-foldable-smartphone/

[6] “LG finally showed us the roll-up TV it’s been teasing for years” (09.01.2016). Retrieved from http://www.digitaltrends.com/home-theater/lg-rollable-oled-hands-on-video/

[7] “LG E6 OLED Review” (20.05.2016). Retrieved from http://referencehometheater.com/review/lg-e6-oled-review/

[8] “LG OLED55E6 4K HDR OLED TV Review” (27.04.2016). Retrieved from http://www.hdtvtest.co.uk/news/oled55e6-201604274285.htm

[9] “Our Test Results Televisions” (29.07.2015). Retrieved from http://www.rtings.com/tv/tests/scores

[10] “LG OLED65E6P 4K OLED TV Review” (20.05.2016). Retrieved from http://televisions.reviewed.com/content/lg-oled65e6p-4k-oled-tv-review

[11] “Galaxy Note7 OLED Display Technology Shoot-Out” (2016). Retrieved from http://www.displaymate.com/Galaxy_Note7_ShootOut_1.htm

[12] Jwo-Huei Jou, et al. “Sunlight-style color-temperature tunable organic light-emitting diode” Applied Physics Letters 95, 013307 (2009).

[13] “LED light bulbs keep improving in efficiency and quality” (04.11.2014). Retrieved from http://www.eia.gov/todayinenergy/detail.php?id=18671

[14] “LG Chem to soon release 100 lm/W OLED lighting panels” (12.09.2014). Retrieved from http://www.oled-info.com/lg-chem-soon-release-100-lmw-oled-lighting-panels

[15] “Konica Minolta developed the world's most efficient OLED panel at 131 lm/W” (04.03.2014). Retrieved from http://www.oled-info.com/konica-minolta-developed-worlds-most-efficient-oled-panel-131-lmw

[16] “Konica Minolta achieves 131 lm/W white OLED lighting panel” (04.03.2014). Retrieved from http://www.osadirect.com/news/article/1178/konica-minolta-achieves-131-lmw-white-oled-lighting-panel/

[17] C. W. Tang, S. A. Van Slyke, and C. H. Chen, “Electroluminescence of doped organic thin films”, J. Appl. Phys. 65, 3610 (1989).

[18] E. Aminaka, T. Tsutsui, and S. Saito, “Effect of layered structures on the location of emissive regions in organic electroluminescent devices”, J. Appl. Phys. 79, 8808 (1996).

[19] J. Wünsche, S. Reineke, B. Lüssem, and K. Leo, „Measurement of triplet exciton diffusion in organic light-emitting diodes”, Phys. Rev. B 81, 245201 (2010).

[20] D. Song, Q. Wang, S. Zhao, and H. Aziz, “Dependence of carrier recombination mechanism on the thickness of the emission layer in green phosphorescent organic light emitting devices”, Org. Electron. 12, 582 (2011).

[21] R. Coehoorn, H. van Eersel, P. Bobbert, and R. Janssen, “Kinetic Monte Carlo Study of the Sensitivity of OLED Efficiency and Lifetime to Materials Parameters”, Adv. Func. Mater. 25, 2024 (2015).

[22] M. Mesta, M. Carvelli, R. J. de Vries, H. van Eersel, J. J. M. van der Holst, M. Schober, M. Furno, B. Lüssem, K. Leo, P. Loebl, R. Coehoorn, and P. A. Bobbert, “Molecular-scale simulation of electroluminescence in a multilayer white organic light-emitting diode”, Nature Materials 12, 652 (2013).

[23] G. Y. Zhong, Y. Q. Zhang, and X. A. Cao, “Quenching-enhanced shift of recombination zone in phosphorescent organic light-emitting diodes”, Org. Electron. 11, 1338 (2010).

[24] C. Diez, T. C. G. Reusch, S. Seidel, and W. Brütting, “Investigation of energy transfer mechanisms between two adjacent phosphorescent emission layers”, J. Appl. Phys. 111, 113102 (2012).

[25] R. Meerheim, S. Scholz, S. Olthof, G. Schwartz, S. Reineke, K. Walzer, K. Leo, “Influence of charge balance and exciton distribution on efficiency and lifetime of phosphorescent organic light-emitting devices”, J. Appl. Phys. 104, 014510 (2008)

[26] C. Murawski, P. Liehm, K. Leo, M. C. Gather, “Influence of Cavity Thickness and Emitter Orientation on the Efficiency Roll-Off of Phosphorescent Organic Light-Emitting Diodes”, Adv. Func. Mater. 24, 1117-1124 (2014).

[27] S. Wehrmeister, L. Jäger, T. Wehlus, A. F. Rausch, T. C. G. Reusch, T. D. Schmidt, and W. Brütting, “Combined electrical and optical analysis of the efficiency roll-off in phosphorescent organic light-emitting diodes”, Phys. Rev. Applied 3, 024008 (2015).

[28] C. Murawski, Efficiency Roll-Off in Organic Light-Emitting Diodes, PhD thesis, Technische Universität Dresden, 2015.

[29] N.C. Erickson, R J. Holmes, “Engineering Efficiency Roll-Off in Organic Light-Emitting Devices”, Volume 24, Issue 38, , Pages 6074–6080, (2014).

[30] S. Lee, C. W. Tang, L. J. Rothberg, “Effects of mixed host spatial distribution on the efficiency of blue phosphorescent organic light-emitting diodes”, Appl. Phys. Lett. 101, 043303 (2012).

[31] H. van Eersel, P. A. Bobbert, R. A. J. Janssen, and R. Coehoorn, “Monte Carlo study of efficiency roll-off of phosphorescent organic light-emitting diodes: Evidence for dominant role of triplet-polaron quenching”, Applied Physics Letters 105, 143303 (2014).

[32] B. Mazhari, “Impact of interfacial barriers on recombination profile in bilayer organic light-emitting diode”, Organic Electronics 6, 229–236, (2005).

[33] R. Coehoorn and S. L. M. van Mensfoort, “Effects of disorder on the current density and recombination profile in organic light-emitting diodes”, Physical Review B 80, 085302, (2009).

[34] B. Peruccoa, N.A. Reinke, F. Müller, D. Rezzonico, and B. Ruhstaller, “The influence of the optical environment on the shape of the emission profile and

methods of its determination", Organic Photonics IV, Proc. of SPIE, Vol. 7722, 77220F, (2010).

[35] K. Kim, T. Won, "Exciton Dynamics in Organic Light-emitting diodes", Journal of the Korean Physical Society, Vol. 61, No. 9, pp. 1523-1527, (2012).

[36] C. Lia, T. Tsuboib, W.Huang, "Recombination zone in organic light emitting diodes with emitting layer of diphenylanthracene-derivative host", 9th International Conference on Nano-Molecular Electronics, Physics Procedia 14, 213–216, (2011).

[37] B. Ruhstaller, T. Beierlein, H. Riel, S. Karg, J. C. Scott, W. Riess, „Simulating Electronic and Optical Processes in Multilayer Organic Light-Emitting Devices", IEEE Journal of selected topics in Quantum Electronics, Vol. 9, No. 3, (2003).

[38] Y. Kajiyama, K. Kajiyama, and H. Aziz, "Diffusion barriers for achieving controlled concentrations of luminescent dopants via diffusion for mask-less RGB color patterning of organic light emitting devices" Optics Express Vol. 23, Issue 24, pp. 30783-30792 (2015)

[39] T. Sadek, H. Aziz, R. O. Loutfy, P. M Smith, "Poor confinement of e-h recombination zone in blue OLEDs", IEEE CCECE/CCGEI, Niagara Falls, Canada (2008).

[40] M. Flämmich, D. Michaelis, N. Danz, „Accessing OLED emitter properties by radiation pattern analyses", Organic Electronics 12, 83–91,(2011).

[41] S. L. M. van Mensfoort, M. Carvelli, M. Megens, D. Wehenkel, M. Bartyzel, H. Greiner, R. A. J. Janssen, R. Coehoorn, „Measuring the light emission profile in organic light-emitting diodes with nanometre spatial resolution", Nature Photonics 4, 329 - 335 (2010).

[42] N. Danz, R. Mac Ciarnain, D. Michaelis, T. Wehlus, A. F. Rausch, C. A. Wächter, T. C. G. Reusch, „OLED emission zone measurement with high accuracy", Proc. SPIE 8829, Organic Light Emitting Materials and Devices XVII, 882923 (2013).

[43] M. Fujihira, Lee-Mi Do, A. Koike, "Growth of dark spots by interdiffusion across organic layers in organic electroluminescent devices", Appl. Phys. Lett. 68, 1787, (1996).

[44] V. Bulovic, V. B. Khalfin, G. Gu, P. E. Burrows, D. Z. Garbuzov, and S. R. Forrest, "Weak microcavity effects in organic light-emitting devices", Phys. Rev. B 58, 3730 (1998).

[45] S. Nowy, B.C. Krummacher, J. Frischeisen, N.A. Reinke, W. Brütting, "Light extraction and optical loss mechanisms in organic light emitting diodes: influence of the emitter quantum efficiency", J. Appl. Phys. 104, 123109 (2008).

[46] H. Cho, D. Kim, and H. Lee "Optical outcoupling enhancement in organic light-emitting diodes using a gradually varying refractive index dielectric structure", Japanese Journal of Applied Physics 54, 062101 (2015).

[47] M. Flämmich, J. Frischeisen, D. S. Setz, D. Michaelis, B. C. Krummacher, T. D. Schmidt, W. Brütting, N. Danz, "Oriented phosphorescent emitters boost OLED efficiency", Org. Electron. 12, 1663-1668 (2011).

[48] M. C. Gather and S. Reineke, "Recent advances in light outcoupling from white organic light-emitting diodes", J. Photon. Energy 5, 057607 (2015).

[49] S.-Y. Kim, W.-I. Jeong, C. Mayr, Y.-S. Park, K.-H. Kim, J.-H. Lee, C.-K. Moon, W. Brütting, J.-J. Kim, "Organic Light-Emitting Diodes with 30% External Quantum Efficiency Based on a Horizontally Oriented Emitter", Adv. Func. Mater. 23, 3896-3900 (2013).

[50] J. Frischeisen, D. Yokoyama, C. Adachi, and W. Brütting, "Determination of molecular dipole orientation in doped fluorescent organic thin films by photoluminescence measurements", Appl. Phys. Lett. 96, 073302 (2010).

[51] M. Flämmich, M. C. Gather, N.Danz, D. Michaelis, A. H. Bräuer, K. Meerholz, A. Tünnermann, "Orientation of emissive dipoles in OLEDs: Quantitative in situ analysis", Organic Electronics 11, 1039–1046, (2010).

[52] A. Graf, P. Liehm, C. Murawski, S. Hofmann, K. Leo, and M. C. Gather, "Correlating the transition dipole moment orientation of phosphorescent emitter molecules in OLEDs with basic material properties", J. Mater. Chem. C 2, 10298-10304 (2014).

[53] K.-H. Kim, S. Lee, C.-K. Moon, S.-Y. Kim, Y.-S. Park, J.-H. Lee, J. W. Lee, J. Huh, Y. You, and J.-J. Kim, "Phosphorescent dye-based supramolecules for high-efficiency organic light-emitting diodes", Nature Commun. 5, 4769 (2014).

[54] M. J. Jurow, C. Mayr, T. D. Schmidt, T. Lampe, P. I. Djurovich, W. Brütting, M. E. Thompson, "Understanding and predicting the orientation of heteroleptic phosphors in organic light-emitting materials", Nature Mat. 15, 85-91 (2016).

[55] C. Mayr, S. Y. Lee, T. D. Schmidt, T. Yasuda, C. Adachi, and W. Brütting, "Efficiency Enhancement of Organic Light-Emitting Diodes Incorporating a Highly Oriented Thermally Activated Delayed Fluorescence Emitter", Adv. Func. Mater. 24, 5232-5239 (2014).

[56] P. Liehm, C. Murawski, M. Furno, B. Lüssem, K. Leo, "Comparing the emissive dipole orientation of two similar phosphorescent green emitter molecules in highly efficient organic light-emitting diodes2, Appl. Phys. Lett. 101, 253304 (2012).

[57] J. Frischeisen, D. Yokoyama, C. Adachi, and W. Brütting, "Determination of molecular dipole orientation in doped fluorescent organic thin films by photoluminescence measurements", Appl. Phys. Lett. 96, 073302 (2010).

[58] T. D. Schmidt, D. S. Setz, M. Flämmich, J. Frischeisen, D. Michaelis, B. C. Krummacher, N. Danz, and W. Brütting, "Evidence for non-isotropic emitter orientation in a red phosphorescent organic light emitting diode and its implications for determining the emitter's radiative quantum efficiency", Appl. Phys. Lett. 99, 163302 (2011).

[59] L. Penninck, F. Steinbacher, R. Krause, and K. Neyts, "Determining emissive dipole orientation in organic light emitting devices by decay time measurements", Org. Electron. 13, 3079-3084 (2012).

[60] N. Irishina, M. Moscoso, R. Carminati, "Recovering fluorophore location and orientation from lifetimes2, Opt. Express 21, 421-430 (2013).

[61] T. D. Schmidt, L. J. Reichardt, A. F. Rausch, S. Wehrmeister, B. J. Scholz, C. Mayr, T. Wehlus, R. Mac Ciarnáin, N. Danz, T. C. G. Reusch, and W. Brütting, "Extracting the emitter orientation in organic light-emitting diodes from external quantum efficiency measurements", Appl. Phys. Lett. 105, 043302 (2014).

[62] E. M. Purcell, "Spontaneous emission probabilities at radio frequencies", Phys. Rev, 69, 681 (1946).

[63] M. Flämmich, "Optical characterization of OLED emitter properties by radiation pattern analyses, PhD thesis, Friedrich-Schiller-Universität, Jena, (2011).

[64] Yi-Lu Chang, “Efficient Organic Light-Emitting Diodes (OLEDs)”, Pan Stanford Publishing, (2015).

[65] Y. Q. Zhang, G. Y. Zhong, X. A. Cao, “Concentration quenching of electroluminescence in neat Ir(ppy)3 organic light-emitting diodes”, J. appl. Phys. 108, 083107, (2010).

[66] “High Efficiency Organic Light Emitting Diodes” (2016). Retrieved from https://www.iapp.de/organische-elektronik.de/en/?OLEDs___High_Efficiency_OLEDs

[67] C. Adachi , M. A. Baldo , M. E. Thompson ,S. R. Forrest, “Nearly 100% internal phosphorescence efficiency in an organic light emitting device”, J. Appl. Phys., 90 ,5048, (2001).

[68] H. Yersin , “Transition Metal and Rare Earth Compounds Excited States, Transitions, Interactions III”, ISBN: 978-3-540-20948-5, Top. Curr. Chem. , 241 , 1, (2004)

[69] T. Nelson, S. Fernandez-Alberti, A. E. Roitberg, and S. Tretiak, “Nonadiabatic excited-state molecular dynamics: Treatment of electronic decoherence”, The Journal of Chemical Physics 138(22), 224111 (2013).

[70] I. Hwang and G. D. Scholes, “Electronic Energy Transfer and Quantum-Coherence in -Conjugated Polymers”, Chemistry of Materials 23(3), 610{620 (2011).

[71] A. Köhler and H. Bässler, „Triplet states in organic semiconductors”, Mat. Sci. Eng. R., 66(4–6):71–109, (2009).

[72] G. D. Scholes “Long-Range Resonance Energy Transfer in Molecular Systems”, Annu. Rev. Phys. Chem., 54(1):57–87, (2003).

[73] Pope, M.; Swenberg, C. E., “Electronic Processes in Organic Crystals”, Oxford University Press, (1982).

[74] Turro, N. J., “Modern Molecular Photochemistry”, University Science Books, (1991).

[75] T. Förster. „Zwischenmolekulare Energiewanderung und Fluoreszenz“, Ann. Phys., 437(1-2):55–75, (1948)

[76] D. L. Dexter, "A Theory of Sensitized Luminescence in Solids", J. Chem. Phys., 21, 5, (1953).

[77] C. Murawski, K. Leo, and M. C. Gather, "Efficiency Roll-Off in Organic Light-Emitting Diodes" Adv. Mater., 25(47):6801–6827, (2013).

[78] D. Y. Kondakov, T. D. Pawlik, T. K. Hatwar, and J. P. Spindler, „Triplet annihilation

exceeding spin statistical limit in highly efficient fluorescent organic light-emitting diodes", J. Appl. Phys., 106, 12, 124510, (2009).

[79] [4410] Yichun Luo, Hany Aziz, Zoran D. Popovic, and Gu Xu, "Electric-field-induced fluorescence quenching in dye-doped tris(8-hydroxyquinoline)aluminum layers", Applied Physics Letters 89, 103505 (2006).

[80] J. Huang, Z. Xu, F. Zhang, S. Zhao, Y. Li, L.Song, X. Xu, "Dissociation of excitons in organic light-emitting diodes", Microelectronics Journal 38 501–504 (2007).

[81] S. Reineke, T. C. Rosenow, B. Lüssem, K. Leo, "Improved High-Brightness Efficiency of Phosphorescent Organic LEDs Comprising Emitter Molecules with Small Permanent Dipole Moments", Advanced Materials, 22, 3189 (2010).

[82] "Alkenes and alkynes" (05.12.2011). Retrieved from https://www.nyu.edu/classes/tuckerman/adv.chem/lectures/lecture_17/node5.html

[83] K.-C. Tang, Kuan Lin Liu, I-Chia Chen, "Rapid intersystem crossing in highly phosphorescent iridium complexes" Chemical Physics Letters 386, 437–441, (2004).

[84] H. Yersin and D. Donges "Low-Lying Electronic States and Photophysical Properties of Organometallic Pd(II) and Pt(II) Compounds. Modern Research Trends Presented in Detailed Case Studies", In H. Yersin, editor, Transition Metal and Rare Earth Compounds, number 214 in Topics in Current Chemistry, pages 81–186. Springer Berlin Heidelberg, (2001). ISBN 978-3-540-67976-9, 978-3-540-44474-9.

[85] H. Yersin, "Mechanisms of Exciton Trapping and Control of Emission Properties In Transition Metal and Rare Earth Compounds", volume 241, pages 1–

26. Springer, Berlin, Heidelberg, (2004). ISBN 978-3-540-20948-5, 978-3-540-39904-9.

[86] V. Bulovic, M. A. Baldo, and S. R. Forrest (Chapter 11) , Organic Electronic Materials, Conjugated Polymers and Low Molecular Weight Organic Solids, R. Farchioni and G. Grosso (Eds.), Springer-Verlag, Berlin Heidelberg (2001).

[87] Hartmut Yersin and Walter J. Finkenzeller, Triplet Emitters for Organic Light-Emitting Diodes, Wiley (2008)

[88] R. R. Chance, A. Prock, and R. Silbey, "Molecular Fluorescence and Energy Transfer Near Interfaces", Adv. Chem. Phys. 37, 1-67 (1978).

[89] C.-T. Tai, "Dyadic Green's Functions in Electromagnetic Theory", Intext, New York, (1971).

[90] N. Danz, R. Waldhäusl, A. Bräuer, and R. Kowarschik, "Dipole lifetime in stratified media", J.Opt. Soc. Am. B 19 (3), 412-419 (2002).

[91] N. Danz, J. Heber, A. Bräuer, and R. Kowarschik, "Fluorescence lifetimes of molecular dye ensembles near interfaces", Phys. Rev. A. 66 (6), 063809 (2002).

[92] K. H. Drexhage, "Interaction of Light with Monomolecular Dye Layers", Prog. Optics 12, 163-232 (1974).

[93] W. Lukosz and R. E. Kunz, "Light emission by magnetic and electric dipoles close to a plane interface. I. Total radiated power", J. Opt. Soc. Am. A 67 (12), 1607-1615 (1977).

[94] H. Kuhn, "Classical Aspects of Energy Transfer in Molecular Systems", J. Chem. Phys. 53 (1),101-108 (1970).

[95] K. A. Neyts, "Simulation of light emission from thin-film microcavities", J. Opt. Soc. Am. A, 15 (4), 962-971 (1998).

[96] A. P. Bartko, K. Xu, and R. M. Dickson, "Three-Dimensional Single Molecule Rotational Diffusion in Glassy State Polymer Films", Phys. Rev. Lett. 89, 026101 (2002).

[97] L. A. Deschenes and D. A. V. Bout, "Single-Molecule Studies of Heterogeneous Dynamics in Polymer Melts Near the Glass Transition", Science 292, 255-258 (2001).

[98] M. Lee, J. Kim, J. Tang, and R. M. Hochstrasser, “Fluorescence quenching and lifetime distributions of single molecules on glass surfaces”, Chem. Phys. Lett. 359, 412-419 (2002).

[92] K. H. Drexhage, “Interaction of light with monomolecular dye layers2, Prog. Optics 12, 165-232 (1974).

[99] F. Steiner, S. Bange, J. Vogelsang, and J. M. Lupton, “Spontaneous Fluctuations of Transition Dipole Moment Orientation in OLED Triplet Emitters”, J. Phys. Chem. Lett. 6, 999-1004 (2015).

[100] S. Reineke, F. Lindner, G. Schwartz, N. Seidler, K. Walzer, B. Lüssem, and K. Leo, “White organic light-emitting diodes with fluorescent tube efficiency”, Nature 459, 234-238 (2009).

[101] Y. Sun, N. C. Giebink, H. Kanno, B. Ma, M. E. Thompson, and S. R. Forrest, “Management of singlet and triplet excitons for efficient white organic light-emitting devices”, Nature 440, 908-912 (2006).

[102] S. W. Liu, J. H. Lee, C. C. Lee, C. T. Chen, J. K. Wang, “Charge carrier mobility of mixed-layer organic light-emitting diodes”, Appl. Phys.Lett. 91, 142106 (2007).

[103] (2016). Retrieved from http://www.adsdyes.com/images/electrophosphorescent/structure-ads076re.png

[104] (2016). Retrieved from http://cselsolar.com/index/pro/images/htl_image012.gif

[105] (2016). Retrieved from https://cdn.shopify.com/s/files/1/0823/0287/products/irppy3_1024x1024.png?v=1450364910

[106] C. Adachi, R. Kwong, S. R. Forrest, “Efficient electrophosphorescence using a doped ambipolar conductive molecular organic thin film”, Org. Elec. 2 37-43 (2001).

[107] “Radiating Slabs”, contact norbert.danz@iof.fraunhofer.de for further information.

[108] M. Flämmich, N. Danz, D. Michaelis, A. Bräuer, M. C. Gather, J. H.-W. M. Kremer, K. Meerholz, “Dispersion-model-free determination of optical constants:

application to materials for organic thin film devices", Appl. Optics 48 (8), 1507-1513 (2009).

[109] E. D. Palik, ed., Handbook of Optical Constants of Solids, Academic Press, New York, (1985).

[110] C. Hosokawa, H. Tokailin, H. Higashi, and T. Kusumoto, Transient behavior of organic thin film electroluminescence, Appl. Phys. Lett. 60, 1220-1222, (1992).

[111]Fig.6.1 and Fig.6.2, M. Flämmich, "Optical characterization of OLED emitter properties by radiation pattern analyses", PhD thesis, Friedrich-Schiller-Universität, Jena, (2011).

[112]Fig.6.3 and Fig.6.4, M. Flämmich, "Optical characterization of OLED emitter properties by radiation pattern analyses", PhD thesis, Friedrich-Schiller-Universität, Jena, (2011).

[113] A. Epstein, M. Roberts, N. Tessler, P. D. Einziger, "Analytical estimation of emission zone mean position and width in organic light emitting diodes from emission pattern image-source interference fringes", Journal of Applied Physics 115, 223101 (2014).

[114] Measurement performed at Fraunhofer IOF, Jena, Germany by M. Heusinger.

[115] M. Fujihira, L. Do, A. Koike, "Growth of dark spots by interdiffusion across organic layers in organic electroluminescent devices", Appl. Phys. Lett. 68, 1787, (1996)

[116] Y. Kawamura, K.Goushi, J. Brooks and J. J. Brown, H.Sasabe, C. Adachi, "100% phosphorescence quantum efficiency of Ir„III complexes in organic semiconductor films", Applied Physics Letters 86, 071104 (2005).

[117] S. Lamansky, P. Djurovich, D. Murphy, F. Abdel-Razzaq, H. Lee, C.Adachi, P.E. Burrows, S. R. Forrest, and M. E. Thompson, "Highly Phosphorescent Bis-Cyclometalated Iridium Complexes:Synthesis, Photophysical Characterization, and Use in Organic Light Emitting Diodes", J. Am. Chem. Soc., 123, 4304-4312, (2001).

[118] V.J. Logeeswaran, N. P. Kobayashi, M. S. Islam, W. Wu, P. Chaturvedi, N.X. Fang, S. Wang and R. S.Williams, "Ultrasmooth Silver Thin Films Deposited with a Germanium Nucleation Layer", Nano Letters, Vol. 9, No. 1, 178-182, (2009).

[119] W. Chen, M. D. Thoreson, S. Ishii, A. V. Kildishev, V.M. Shalaev, “Ultra-thin ultra-smooth and low-loss silver films on a germanium wetting layer”, Optics Express, Vol. 18, No. 5, 5124, (2010).

[120] A.I. Maaroof, G.B. Smith, “Effective optical constants of nanostructured thin silver films and impact of an insulator coating”, Thin Solid Films 485, 198 – 206, (2005).

[121] P.Zhao, W. Su, R. Wang, X. Xu, F. Zhang, “Properties of thin silver films with different thickness” Physica E41, 387–390, (2009).

[122] J. Gong, R. Dai, Z. Wang, Z. Zhang, “Thickness Dispersion of Surface Plasmon of Ag Nano-thin Films: Determination by Ellipsometry Iterated with Transmittance Method”, Scientific reports, 5 : 9279, (2015).

[123] M. Flämmich and N. Danz, Optical characterisation of OLED emitters from radiation pattern analyses, Woodhead Publishing Series in Electronic and Optical Materials, 36, 319-359 (2013).

[124] T. D. Schmidt, D. S. Setz, M. Flämmich, B. J. Scholz, A. Jaeger, C. Diez, D. Michaelis, N. Danz, W. Brütting, “Degradation induced decrease of the radiative quantum efficiency in organic light-emitting diodes”, Appl. Phys. Lett. 101, 103301 (2012).

[125] S. Wehrmeister, T. D. Schmidt,W. Brütting, Institute of Physics, University of Augsburg, Universitätsstr. 1, 86135 Augsburg, Germany

[126] Mauro Furno, Rico Meerheim, Simone Hofmann, Björn Lüssem, Karl Leo, „Efficiency and rate of spontaneous emission in organic electroluminescent devices”, Physical Review B 85, 115205 (2012).

[127] N. C. Giebink and S. R. Forrest, “Quantum efficiency roll-off at high brightness in fluorescent and phosphorescent organic light emitting diodes”, Phys. Rev. B 77, 235215 (2008).

[128] Yichun Luo, Hany Aziz, Zoran D. Popovic, and Gu Xu, “Electric-field-induced fluorescence quenching in dye-doped tris(8-hydroxyquinoline)aluminum layers”, Applied Physics Letters 89, 103505, (2006).

[129] J. Zhao Huang, Z. Xu, F. Zhang, S. Zhao, Y. Li, L. Song, X. R. Xu, "Dissociation of excitons in organic light-emitting diodes", Microelectronics Journal 38 501–504 (2007).

[130] M. D. Pace, W. R. Barger, A. W. Snow, "EPR of Copper Tetrakis(cumlphenoxy)phthalocyanine Langmuir-Blodgett Films", Journal Of Magnetic Resonance 75,73-82 (1987).

[131] D. Yokoyama, A. Sakaguchi, M. Suzuki, C. Adachi, "Horizontal molecular orientation in vacuum-deposited organic amorphous films of hole and electron transport materials", Applied Physics Letters 93, 173302 (2008).

[132] Y. Shirota, "Organic materials for electronic and optoelectronic devices", J. Mater. Chem., 10, 1-25, (2000).

[133]Y. Shirota, "Photo- and electroactive amorphous molecular materials—molecular design, syntheses, reactions, properties, and applications", J. Mater. Chem., 15, 75–93, 75, (2005).

[134] Qing Zhou, "Probing Three-Dimensional Single-Molecule Rotational Diffusion in Polymer", Journal of the Korean Physical Society, Vol. 47, August pp. S190S193 (2005).

[135] Y. Kawamura, J. Brooks, J. J. Brown, H. Sasabe, and C. Adachi, "Intermolecular interaction and a concentration-quenching mechanism of phosphorescent Ir(III) complexes in a solid film", Phys. Rev. Lett. 96, 017404, (2006).

[136] Caroline Weichsel, Lorenzo Burtone, Sebastian Reineke, Susanne I. Hintschich, Malte C. Gather, Karl Leo, and Björn Lüssem, "Storage of charge carriers on emitter molecules in organic light-emitting diodes", Physical Review B 86, 075204 (2012).

[137] M. D. Pace, W. R. Barger, and A. W. Snow, "Molecular Packing and Iodine Doping of Oxovanadium- and Copper-Substituted Tetrakis(cumy1phenoxy)phthalocyanine Langmuir-Blodgett Films Studied by ESR", Langmuir, 5, 973-978 973 (1989).

[138] R. Azumi, M. Matsumoto, Y. Kawabata, S. Kuroda, M. Sugi, L. G. King, M. J. Crossley, "Orientation Change of Porphyrin in Langmuir-Blodgett Films Caused by a Trigger Molecule", J. Phys. Chem.,97, 12862-12869, (1993).

[139] K. Ichimura, T. Kobayashi, K. A. King, and R. J. Watts, “Excited-State Absorption Spectroscopy of Ortho-Metalated Ir(III) Complexes”, The Journal of Physical Chemistry, Vol. 91, No. 24, 6105, (1987).

[140] Y. Koide, S. Takahashi, M. Vacha, “Simultaneous Two-Photon Excited Fluorescence and One-Photon Excited Phosphorescence from Single Molecules”, J. Am. Chem. SOC., 128, 10990-10991, (2006).

[141] G. J. Hedley, A. Ruseckas, I. D. W. Samuel, “Ultrafast Intersystem Crossing in a Red Phosphorescent Iridium Complex”, Journal of Physical Chemistry A, , 113, 2–4, (2009).

[142]M.G. Colombo and H. U. Giidel, “Synthesis and High-Resolution Optical Spectroscopy of his(2 42 4hienyl)pyridinato-e(2,2-bipyridine) iridium(III)”, Inorg. Chem.,32, 3081-3087, (1993).

[143]P. H.P. Harbach, A. Dreuw, “A fresh look at excitonically coupled chromophores from a Jahn–Teller perspective”, Chemical Physics 377, 78–85, (2010).

[144]T. Karatsu , E. Itoa, S.Yagai, A. Kitamura, “Radiative and nonradiative processes of meridional and facial isomers of heteroleptic iridium-trischelete complexes”, Chemical Physics Letters 424, 353–357,(2006).

[145] J. Lua, Q. Liu, J. Ding, Y. Tao, “New triscyclometalated iridium complexes for applications in phosphorescent light-emitting diodes”, Synthetic Metals 158 95–103, (2008).

[146] M. Lieberherr, Ch. Fattinger and W. Lukosz, “Optical environment-dependent effects on the fluorescence of submonomolecular dye layers on interfaces”, Surface Science 189/190 954-959 North-Holland, Amsterdam, (1987).

[147] M. P. Lettinga, E. M. Klarenbeek, Han Zuilhof, and M. A. M. J. van Zandvoort, “The Orientation of the Phosphorescence Dipole Moment of Erythrosine B Within Its Molecular Frame”, Journal of Fluorescence, Vol. 9, No. 3, (1999).

[148] M. P. Lettinga, H. Zuilhof, M. A. M. J. van Zandvoort, “Phosphorescence and fluorescence characterization of fluorescein derivatives immobilized in various polymer matrices”, Phys. Chem. Chem. Phys., , 2, 3697 -3707, (2000).

[149] K. Vasilev, W. Knoll, and M. Kreiter, “Fluorescence intensities of chromophores in front of a thin metal film”, The Journal of Chemical Physics 120, 3439, (2004).

[150] A. T. Yeh, C. V. Shank, J. K. McCusker, “Ultrafast Electron Localization Dynamics Following Photo-Induced Charge Transfer”, Science Vol. 289, 11, (2000).

[151] J. Kalinowski, ed., “Organic Light-Emitting Diodes: Principles, Characteristics, and Processes, Marcel Dekker, New York, (2005)

[152] M. A. Baldo and S. R. Forrest, “Transient analysis of organic electrophosphorescence : I. Transient analysis of triplet energy transfer”, Physical Review B Vol. 62, No. 16 II, (2000).

[153] D. S. Setz, T. D. Schmidt, M. Flämmich, S. Nowy, J. Frischeisen, B. C. Krummacher, T. Dobbertin, K. Heuser, D. Michaelis, N. Danz, W. Brütting, A.Winnacker, “Comprehensive efficiency analysis of organic light-emitting devices”, Journal of Photonics for Energy 011006-1 Vol. 1, (2011).

[154] T. Lampe, T. D. Schmidt, M. J. Jurow, P. I. Djurovich, M. E. Thompson,W. Brütting, “Dependence of Phosphorescent Emitter Orientation on Deposition Technique in Doped Organic Films”, Chem. Mater. 2016, 28, 712−715, (2016).

LIST OF FIGURES

Fig.2.1 Charge carrier energy levels in an OLED under forward voltage bias

Fig.2.2.1. Ethene molecular orbitals and energy levels.

Fig.2.2.2 Excitation and emission in an organo-metallic diatomic molecule.

Fig.2.3.1 Radiation characteristics of the orthogonal dipole components.

Fig. 2.3.2 Dipole emission from an OLED.

Fig.3.1.2.1 Single emitter device structure and energy levels.

Fig.3.1.2.2 Chemical structure sketches of materials.

Fig.3.1.3 Dual emitter device structure and energy levels

Fig. 3.2.2 General OLED emission measurement setup.

Fig.3.4.1 Intensity spectra with z misalignment.

Fig.3.4.2 Noise level at different wavelengths.

Fig. 4.1.1.1 Angular spectrum fitting assuming different confined EZPs.

Fig. 4.1.2.1 Angular spectrum fitting assuming multiple layer emission.

Fig.4.1.2.2 Förster transfer from emitters to the ETL.

Fig. 4.1.2.3 Confined and extended EZP angular spectra comparison.

Fig. 4.2.1 Intrinsic spectra measurements.

Fig. 4.3.1 Orientation ratio fitting with an extended EZP.

Fig. 4.3.2 TM angular spectra fitting comparison.

Fig. 4.4.1.1 Complete inter- layer device reflectivity fitting.

Fig. 4.4.1.2 Refractive index modification.

Fig. 4.4.2.1 Variation of emitter emission lifetimes with HTL spacer layer thickness.

Fig. 4.4.2.2 Intrinsic quantum efficiency from emission lifetime measurements

Fig. 4.5.1.1 Device emission characteristics.

Fig. 4.5.1.2 Polarization filtered emission lifetime measurements.

Fig. 4.5.2.1 In-plane polarized PL of non- inter- layer devices.

Fig. 4.5.2.2 Out-of-plane polarized PL of non- inter-layer devices.

Fig. 4.5.3.1 Out of plane polarized PL of inter-layer devices.

Fig. 4.5.4.1 inter- layer device EL angular spectra comparison.

Fig.5.1.1. Dual emitter intrinsic spectrum fitting.

Fig.5.1.2. Choosing the most AOP sensitive devices

Fig.5.2.1. Green EZP extraction for the 124 nm ETL device.

Fig.5.2.3. 124 nm ETL device angular spectra comparison.

Fig.5.2.4. Green EZP extraction for the 285 nm ETL device.

Fig.5.2.5. 285 nm ETL device angular spectra comparison.

Fig.5.2.2. Green emitter lifetime change with position.

Fig.5.3.1. Orientation ratio fitting for the 124 nm ETL device.

Fig.5.3.2. Orientation ratio fitting for the 285 nm ETL device.

Fig.5.4.1 Interference minimum of the 165 nm ETL device.

Fig.5.4.2. Interference minimum from 165 nm device at different current densities.

Fig.5.4.3. Red EZP extraction for the 165 nm ETL device at 50 $mAcm^{-2}$

Fig.5.4.5 165 nm ETL device complete angular spectra comparison at 50 $mAcm^{-2}$.

Fig.5.4.6 Interference minimum of the 325 nm ETL device at 5 $mAcm^{-2}$.

Fig.5.4.7 Red EZP extraction for the 325 nm ETL device at 5 $mAcm^{-2}$

Fig.5.4.8. Complete 325 nm ETL device angular spectra comparison at 5 $mAcm^{-2}$.

Fig.5.4.4. Red emitter lifetime change with position

Fig.5.4.9.Comparison of extracted intrinsic red spectra to red EL spectrum.

Fig.5.5.1. Orientation ratio fitting for the 165 nm ETL device.

Fig.5.5.2 Orientation ratio fitting for the 325 nm ETL device.

LIST OF ABBREVIATIONS

AOP – Active optical property

EF – Eigenfunction

EBL – Electron blocking layer

EL – Electroluminescence

EML - Emission layer

EOD - Emitter orientation distribution

ESR – Electron spin resonance

ETL – Electron transport layer

EZP – Emission zone profile

HBL – Hole blocking layer

HTL – Hole transport layer

ITO – Indium tin oxide

LC – Ligand centred

MLCT – Metal to ligand charge transfer

OLED - Organic light-emitting diode

RMS - Root mean squared

PL - Photoluminescence

TDM – Transition dipole moments

TE – Transverse electric field

TM – Transverse magnetic field

TPQ – Triplet-polaron quenching

SNR - Signal to noise ratio

LIST OF PUBLICATIONS

Peer reviewed papers

First author:

R. Mac Ciarnain, D. Michaelis, T. Wehlus, A.F. Rausch, N. Danz, A. Bräuer, A. Tünnermann, “Emission from outside of the emission layer in state-of-the-art phosphorescent organic light-emitting diodes” Organic Electronics 44 (2017) 115 - 119.

A paper title “Plasmonic Purcell effect reveals phosphor orientation details in Organic LEDs“ based on the results of Section 4.5.1 is in the process of being reviewed by Nature Scientific Reports for publication.

Co-author:

T. D. Schmidt, L. J. Reichardt, A. F. Rausch, S. Wehrmeister, B. J. Scholz, C. Mayr, T. Wehlus, R. Mac Ciarnáin, N. Danz, T. C. G. Reusch, W. Brütting, “Extracting the emitter orientation in organic light-emitting diodes from external quantum efficiency measurements” ,Appl. Phys. Lett. 105, 043302 (2014)

B.Conference papers

Co-author:

N. Danz ; R. MacCiarnain ; D. Michaelis ; T. Wehlus ; A. F. Rausch ; C. A. Wächter ; T. C. G. Reusch “OLED emission zone measurement with high accuracy”, Proc. SPIE 8829, Organic Light Emitting Materials and Devices XVII, 882923 (2013).

B.Conference contributions

Talks:

R. MacCiarnain, “Fluctuating Emission Dipole Moments of Aligned Phosphors in Organic Light-Emitting Diodes” OSA Light, Energy and the Environment Congress, , Kongresshalle am Zoo, Leipzig, Germany, (14 - 17 November 2016)

Posters:

R. MacCiarnain, “Emitter orientation analysis in multi-color organic light-emitting diodes”, 10th International Conference on Electroluminescence and Organic Optoelectronics (ICEL ’10), Cologne, Germany (August 31 – September 3, 2014)

AKNOWLEDGEMENTS

First of all I would like to thank Dr. Norbert Danz for always making himself available throughout my dissertation work for help and advice. I was very lucky to have such a good scientist as a supervisor who was always willing to help me in the Lab and to spend considerable time discussing and explaining our work together. Whenever I was stuck on some problem or some experimental approach, talking with Norbert always helped. I would also like to sincerely thank Dr. Dirk Michaelis for giving a lot of his time to help me with theoretical aspects of my work. I am also indebted to Dr. Thomas Wehlus and Dr. Andreas Rausch of Osram OS Regensburg for a very cordial and generous working relationship. They have both been very helpful in manufacturing many novel devices and giving us much information without which this work would of course have not been possible. I would like to thank my dissertation supervisor Prof. Andreas Tünnermann for being always kind and jovial with me even in the stressful times, and I believe he is responsible for a very nice work atmosphere at Fraunhofer IOF, Jena. Of course most of my time was spent with my department A3. I have spent nearly 5 years with this group of 50 or so people headed by Dr. Andreas Bräuer. I cannot believe that such a friendly and cooperative working environment exists in another physics group, and again a lot of credit should be given to Dr. Andreas Bräuer for this. I first came to Jena to join the Masters program at the Abbe School of Photonics, so including this is seven years in Jena. I would like to thank Prof. Pertsch, Claudia Lang, Szilvia Mammel and Dörte Hansen for going way beyond the reach of their jobs and helping me and the other students to reach the sucesses we have today. Of course, I spent the most time with my fellow Masters students, Jan Willem, Markus, Nadja, Jose, Victor and not always studying….to these guys I have met friends for life. In particular I would like to thank my first roommate in Jena, Kemal Safak. It's a pity our Bro Berkcan didn't make it to join us in Jena. Kemal is the best guy I have ever met . He will hand in his dissertation tomorrow so I guess I will be meeting him for a beer very soon….which reminds me of the other wheel in our tricycle, Lisa-Marie Elke Hahn. I am so glad to have a German family like hers to call my own ☺. Also a shout out to the Hinter-meilingen-Gangsta crew of Ellie-Doggie and Lisa Groß. Football was also very important to me so I'd like to thank my football buddy Peter Mohr Mohr Mohr, see you soon man. Back to Fraunhofer, and I would never have survived if it wasn't for my international lunch group here, I hope I don't forget anyone but

Sean, Shu, Marc Riegey, Meabh, Mateuzs, Pauline Hibonero, Jacobo, Polvo & Schneidah, Liza akdemeeeva, Vera the Avenger, Sophie, Daddy Max, Flo-rian, Schneeman, Manu, it made me very happy to be able to get away from the work and meet you guys almost everyday. To my flatmates in Jena, the Magdelstieg Mafia, David, Jana and Lena, I know I didn't get much time to spend with yous the last while but I'm nearly free now! To my Bundoran/Moyola boys, really lucky to have a group of lads like yous, who have made the effort to always be there and keep in touch no matter the distance, of course Ryanair helped ;). Of course, last but not least, to my family, I don't know if everybody says this but I could not think of having a possibly better family for love and support, I will thank you guys personally.

EHRENWÖRTLICHE ERKLÄRUNG

Ich erkläre hiermit ehrenwörtlich, dass ich die vorliegende Arbeit selbständig, ohne unzulässige Hilfe Dritter und ohne Benutzung anderer als der angegebenen Hilfsmittel und Literatur angefertigt habe. Die aus anderen Quellen direkt oder indirekt übernommenen Daten und Konzepte sind unter Angabe der Quellen gekennzeichnet.

Bei der Auswahl und Auswertung folgenden Materials haben mir die nachstehend aufgeführten Personen in der jeweils beschriebenen Weise unentgeltlich geholfen:

1.

2.

3.

Weitere Personen waren an der inhaltlich-materiellen Erstellung der vorliegenden Arbeit nicht beteiligt. Insbesondere habe ich hierfür nicht die entgeltliche Hilfe von Vermittlungs bzw. Beratungsdiensten (Promotionsberater oder andere Personen) in Anspruch genommen. Niemand hat von mir unmittelbar oder mittelbar geldwerte Leistungen für Arbeiten erhalten, die im Zusammenhang mit dem Inhalt der vorgelegten Dissertation stehen.

Die Arbeit wurde bisher weder im In- noch im Ausland in gleicher oder ähnlicher Form einer anderen Prüfungsbehörde vorgelegt. Teile dieser Arbeit wurden jedoch aus Prioritätsgründen bereits veröffentlicht oder wurden zur Veröffentlichung eingereicht.

Die geltende Promotionsordnung der Physikalisch-Astronomischen Fakultät der Friedrich-Schiller-Universität Jena ist mir bekannt.

Ich versichere ehrenwörtlich, dass ich nach bestem Wissen die reine Wahrheit gesagt und nichts verschwiegen habe.

Jena, 3. November 2016 _____

Rossá Mac Ciarnáin

CURRICULUM VITAE

Name Rossá Mac Ciarnáin

Date of birth 16.06.1987

Birthplace Sligo, Ireland

Education

1991 - 1999 Primary school

1999 - 2005 Secondary school

05.2005 Leaving certificate (Abitur)

09.2005 – 05.2009 Bachelor of Science in Applied Physics and Electronics

National University of Ireland Galway, Ireland

2008 - 2009 Bachelor Thesis

Efficiency of Photovoltaic cells Supervisor: Dr. Miriam Byrne

School of Physics NUI Galway

05.2009 B.Sc received

10.2009 – 02.2012 Master of Science in Photonics

Abbe School of Photonics, Friedrich-Schiller University,

Jena, Germany

11.2011 – 02.2012 Master thesis "Transient Electroluminescence Decay

Analysis of Organic LED Devices" Supervisors: Dr. Hans-Peter Loebl

Prof. Thomas Pertsch

at Philips Research Aachen

03.2012 M.Sc. Photonics recieved

Professional activity

11.2011 – 02.2012 Master student at Philips Research Aachen

Since 05.2012 –Doctor student at Fraunhofer-Institut für Angewandte Optik und Feinmechanik IOF, Jena

Jena, 3. November 2016 _____

Rossá Mac Ciarnáin